Maastricht UMC+

Maastricht University

TU Delft

ACTUATOR DESIGN FOR A VISCOUS IMPELLER PUMP TO POWER THE FONTAN CIRCULATION

Marina Krijgsman
5030536
July 2021

Advisor MUMC+: Dr. A. Sizarov
Advisor UM: Dr.ir. G.J.M. Tuijthof
Advisor TU Delft: Prof. dr. P.J. French

Abstract

Patients with a Fontan circulation have a diminished life expectancy of only 30-40 years old. A mechanical circulatory assist device can potentially increase their life expectancy and quality of life. Given the complexity of the anatomy and physiology of the Fontan circulation, design of a safe and effective mechanical assist device is a challenging task. A device based on a viscous impeller pump is very attractive. Such a device is amenable for minimally invasive implantation through a catheter, given the miniaturization of its actuator is possible. The current thesis provides the first steps in designing and developing the small brushless electromagnetic motor intended to drive the viscous impeller pump. First, a list of requirements was defined for such an actuator. The essential requirements are that the actuator is 5.4 mm in diameter and 11 mm in length, has an outrunner configuration, can reach a power output of at least 0.92 Watts and that the within the motor generated temperature does not excessively heat up the surrounding blood or breaks the actuator. After that, the actuator's first concept was defined and validated on the torque output and heat generation. After that, various optimizations of the design were performed, which resulted in a potentially promising actuator concept. Although, the presented actuator concept meets the prescribed dimensions and is an outrunner BDLC motor, the predicted power and torque output of 0.632 Watts and 2446 μNm, respectively, both are above the required values. The actuator needs to be tested to conclude if the actuator can indeed provide sufficient drive resulting in required pumping power of the VIP.

Table of Contents

Acknowledgement

I want to begin this acknowledgment by expressing my gratitude to Dr. Aleksander Sizarov, Dr. Gabrielle Tuijthoff, Professor Paddy French, and Enrico Tofolli for supporting me the past year through my graduation project. Thank you for giving me the opportunity to work on such an innovative project.

Gabrielle Tuijthoff guided me through my project and taught me to be a more structured engineer. She pointed me in the right direction and kept track of the path to follow. Although I pushed her buttons with being chaotic from time to time, she patiently taught me how to regain structure in the project. Without Gabrielle, the meetings would have been a lot less structured, and she pointed how to make a clear argument. Also, she always noted when I was talking at cross-purpose with another advisor during the meetings.

I would like to express my appreciation to Aleksander Sizarov, who allowed me to work on his project. He helped me to understand the clinical implications and to point out the current problems. The enthusiasm with which Aleksander wants to improve the lives of his patients is inspiring. He would answer my emails late at night or even on weekends. He helped me to improve my thesis on correctness and phrasing.

I would like to thank Professor Paddy French for supporting me with his helpful technical input during the meetings. He showed me the possibilities of the TU Delft and its facilities. Professor Paddy French helped me with the electrical engineering challenges and how to solve them.

I would like to express my appreciation to Enrico Tofolli, who I could also ask for an early morning meeting. Enrico Toffoli helped me enormously as a sparring partner to look with me through formulas and ideas. With his knowledge of electronics, he could point me in the right direction and indicate subjects I neglected or forgot.

1. Introduction

Five out of 100,000 babies are born with a single ventricle heart defect Harris and George (2017) as depicted in Figure 1. Most of these patients do not survive their first year of life if no palliative interventions are performed. After a primary intervention, typically within the first weeks after birth, a series of surgical procedures are performed to modify the univentricular heart and/or great vessels. The intervention separates the systemic and pulmonary blood flows, which ensures a more sustainable supply of oxygen and nutrients to the tissues. As a result of these modifications, a total cavopulmonary connection (TCPC) is established, through which the blood coming from the venae cavae flows passively through the lungs while the heart is actively pumping blood only to the body circulation (Fontan & Baudet, 1971). This circulation is called a Fontan circulation, which contrasts with the normal situation where the systemic venous blood passes through the right side of the heart and is actively pumped into the lungs. About 60,000 patients worldwide have a Fontan circulation, with many of them suffering from complications that lower their quality of life, such as development deficits and diminished exercise tolerance (Broda, Downing, & John, 2020; Nayak & Booker, 2008). Although the modifications of surgical techniques currently ensure a 95% chance of survival at the age of 15 after the TCPC completion. The total life expectancy of such patients is low, with the majority dying at 30-40 years of age (Hsu, 2015; Lyle, Said, & Egbe, 2017).

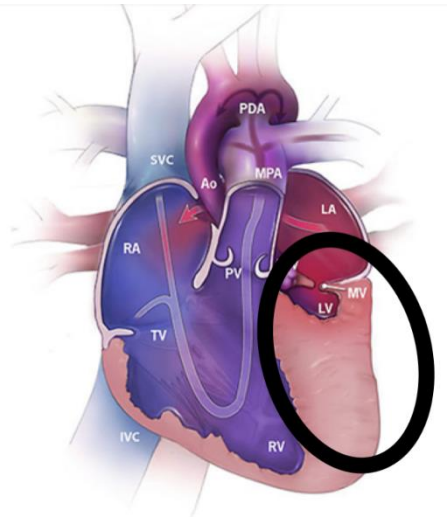

Figure 1: Anatomy of Hypoplastic Left Heart Syndrome, one of the types of single ventricle heart defects. The left ventricle is severely underdeveloped, indicated by the black circle. (image courtesy ("Facts about Hypoplastic Left Heart Syndrome," 2019)) Ao, Aorta; AoV, Aortic Valve; LA, Left Atrium; LV, Left Ventricle; IVC, Inferior Vena Cava; MPA, Main Pulmonary Artery; MV, Mitral Valve; PDA, Patient Ductuc Arteriosis; ; PV, Pulmonary Valve; RA, Right Atrium; RV, Right Ventricle; SVC, Superior Vena Cava; TV, Tricuspid Valve

Since the introduction of the Fontan procedure in 1971, research has focused on improving surgical procedures and treating complications. However, the only real treatment for the failing Fontan circulation is heart transplantation. Unfortunately, this is also associated with many difficulties and higher costs (Urencio, Greenleaf, Salazar, & Dodge-Khatami, 2016). The main problem in a failing Fontan circulation is the increased systemic venous and lymphatic pressures combined with a decreased pressure in pulmonary arteries (Leval, 1998). This combination is described as the Fontan paradox, causing numerous long-term complications, eventually resulting in the patient's death. Mechanical circulatory assistance by a device implanted within the TCPC intersection would augment the pulmonary blood flow while decreasing systemic venous pressures, and thus reversing the Fontan paradox (Rodefeld et al., 2011). This would prevent or postpone the need for heart transplantation and significantly increase life expectancy. Rodefeld et al. (2011) introduced a biconical viscous impeller pump (VIP) design to mechanically assist the blood flow within the TCPC circuit). However, the proposed design of the VIP requires a major surgical procedure for implantation of the heart (Rodefeld et al., 2019), which should ideally be avoided in clinically deteriorated and unstable patients with failing Fontan circulation.

The VIP by Rodefeld et al. (2011) showed the potential to provide the required support to a failing Fontan circulation. However, Rodefeld et al. (2019) chose not to pursue a catheter-based approach but instead of this, they applied a complete replacement of the TPCP with a VIP integrated within a rigid 4-way case, implantation of which requires a major open surgery. The idea of a catheter-based VIP for Fontan circulation was studied further because of the promising original results. No actuator inside the TCPC was presented in the original idea, and it remained unknown if it is possible to design an actuator that can power and fit within such a small viscous pump. Therefore, the first step is in the continuation of the development of the VIP is to design an actuator that is small but capable of delivering the required power. This thesis aims to design an actuator for the catheter-based VIP and demonstrates its feasibility by calculations and analysis.

1.1 Thesis layout

This thesis is divided into nine chapters. The second chapter presents a brief background of healthy cardiovascular physiology, followed by pathological cardiovascular physiology in patients with a univentricular heart defect. Next, the Fontan surgical procedure is explained along with the complications associated with a Fontan circulation. Then the mechanical assist device is introduced that can treat these complications. A brief overview of mechanical devices is provided to form a basis of the possibilities and their application for the Fontan circulations. The chapter concludes with the mechanical assist device forming the basis for the given research study. Chapter 4 explains the basics of electric motors, power losses in the electric motor, equations of the torque output, and an equation to calculate the actuator's internal temperature. Chapter four qualitatively defines the dimensional and output requirements for the actuator and concludes with a list of all the requirements. Chapter five presents the concept design for the actuator, followed by a design validation by calculating the torque output and internal temperature. Then chapter six presents the optimization of the concept design for various parameters. The manufacturing processes and materials are discussed, which are required to produce the components of the presented electric motor. The components first to fail are mentioned, and the chapter concludes with an improved final concept design of the actuator. In chapter seven, the test protocols are described to test the physical prototype after manufacturing. In chapter eight, the discussion is provided on the met requirements, the requirements which need to be improved, the limitations of the current study, and the future steps.

2. Clinical background

Chapter 2 presents a brief background on regular cardiovascular circulation, and then describes the single ventricle heart defect and the Fontan circulation. In the next section, the hemodynamic problems arising with the Fontan circulation and the gap in the treatment of cardiac assist devices are discussed that can be potentially resolved. After that, the current cardiac assist devices are discussed, including their application for the Fontan circulation. The chapter concludes with the current developments for cardiac assist devices specifically developed for the Fontan circulation and the need to develop the actuator powering the cardiac assist device.

2.1 Regular cardiovascular circulation

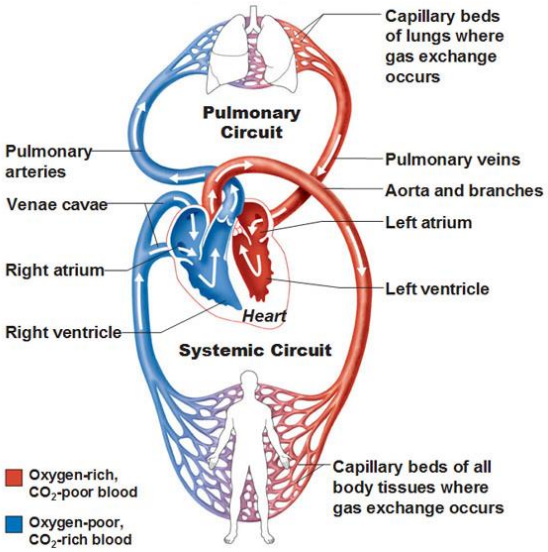

Figure 2: The heart as a double pump with the pulmonary and the systemic circuit. The blue colored vessels indicate the oxygen poor blood and the red colored vessels indicate the oxygen rich blood. The white arrows indicate the direction of the blood flow. Image courtesy ("Intro to the heart," 2012)

The primary function of the cardiovascular system is to supply the body with dissolved oxygen, nutrients and remove carbon dioxide including waste products (Calvert & Lefer, 2012). The anatomically normal heart consists of two separated synchronized pumps, one on the heart's right side and the other on the left side. Each pump consists of an atrium and a ventricle. These pumps drive the blood simultaneously and parallel through the two circuits: systemic circulation and pulmonary circulation (Figure 2). Figure 3 shows a healthy heart's anatomy in an adult. The left side is more muscular and thereby stronger than the right side because the left ventricle must provide blood to the high resistance systemic circulation. The pressure in the pulmonary circuit is 25% of the pressure in the systemic circuit. In the heart, four valves guard the heart ventricle's inlets and outlets to prevent blood's backflow (Figure 3 depicts the four valves).

An adult heart beats approximately 75 beats per minute, providing a blood flow of 5 L/min. The events from the beginning of a heartbeat to the next heartbeat are referred to as the cardiac cycle. A cardiac cycle consists of the diastole (relaxation) and the systole (contraction) of both atria and ventricles (Calvert & Lefer, 2012). In the diastole, the atriums and ventricles are relaxed. As a result, oxygen-poor blood from the venae cavae and oxygen-rich blood from the pulmonary veins flows into the right and left atrium, respectively. The pressure gradient causes the opening of the tricuspid and mitral valves, resulting in the inflow of blood into the ventricles. Nearly 75% of the blood flows passively due to the ventricles suction effect and the other 25% flows through the contraction of the atria. After filling the ventricles, the ventricular contraction follows, propelling the oxygen-rich blood from the left ventricle into the aorta towards the systemic circuit and the oxygen-poor blood from the right ventricle into the pulmonary arteries towards the lungs. This contraction causes the pressure to rise within the ventricles resulting in the closure of the inlet valves and opening of the outlet valves. After the blood passes through the lungs and the other organs, the blood flows back to the heart and the cardiac cycle repeats itself.

2.2 Univentricular type congenital heart defects

Congenital heart defects are the structural problems of a heart and the major vessels arising from abnormal formation before birth ("About Congenital Heart Defects," 2020). One of the most complex and severe congenital heart defects is single ventricle heart defects (SVHD). In SVHD, one of the ventricles is severely underdeveloped, which results in a single functioning pump inside the heart as depicted in Figure 1.

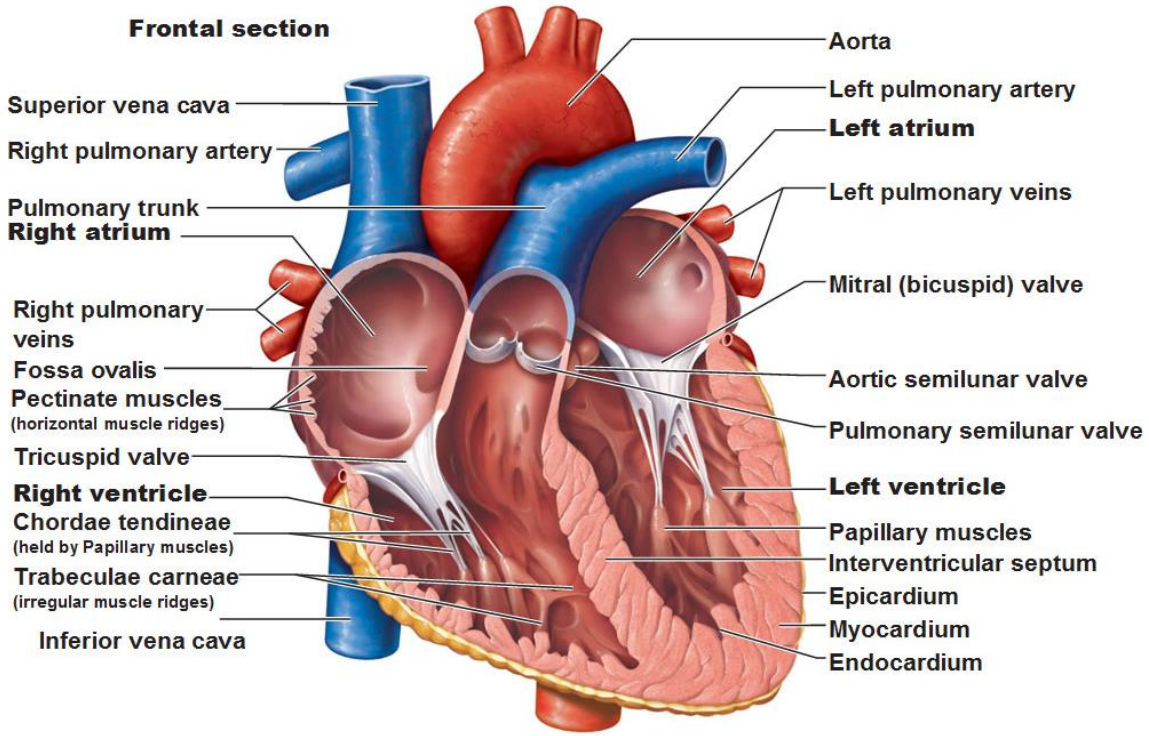

Figure 3: Frontal cross-section of a normal human heart. Image courtesy ("Intro to the heart," 2012). All the components of a healthy heart a depicted including the vessels and four valves.

Different types of SVHDs are known, with the most common being hypoplastic left heart syndrome (Figure 1), which is a combination of abnormalities of the heart's left side. The left ventricle, aorta, and valves connected to the left ventricle are undersized (Norwood, Kirklin, & Sanders, 1980). As a result, the heart's right side must pump simultaneously into both the pulmonary circulation and the high resistance systemic circulation. Another relatively mostly occurring form of SVHD is tricuspid valve atresia. Failure of the right-sided atrioventricular valve leads to a hypoplastic right ventricle, resulting in the left ventricle pumping the blood simultaneously into both circulations (Harris & George, 2017). Thus, both the right and left ventricle can be affected when a baby is born with an SVHD. In any case of the SVHD, a septal defect between the left and right atria and/or ventricles enables the blood mixing between the systemic and the pulmonary circulation, making simultaneous pumping into both the lungs and the body possible with only one ventricle. Due to this septal defect, the baby can survive until the first surgery is performed. However, to ensure survival, patients born with the SVHDs usually need complex surgery in the first year of their life. During a series of surgical procedures pulmonary and systemic circulations are separated, which will be further explained in the next section.

2.3 Fontan circulation palliation

In 1968, Dr. Francis Fontan proposed a surgical procedure to solve the hemodynamic problem of SVHD in patients with tricuspid valve atresia (Fontan & Baudet, 1971). In the late 1980s, the procedure was modified into two-stage surgical reconnection of both venae cavae directly to the pulmonary artery branch, thereby creating the TCPC. The circulation containing a TCPC is called a Fontan circulation. In the Fontan circulation, the flow towards the lungs is passive and is carried out by the systemic venous pressure. The patients' criteria to meet to be accepted as suitable candidates for the TCPC completion procedure have been refined over the years, thereby increasing patients' quality of life with Fontan circulation (Gewillig, 2005; Nayak & Booker, 2008).

The TCPC is currently completed in two stages. High pulmonary vascular resistance and the small size of pulmonary arteries make it impossible to perform the Fontan palliation directly after birth (Gewillig, 2005). Staged creation of the Fontan circulation allows the patient's body to gradually adapt to the hemodynamic changes. Often, an additional primary palliation is needed in SVHD patients aiming to relieve any existing

systemic obstruction, provide sufficient pulmonary blood flow to allow adequate oxygen delivery to tissues, and let the necessary pulmonary arterial growth (Nayak & Booker, 2008). An initial palliation is usually performed in the newborn period to ensure sufficient and balanced blood flow simultaneously into systemic and pulmonary circulations. During the initial palliation a balanced flow to the lungs and the body ensured, for example, using the Norwood procedure with a shunt placed between a branch of the aorta and the pulmonary artery in the hypoplastic left heart syndrome (Figure 4a).

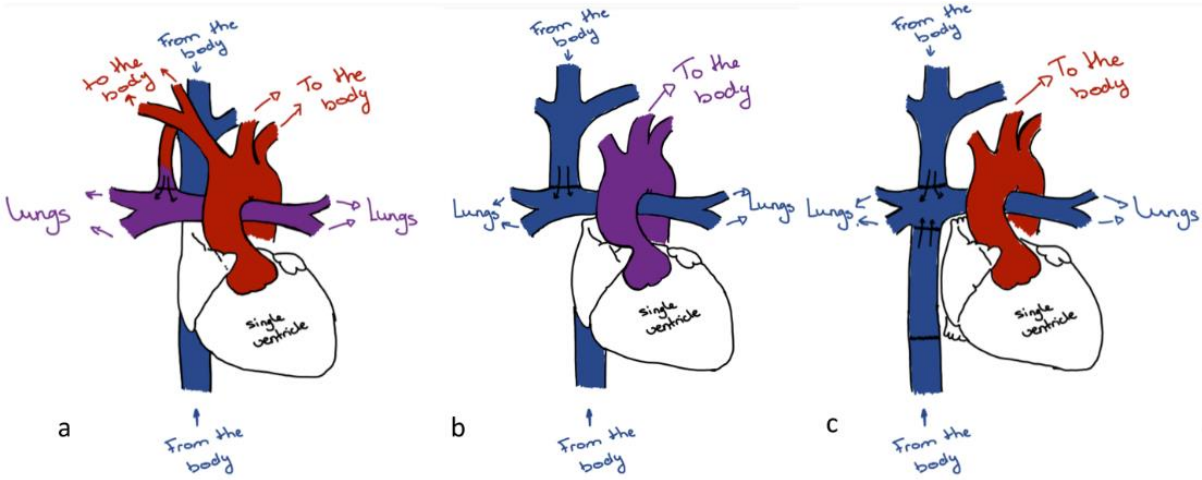

Figure 4: An example of a staged surgical repair of a single ventricle heart, ending with the VIP inside the TCPC. The red-colored vessels indicate the oxygen-rich blood, the blue-colored vessels the oxygen-poor blood, and the purple-colored vessels a mix between the oxygen-poor and the oxygen-rich blood. (a). Stage 1 (Norwood repair): A shunt is created between the aorta and the pulmonary artery, allowing blood flow to the lungs. b) Stage 2 (Hemi-Fontan repair): The superior vena cava is connected to the pulmonary artery, which is the only source of pulmonary blood flow. c) Stage 3 (Fontan completion): The inferior vena cava is also connected to the connection between the superior vena cava and the pulmonary arteries creating the TCPC.

After about two to six months, the first stage of Fontan circulation is performed based on either bidirectional Glenn anastomosis or Hemi-Fontan operation. The exact timing of this procedure depends on pulmonary arteries growth and the state of the pulmonary vascular resistance. During the establishment of the bidirectional Glenn anastomosis, the shunt is removed, and the superior vena cava is connected to the pulmonary artery branch as shown in Figure 4b. In about 1 to 5 years, the patient usually starts to experience restrictions due to the low pulmonary blood flow in only partial heart bypass and the completion process of the TCPC is performed. During the TCPC completion procedure, the inferior vena cava is connected to the pulmonary artery branch, using a synthetic graft conduit (Figure 4c). In the TCPC, all the oxygen-poor blood from systemic venous circulation flows passively into the pulmonary circulation. As a result, the systemic ventricle becomes the only power source for the Fontan circulation (Leval, 1998). Such a situation does lead to many complications for the patients and results in a much shorter life expectancy of an average of 35 – 40 years compared to 70 – 80 in the general population (Lyle et al., 2017).

2.3.1 Hemodynamic problems arising from long-term Fontan circulation.

Figure 5a shows the normal biventricular circulation where the mean pressure in the vena cava is below 10 mm Hg, and the pressure in the pulmonary arteries is above 15 mm Hg. However, in the Fontan circulation (Figure 5b), there is a significant pressure rise in the vena cava and relative hypotension in the pulmonary arteries. This difference in pressure causes the Fontan paradox, a simultaneous increase in systemic venous pressure and decreased pulmonary arterial pressure caused by the missing subpulmonary ventricle (Leval, 1998).

The Fontan paradox causes many complications, for example, diminished exercise tolerance, protein-losing enteropathy, development deficit, ventricular dysfunction, arrhythmias, and thromboembolism (Nayak & Booker, 2008). The most common cause of late mortality in Fontan patients is the so-called 'failing Fontan circulation' which is a broad term to describe Fontan circulation dysfunction (Broda et al., 2020). A failing Fontan is not the same as congestive heart failure due to left ventricular dysfunction. The underlying cause of a failing Fontan circulation is the persistent systemic venous and lymphatic hypertension accompanied by

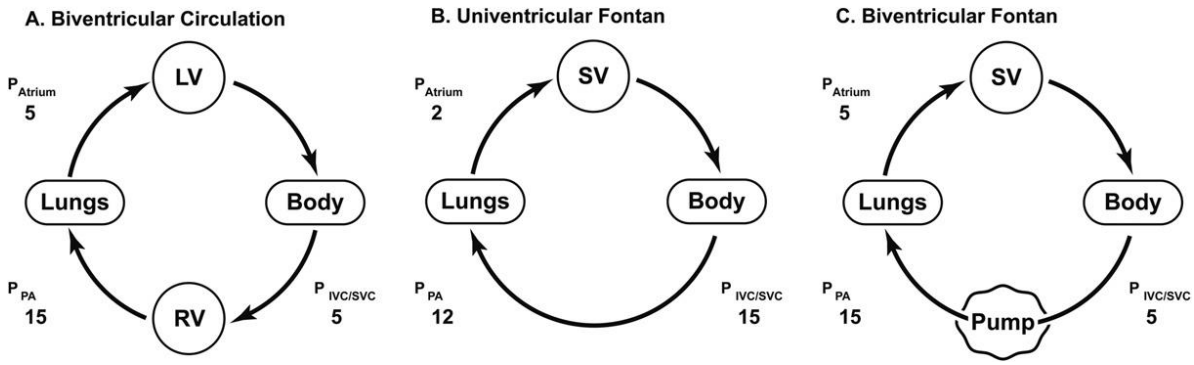

Figure 5: Overview of the pressure in the biventricular circulation, univentricular Fontan, and the biventricular Fontan with the implanted pump. The values indicate the blood pressure in mmHg (Image courtesy (Rodefeld, Frankel, & Giridharan, 2011). LV, Left Ventricle; RV, Right Ventricle; SV, Single Ventricle

low pulmonary blood flow and not primary myocardial dysfunction as in heart failure (Rodefeld et al., 2011). However, Fontan failure presents classic heart failure symptoms, increased tissue/organ water content, and decreased tissue/organ perfusion. Both symptoms eventually require a heart transplant. According to Leval (1998), it should be feasible to reverse the Fontan paradox by developing a cardiac mechanical device that lowers the vena cava pressure by 5 mm Hg and augments the pulmonary artery pressure by 5 mm Hg (Figure 5c).

2.4 Circulatory mechanical assist devices

Cardiac mechanical assist devices have been developed since 1960 for patients with congestive heart failure to replace the cardiopulmonary bypass circuit, thereby supporting the pumping function of the failing heart (Stewart & Givertz, 2012). Assist devices can be categorized based on the ventricle they support; left ventricular assist device, right ventricle assist devices, and biventricular assist devices (Figure 6) (Han & Trumble, 2019). The first generation of cardiac assist devices generated a pulsating flow. A diaphragm and unidirectional artificial heart valves caused the filling and emptying of the device, mimicking diastolic and systolic phases of the cardiac cycle (Mancini & Colombo, 2015). The second and third generations of the cardiac assist devices implement the axial or centrifugal pumps resulting in continuous blood flow (Figure 7). Over the years, the cardiac pumps are reduced in size; however, major surgery is still required to implant these devices into the patients. Another concern is that cardiac assist devices may cause vascular obstruction in case of a malfunction that can have lethal consequences.

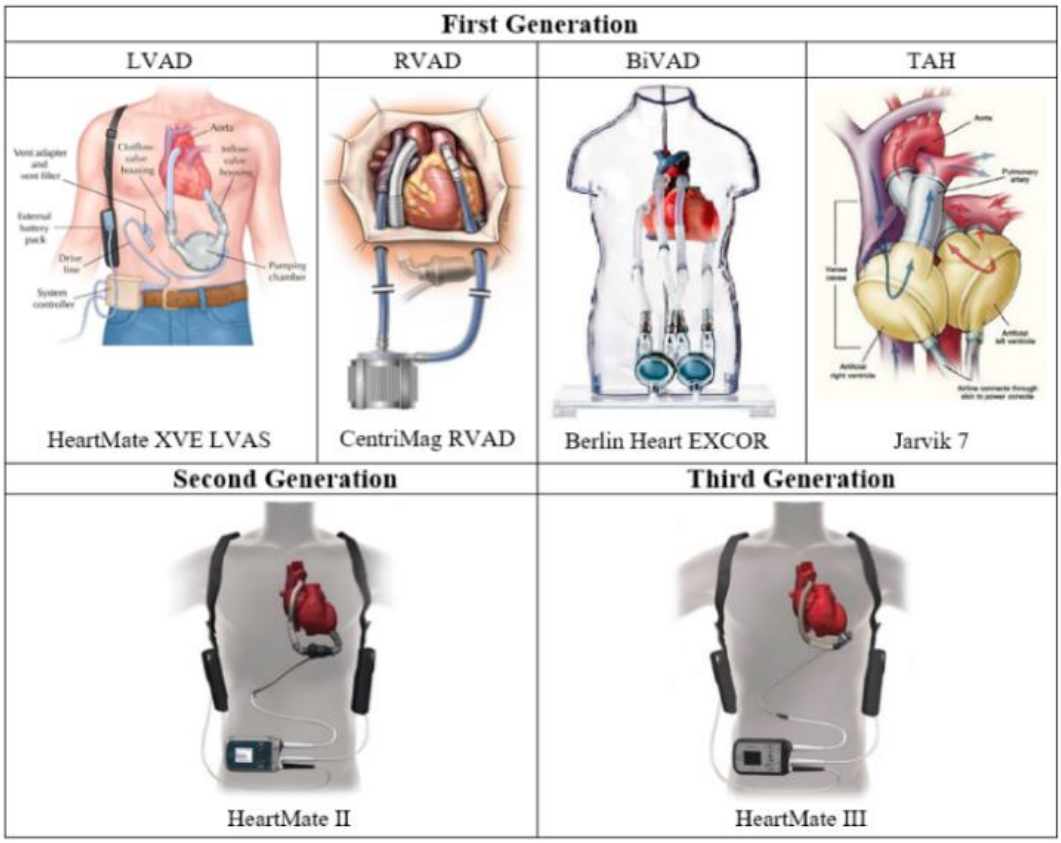

Figure 7: Examples of the three generations cardiac assist devices (image courtesy (Han & Trumble, 2019)).BiVAD, biventricular assist device; LVAD, left ventricular assist device; RVAD, right ventricular assist device; TAH, total artificial heart.

Besides these two main concerns, there are several other concerns when introducing a pump into the circulatory system. One of the major ones is hemolysis, which is the breakdown of the red blood cell membranes (Deutsch, Tarbell, Manning, Rosenberg, & Fontaine, 2006). Red blood cells are the oxygen carriers in the blood; a breakdown of their membrane causes a release of hemoglobin and other red blood cell components into the bloodstream resulting in anemia and reduced capacity of blood to carry oxygen. High shear-stress levels induced by a cardiac assist device in the bloodstream can cause hemolysis (Y. T. Delorme et al., 2013). On the other hand, low shear stress due to slow blood flow or low pressures is associated with thrombosis. In cardiac assist devices designed nowadays, the surface area contacting the blood is kept to a minimum, impeller profiles are adjusted, implantation invasiveness minimized, and less reactive surface material is used. Besides the above concerns, several other problems are mentioned in the literature, such as bacterial infections, commonly from percutaneous drivelines (Han & Trumble, 2019).

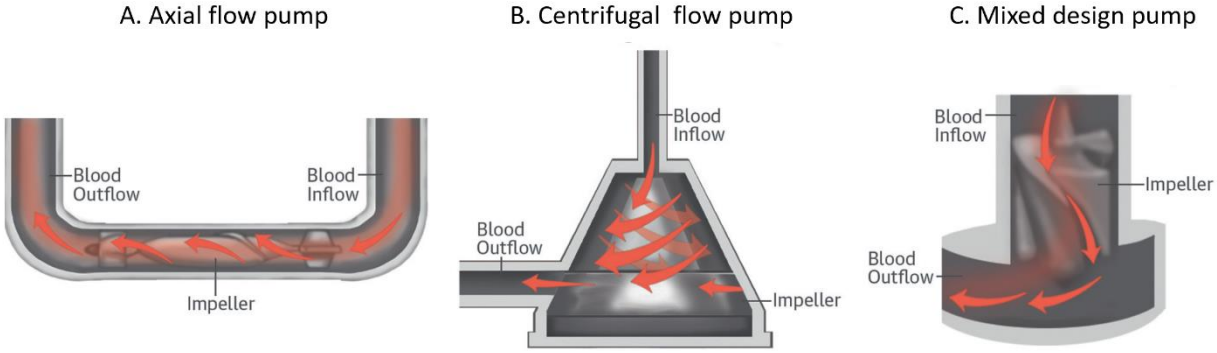

Figure 6: Three different pumping systems left ventricular assist device (image courtesy (Mancini & Colombo, 2015))

However, this risk factor is unavoidable because the cardiac assist devices need power, communication, and control, provided by a unit located outside the body. When connecting the power and control unit with the implanted device, the driveline enters the body through the skin, creating a potential entry site for bacteria. Minimizing the power-control unit, decreasing the device's power consumption, and increasing the battery capacity would avoid the need for a driveline outside the body.

Recently, two cardiac assist devices are developed that are implantable through catheter-based procedures (Kapur et al., 2020; Smith et al., 2019). Catheter-based procedures reduce the surgical complexity and significantly reduce the risk. The Intra-arterial blood pump by Smith et al. (2019) is a miniature left ventricular assist device (Figure 8). The Intra-atrial blood pump is percutaneously delivered and positioned across the atrial septum to support the compromised left atrium. The Intra-arterial blood pump draws blood from the left atrium and transfers it to the pulmonary arteries. Thus, the inflow of the blood is perpendicular to the outflow of the blood. A brushless direct current (BLDC) motor powers the Intra-arterial blood pump.

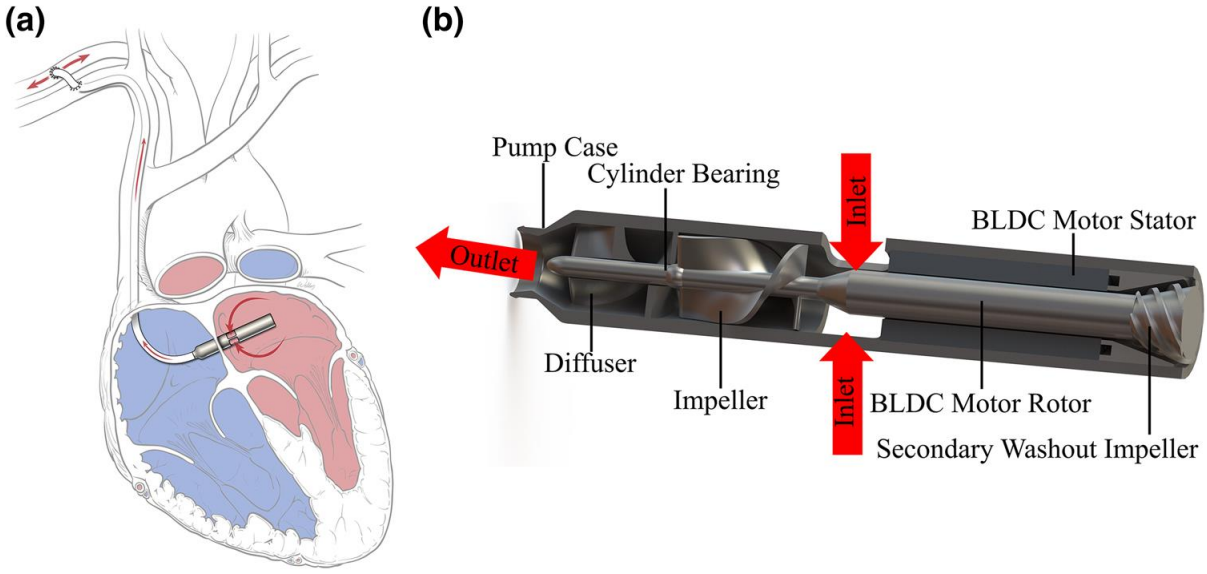

Figure 8: Intra-atrial blood pump prototype. A) The location of the Intra-arterial blood pump in the heart. The left ventricle is smaller and compromised compared to a regular left ventricle. B) Cross-section of intra-atrial pump. Image courtesy (Smith et al., 2019). (Smith et al., 2019)

Another axial impeller, similar to the Intra-arterial blood pump, is the Aortix intra-aortic pump by Kapur et al. (2020) (Figure 9). The Aortix is a 6.5cm long impeller pump powered by a BLDC motor with a diameter of 6 mm designed by the company Maxon motors ("Circulatory Support without Surgery for Heart Failure Patients," 2020). The impeller of the Aortix is mounted within a self-expanding nitinol strut anchoring system. The Aortix is implanted inside the aorta and intended to provide short-term hemodynamic support by accelerating the downstream flow in the descending aorta. In contrast to the intra-atrial pump, the pump does not have to work against a pressure gradient, and the blood is propelled forwards instead of perpendicular. These devices show the potential to develop implantable cardiac assist devices without the need for major surgery.

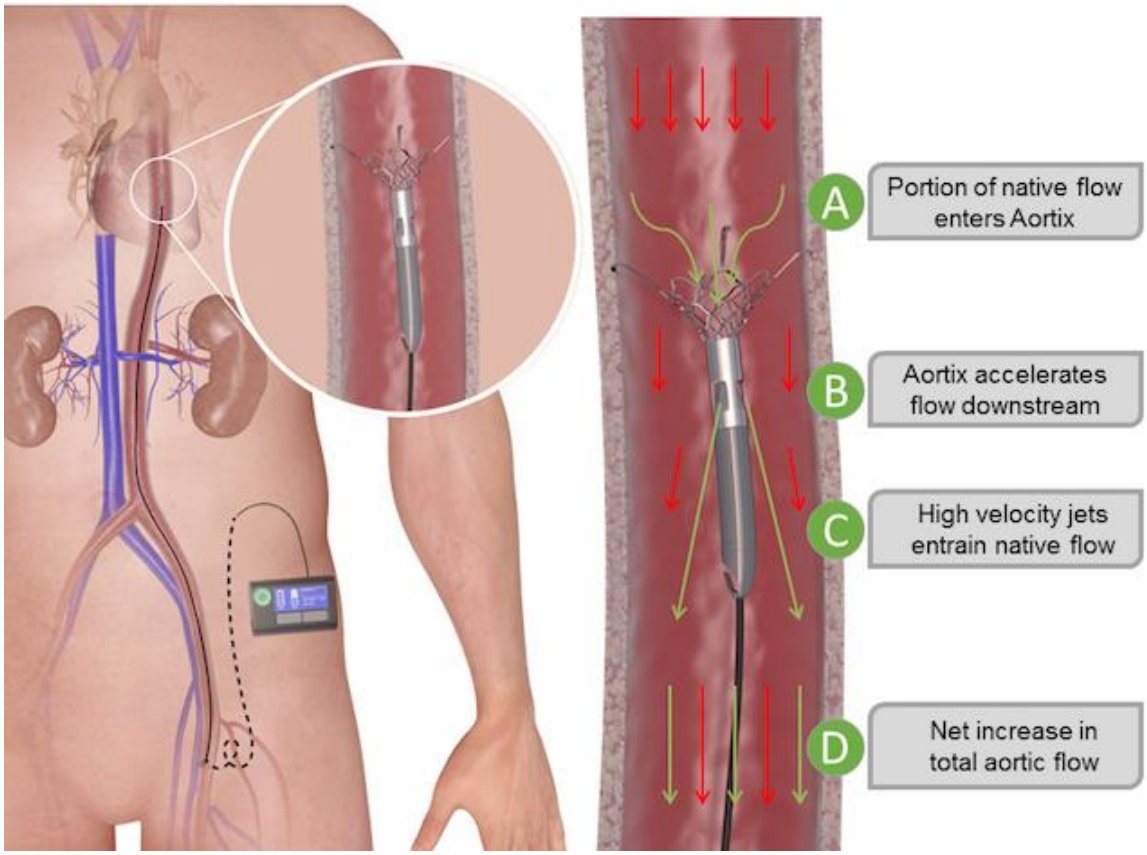

Figure 9: Intra-arterial blood pump by Kapur, Esposito, and Wihiteheed (2020). The pump is placed in the ascending aorta.

2.5 Circulatory assist devices for Fontan circulation

As mentioned earlier, a cardiac assist device can reduce systemic venous pressure while maintaining cardiac output (Griselli, Sinha, Jang, Perri, & Adachi, 2018). Multiple studies have evaluated the treatment options with various mechanical assist devices for patients with Fontan circulation (Chopski, Moskowitz, Stevens, & Throckmorton, 2017; Giridharan et al., 2014; Griselli et al., 2018; Imielski, Niebler, Kindel, & Woods, 2017; Nathan et al., 2006; Newcomb, Negri, Brizard, & d'Udekem, 2006; Throckmorton et al., 2011). In 29% of patients with Fontan circulation, cardiac assist devices are used as a bridge to transplant (Chopski et al., 2017). Ventricular assist devices unload the dysfunctional single ventricle, reduce its volume and external work, and augment the myocardial supply-demand ratio (Giridharan et al., 2014; Griselli et al., 2018). However, a ventricular assist device supporting the systemic circulation cannot directly support the blood flow through the Fontan circuit and pulmonary circulation. They cannot reduce the systemic venous pressure or increase the single ventricle preload. Although there are reports on successful use of the ventricular assist devices to support the failing Fontan patients for a short period, but the long-term results remain poor (Newcomb et al., 2006). The implantation of ventricular assist device to support the pulmonary circulation or total artificial heart in a Fontan patient also requires a surgical modification of the TCPC to ensure efficient systemic venous and pulmonary flow (Nathan et al., 2006). This modification is required because the cannulation of the valveless TCPC circuit reduces the forward flow due to the recirculation. Furthermore, a collecting chamber for the systemic venous return needs to be created during the total artificial heart implantation, complicating the surgery, and substantially increasing its risk. Another significant drawback of the currently available cardiac assist devices implanted into the TCPC circuit is that the device becomes the only path to the pulmonary circulation leading to lethal consequences in case of device malfunction.

The current cardiac assist device technologies, thus, are not optimal for providing mechanical support to the blood flow through the Fontan circuit. Therefore, a cardiac assist device that can function within the low-pressure and high-compliance environment of the TCPC is required. The device should simultaneously reduce the systemic venous pressure and increase the pulmonary arterial pressure to resemble the normal

circulation more closely. Unfortunately, such a device is not yet available, but several research groups focus on developing such a specific assist device for Fontan circulation (Granegger et al., 2019; Rodefeld et al., 2010).

One of the first concepts of a Fontan-specific cardiac assist device uses two micro axial pumps placed within both inflows into the TCPC (Figure 10) (Rodefeld et al., 2003). A drawback of this system is that the two axial pumps supporting the double inflow and outflow of the TCPC connection need to be perfectly synchronized to provide the pressure elevation in the opposing venous territory. Lacour-Gayet et al. (2009) suggested a Y-shaped three-way modification to overcome the necessity of two pumps; however, this increases the surgery's complexity. Also, due to the high rotational velocity, the pumps create an increased risk of inlet collapse due to the suction effect (Kennington et al., 2011). Another major drawback is that the micro axial pump obstructs the blood flow in case of a malfunction with potentially lethal consequences.

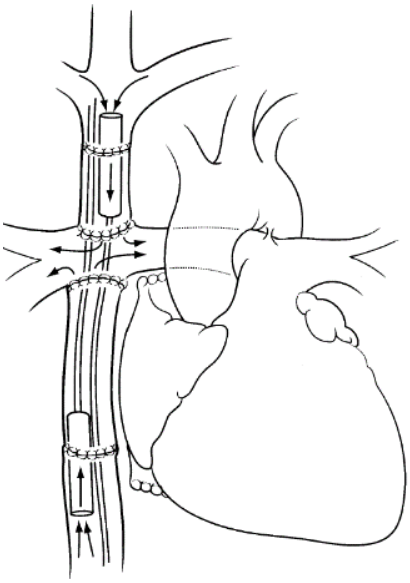

Figure 10: Axial pumps are positioned above and below the TCPC in the inferior vena cava and the superior vena cava to propel the blood flow forward and into the pulmonary arteries. (Rodefeld et al., 2003).

2.5.1 Cavopulmonary pump by Granegger et al. (2019)

Granegger et al. (2019) eliminated the need for two pumps by developing a cavopulmonary pump that replaced the TCPC (Figure 11). The pump is intended to replace the subpulmonary ventricle in young adolescents up to adult patients. The pump is designed to have minimal wear and an operation time of at least ten years. The pump consists of two inlets and two outlets with an impeller suspended in the middle. The actuation system of the cavopulmonary pump consists of two axial three-phase synchronous actuators (Figure 12). Mechanical bearings fix the impeller's position between two flow straighteners at the inlet based on the Heartmate II rotary blood pump. This system permits a small pump size to have large fluid gaps like 0.5mm gaps between the impeller blade and the upper and lower housing walls are incorporated to permit a good washout for the secondary flow. It also ensures the cooling of the adjacent motor coils and prevents pump thrombosis. Gaps larger than 0.5 mm allow floating thrombi to pass the pump. The cavopulmonary pump does have a significant disadvantage in that the implantation requires a major surgery.

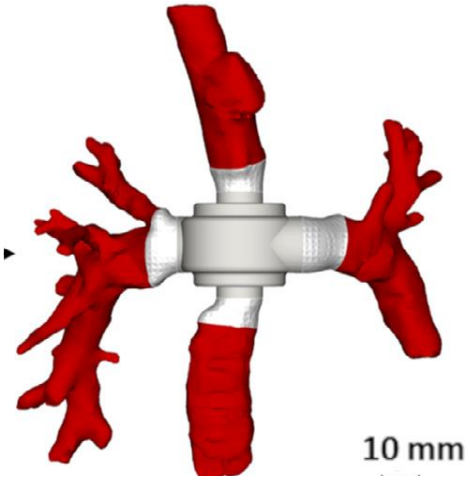

Figure 11: Implantation of the cavopulmonary pump in the total cavopulmonary connection. The cavopulmonary pump is depicted including the connected vena cava and the pulmonary arteries. Image courtesy (Granegger et al., 2019)

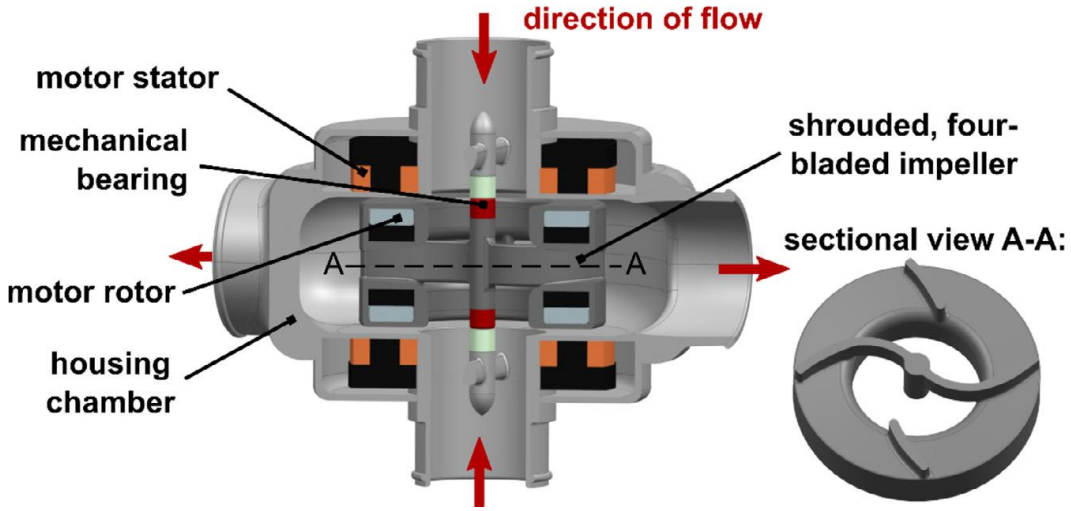

Figure 12: Cavopulmonary pump with two axial flux three-phase synchronous motors. Each motor consists of 12 coils and the rotor has 8 poles of surface-mounted permanent magnets. The impeller blade has a diameter of 19mm, sectional view A-A. Image courtesy (Granegger et al., 2019)

2.5.2 Tesla Pump by Cysyk et al. (2019)

Similar to the cavopulmonary pump by Granegger et al. (2019), the pump by Cysyk et al. (2019) replaces the TCPC (Figure 13a). The inlets ports of the pump are directly connected to the inferior and superior vena cava and the outlet to the pulmonary artery. The bladed rotor consisting of 3 to 5 thin and flat parallel disks is responsible for the viscous impeller propelling of the blood and is suspended by the hydrodynamic bearing depicted in Figure 13b. The shape of the bladed rotor is such that stagnation of blood is eliminated surrounding the blades. A stator surrounds the rotor and thereby powers the rotor. Cysyk et al. (2019) implanted the Tesla pump inside a sheep in which a Fontan circulation was created for 30 days. The test was successful, and the pump demonstrated adequate circulatory support. In addition, the sheep showed normal physiological pulmonary and venous pressures.

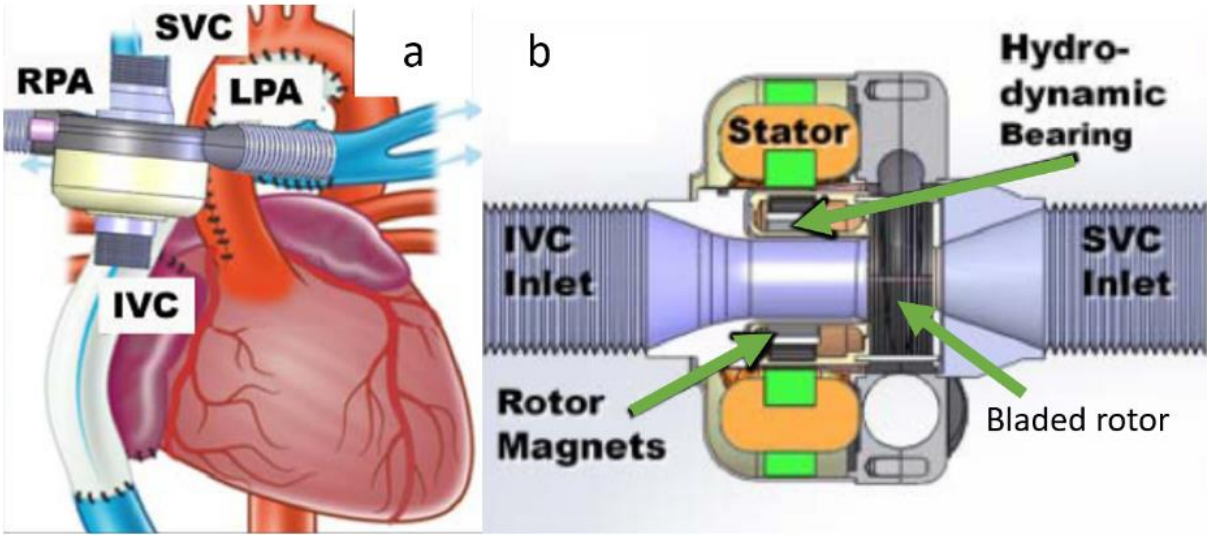

Figure 13: a) The Tesla implanted in the Fontan circulation. The picture depicts the pump as a replacement of the TCPC. b) Schematic depiction of the Telsa pump showing the two inlets, the stator rotor, and the location of the bladed rotor. Image courtesy (Cysyk et al., 2019).

2.5.3 VIP by Rodefeld

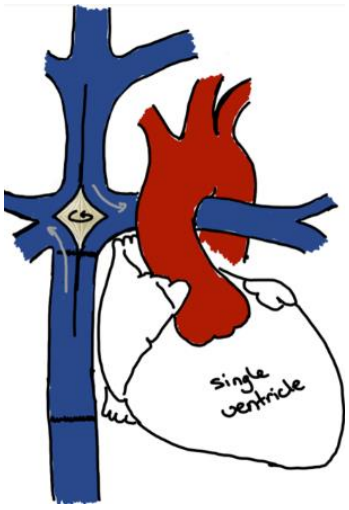

Figure 15: The VIP inside the TCPC propelling the incoming flow from the inferior vena cava and the SVC forwards into the pulmonary arteries.

In 2009, the research group led by Rodefeld (Rodefeld et al., 2011) proposed another solution; a biconical VIP placed at the intersection of the inflows and outflows of the TCPC (Figure 14). The proposed VIP is based on the Von Kármán viscous pump principle, in which a flat disk rotating in a fluid induces rotation in the surrounding fluid due to the no-slip condition (Figure 15) (Rodefeld et al., 2011). The centrifugal forces created by the rotating fluid generate a radial outflow. The fluid's radial outflow is accompanied by the fluid's axial inflow from the far-field towards the disk due to volume conservation.

The blood inflow from both the inferior vena cava and the superior vena cava is drawn into the TCPC by the VIP and then propelled into the left and right pulmonary artery. Due to its biconical configuration, such a VIP does not cause TCPC pathway obstruction in a static position. The VIP decreases the turbulent flow energy loss by optimizing the fluid transfer through the TCPC. Therefore, if the VIP fails, this flow optimization counteracts any obstructive potential. The VIP provides a low-pressure, high volume flow, which can replace the normal subpulmonary ventricle hemodynamics. There is no backpressure elevation in the vena cavae due to the inlet suction created by the VIP. Also, the risk of vein collapse and cavitation is reduced by a high degree of fluid slip, thereby avoiding excessive pressure rise and risk of perfusion injury to the lungs. The original design of the VIP proposed by Rodefeld's group was intended to be minimally invasive implantable through a catheter-based procedure with the actuator outside the body.

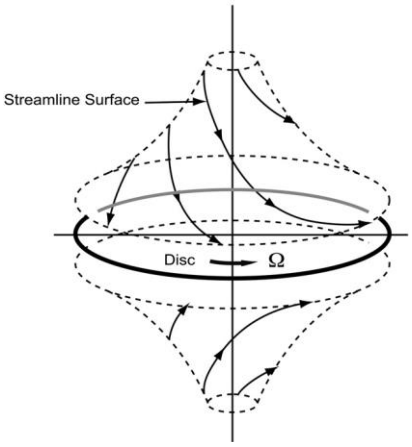

Figure 14: Schematic presentation of the flow streamlines by the rotating disk of the Von Kàrmàn principle. Image courtesy (Panton, 2013)

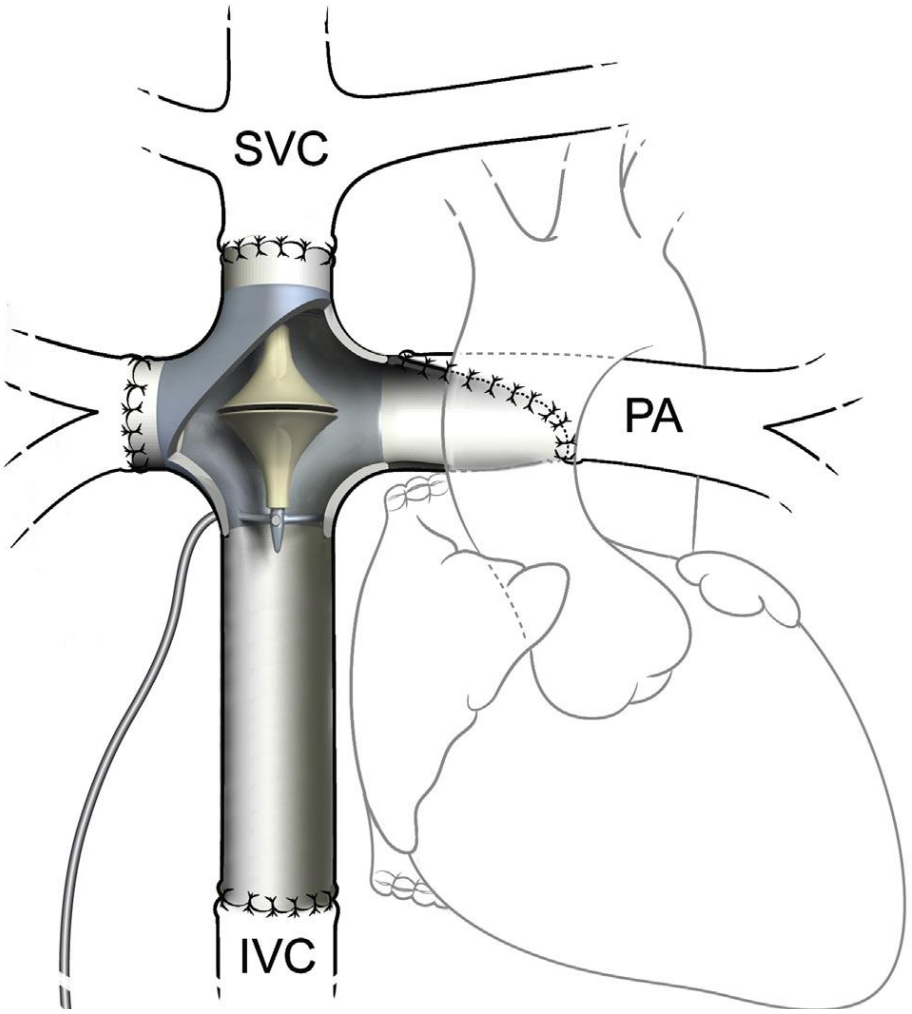

Figure 16: Conceptual pump implantation by Rodefeld et al. (2019) that replace the complete TCPC.

After introducing the design, the group of Rodefeld has published several in vitro and computational fluid dynamics simulations of the device positioned within the 4-way intersection with idealized geometry simulating the TCPC, showing promising results (Y. Delorme et al., 2013; Kennington et al., 2011; Kerlo et al., 2013). These simulations concluded that the VIPs' performance is relatively insensitive to different inlet conditions and flow rate changes. In addition, the VIP provides a nearly stable mechanical cavopulmonary flow assistance under different physiological conditions, corresponding to rest and exercise conditions. No cavitation was observed over the VIP operational range. Cavitation is the formation of small vapor-filled cavities in the fluid where the pressure is relatively high due to a rapid change in pressure; this can damage the blood cells. Furthermore, the VIP generates a low-pressure Fontan flow augmentation while not exceeding shear stress levels that could cause hemolysis (further explained in the next section).

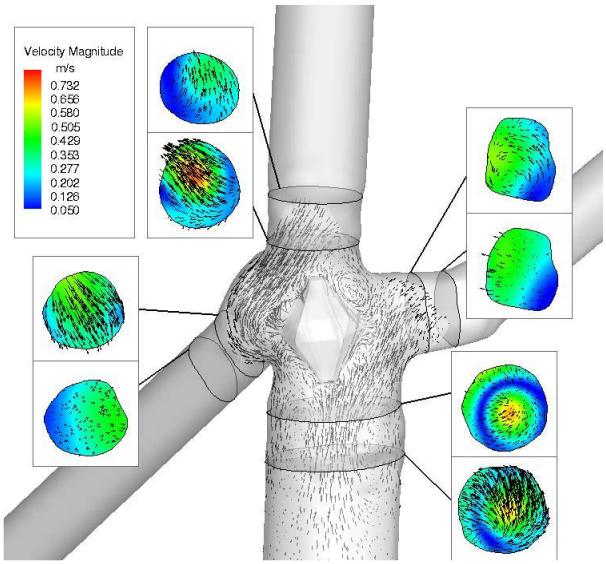

Figure 17: The velocity fields of the flow generated by the VIP inside a MRI-based patient specific TCPC geometry, by DeGan et al. (2011). The lines show the recirculation of the blood.

However, Rodefeld et al. (2019) changed the design of the catheter-based VIP to a new rigid 4-way case intended to replace the TCPC intersection, requiring, thus a major surgical procedure (Figure 16). The idea of replacing the TCPC intersection by the integrated VIP is similar to the design proposed

in the research of (Granegger et al., 2019). Unfortunately, minimal information is available for the motivation to change the design; besides the limited computational fluid dynamics studies of the VIP performance within a patient-specific TCPC geometry based on only two MRI datasets of the TCPC circuits (DeGan et al., 2011). The previous studies of the VIP were conducted in idealized geometry (Figure 14). From patient-specific TCPC geometry studies, DeGan et al. (2011) concluded that the VIP could not function properly within a patient-specific TCPC geometry intersection due to increased pressure gradient from the inlet to the outlet and induction of recirculation near and below the VIP (Figure 17). As discussed in the next chapter, recirculation and flow stagnation areas concern the increased risk of thrombus formation.

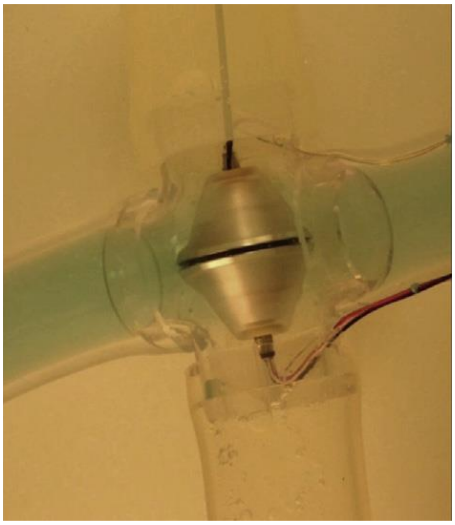

Figure 18: Screenshot of the video showing the secondary flow path. The blue fluid is contrast injections that selectively flow through the internal flow path, with dispersion of outflow at the equatorial midline. Image courtesy (Rodefeld et al., 2019)

The new design housing has a double inlet, double outlet, thin-walled, and hard case shell that suspends the impeller pump and serves to direct the TCPC flow. In the center of the VIP, a stator is located containing iron laminations and copper windings. Around the stator, a biconical rotor is placed containing the magnets, which are along with the rotor the only moving part of the device. The surface vanes that provide the low-pressure, high-volume augmentation of the cavopulmonary flow are located on the outside surface of the rotor. The electric wires from the stator go through the central shaft and exit the housing via struts holding the shaft in place. An additional flow path is created in the new design allowing for a secondary internal blood flow between the motor and the impeller (Figure 18). This secondary internal flow allows for electromagnetic flux transfer for motor torque, heat dissipation, bearing lubrication, and to reduce the risk of recirculation and thrombosis. The internal flow path allows for inflow at each axial end, with outflow at the equatorial gap in the biconical impeller. The experiments concluded that the heat dissipation was excellent, confirmed by reduced core temperature at higher rotation velocity and by no measurable increase in blood analog temperature (<0.1°C).

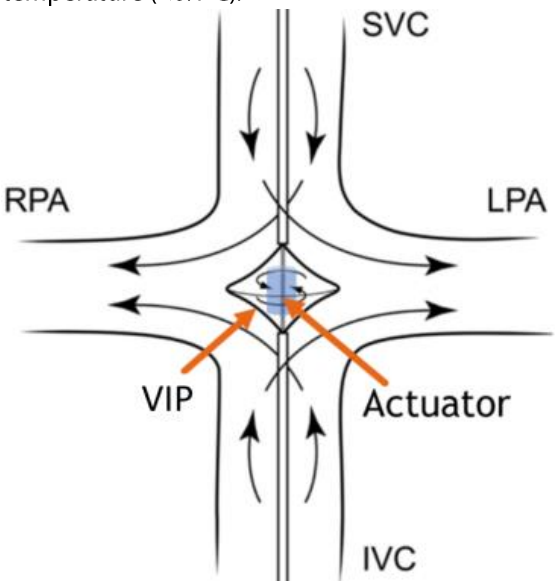

Figure 19: Sketch of the TCPC with the VIP. The black arrows indicate the direction of blood flow induced by the impeller rotation (indicated by the arrows drawn inside the impeller). The blue cylinder is where the actuator will be placed. Image courtesy (Rodefeld et al., 2010)). IVC, inferior vena cava; LPA, left pulmonary artery; RPA, right pulmonary artery; SCV, superior vena cava.

Before completely disregarding the original catheter-based VIP, more research should be conducted because of the lack of information about the change in design and very limited and oversimplified analysis of the patient-specific TCPC geometries in the computational fluid dynamic simulations. The new proposed design for the VIP is not attractive due to the required major surgery in patients with an already compromised hemodynamic balance. Until very recently, in all the experiments by the group of Rodefeld et al. (2013), only the pump's impeller has been tested powered by an external motor. There has not been an actuator developed to power the pump. To continue with the development of the catheter-based VIP first needs to investigate if a small enough actuator can be designed to sufficiently power the VIP (Figure 19).

3. Electric motor theory

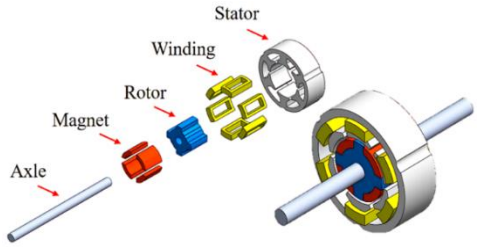

Figure 20: Exploded view and assembly drawing of the inset permanent magnet synchronous motor. The motor consists of a stator with six yokes, a 60 windings coil winding, a rotor containing four permanent magnet poles, and an axle (image courtesy (Pang et al., 2020)

A thorough literature study was performed to investigate the possible actuators that could fit into the VIP. The literature study concluded that the actuator model proposed by Pang et al. (2020) could be a good starting point to design the actuator (Figure 20). This actuator is an inrunner permanent magnet synchronous motor (PMSM) selected because of the reported high torque output for its relatively small size. However, the actuator discussed in the Pang et al. (2020) research needs to be scaled-down to fit into the VIP. In addition, the Pang et al. (2020) actuator design needs to be converted to an outrunner configuration to be easily attached to the VIP. The actuator by Pang et al. (2020) is an electric motor.

Therefore, in this chapter the electric motor's main components and functioning are given. This is described based on the BLDC motor because it is one of the most general types. Because the actuator by Pang et al. (2020) needs to be reduced in size, the consequences of scaling down the actuator are also mentioned. After that, the inrunner and outrunner configurations are described to understand the differences when converting this actuator to an outrunner. Then the difference between the PMSM and BLDC is described to provide a basis to make the best design choice. Heat is produced in the electric motor when losses occur, which is undesirable. Therefore, the losses and thereby efficiency is described.

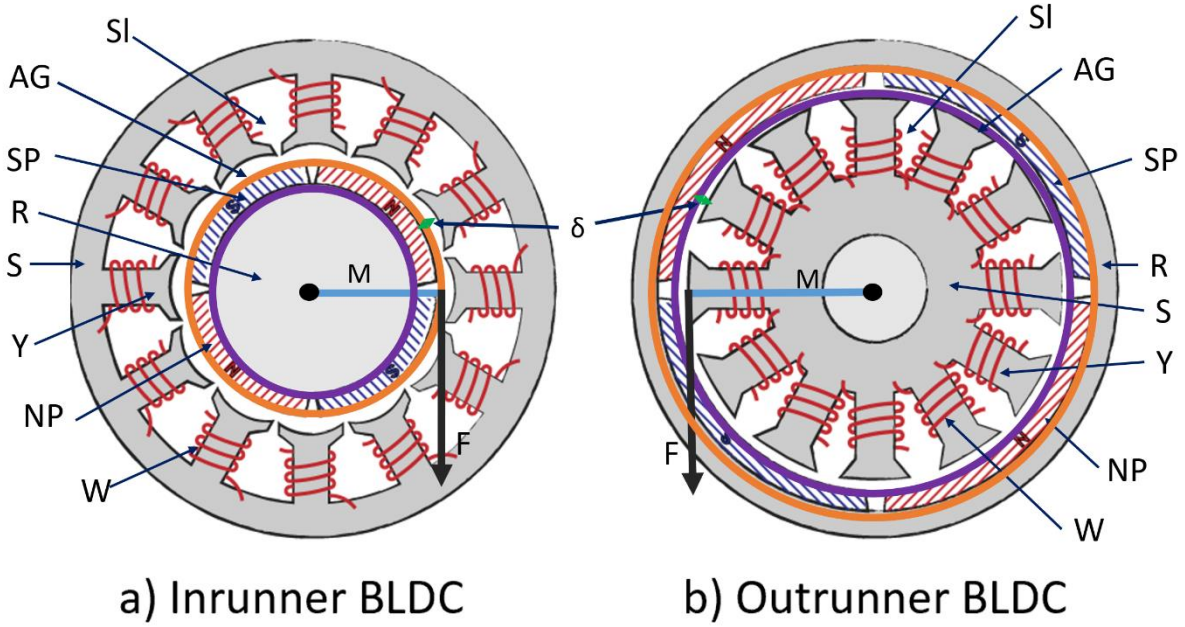

Figure 21: Simplified schematics of an inrunner and an outrunner radial flux BLDC motor. a) The stator outside the inrunner has 12 yokes, all wrapped with a coil. The permanent magnet south and north poles are attached to the rotor which rotates. b) The configuration is the opposite; the rotor rotates around the stationary stator. The blue lines indicate the moment and moment arm, and the black dot the centre of the actuator The orange circle is the outer diameter of the rotor and the purple the inner diameter of the rotor. The green arrows indicate the air gap length (image courtesy ("Brushed vs. Brushless Motors," 2020)).AG, Air gap; δ, air gap length; F, Lorentz force M, moment arm; NP, north pole permanent magnet; R, rotor; S, stator; Sl, Slot; SP, south pole permanent magnet; Y, yoke; W, windings

The main components of a BLDC motor are the stator (S) and the rotor (R) given in Figure 21 (Hanselman, 2003). The stator and rotor are separated by a small air gap (AG). The stator has several yokes (Y) onto which wire windings (W) are wrapped. A power source provides a current flow through these wires. Permanent magnets are attached circularly on the rotor with alternatingly north and south poles (Np and SP) facing the yokes of the stator. Figure 22 shows the different variables of an electric motor.

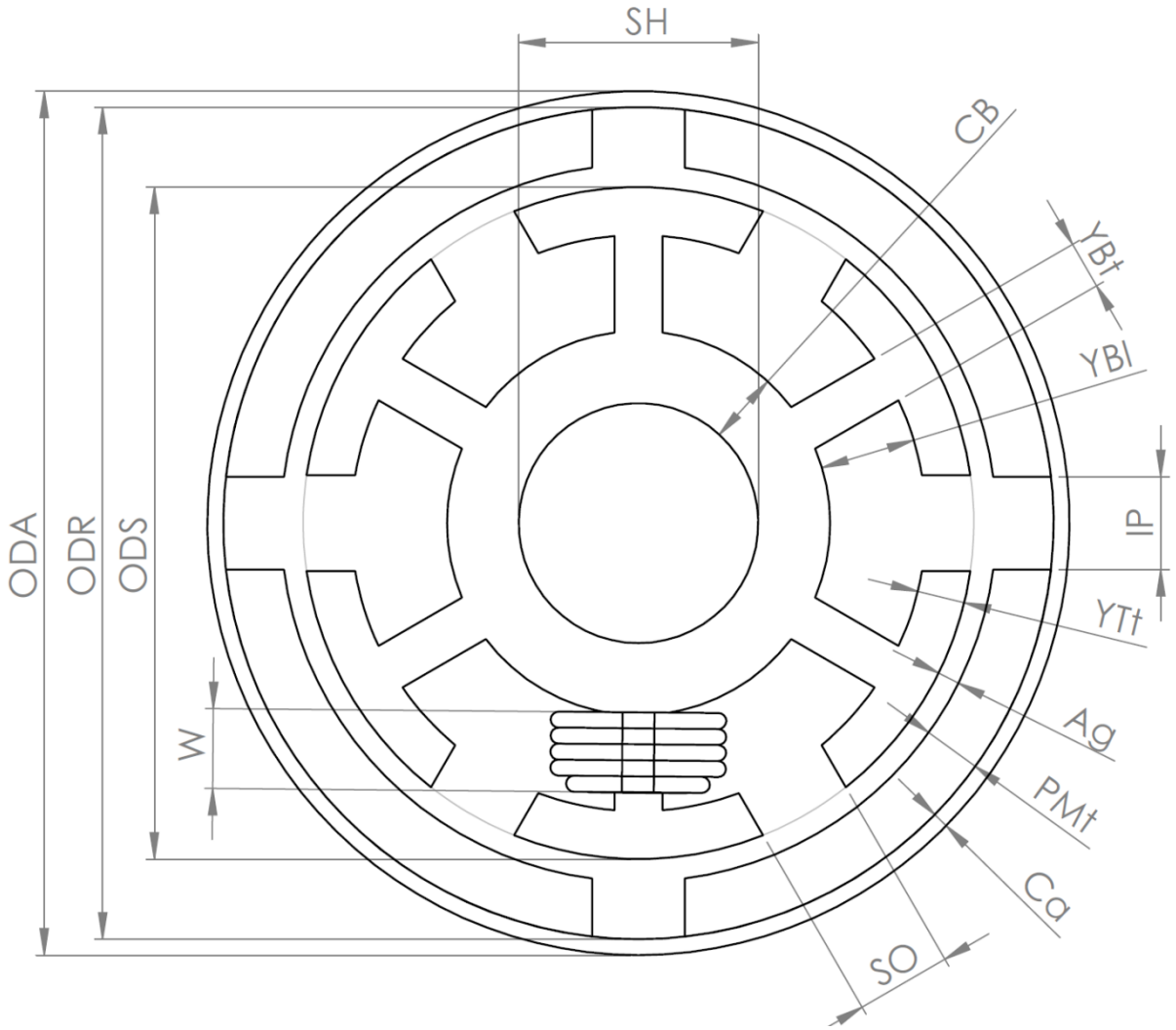

Figure 22: Dimensions of an outrunner BLDC motor. Ca, Case; CB, Core back length; IP, interpole length; ODA, outer diameter of the actuator; ODR, Outer diameter of the rotor; ODS, Outer diameter of the stator; PMt, Permanent magnet thickness; SH, Shaft hole diameter; SO, Slot opening; YBl, Yoke base length; YBt, Yoke base thickness; YTt, Yoke top thickness

A direct current powers the BLDC motor. This current flows through the windings, thereby creating a magnetic field in the air gap. This magnetic field moves around in the air gap since the coils alternately switch on and off. The interaction between the created magnetic field and the magnetic field generated by the permanent magnets on the rotor causes a Lorentz reaction force to the rotor. Torque is created through the moment arm (M), which rotates the rotor of the actuator.

3.1 Output torque

Next, the output torque equation is provided to gain more insights into the parameters that influence the torque, and the formula is later used to validate the designed actuator. The torque calculation in an electric motor is based on the (tangential) Lorentz force equation (Reichert et al., 2009):

$$F = \mathrm{NB_g L_{st}} i \quad (3.1)$$

- F_L Lorentz force [N]
- N number of windings

- B_g air gap flux density [T]
- L_{st} axial stack length [m]
- i_{in} input current [A]

Torque is the rotational force causing the actuator to rotate around its axis (Figure 21). Torque is calculated by multiplying the applied force and the moment arms vector from the point of the applied force to the axis (Serway & Jewett, 2018). In an actuator, the moment arm is the distance from the actuator's center point to the point of application of the force, and this distance is the outer radius of the rotor. The force is caused by the interaction between the rotor and stator, which happens in the air gap. This results in the following equation (Hanselman, 2003):

$$|\tau| = 2N_m \mathrm{N B_g L_{st} R_{ro}} i \quad (3.2)$$

- τ torque [Nm]
- R_{ro} the outer radius of the rotor [m]
- N_m number of poles

In Eq. 3.2, the factor 2N is added because each slot has windings from both sides, contributing to the generation of torque (Hanselman, 2003). For the torque Eq. 3.2, the air gap flux density is not yet known and needs to be calculated.

It is assumed that the equation for the air gap flux density is the same for an inrunner and an outrunner because the equation describes the interaction of the flux density to the air gap. Therefore, the configuration should not influence the air gap flux density. To calculate the air gap flux density, Ye and Yao (2018) provide an equation to calculate this analytically for an outrunner PMSM. The number of poles does not appear in the equation because the flux crossing the air gap is not a function of the number of poles (Hanselman, 2003). The equation for the air gap flux density is as follows (Ye & Yao, 2018):

$$B_g = \frac{4B_r R_m R_l}{\left[\frac{2R_l R_s \delta}{\mu_0 S_{ag}} + (R_r + 2R_m) \cdot \left(\frac{2\delta}{\mu_0 S_{ag}} + R_s R_l\right)\right]} \quad (3.3)$$

- B_g air gap flux density [T]
- B_r the residual flux density [T]
- R_m the reluctance of the magnet pole [H^{-1}]
- R_l the reluctance due to magnet to stator flux leakage [H^{-1}]
- R_s the reluctance of the stator core [H^{-1}]
- δ air gap length [mm]
- μ_0 air permeability [N/A^2]
- S_{ag} the surface area of the air gap [mm^2]
- R_r the reluctance of the rotor core [H^{-1}]

To calculate the R_m, R_s, R_r, Ye and Yao (2018) provided the the following equations:

$$R_m = \frac{h_m}{\mu_0 \mu_r S_m} \quad (3.4)$$

- h_m magnet thickness [m]
- μ_r relative permeability of the magnet [N/A^2]
- $\mathrm{S_m}$ magnet area perpendicular to the magnetizing direction [m^2]

$$R_s = R_r = 0.01\, R_g \quad (3.5)$$

- R_g the reluctance of the air gap [H^{-1}]

$$R_g = \frac{\delta}{\mu_0 S_{ag}} \quad (3.6)$$

Fill in (3.6) into (3.5) gives:

$$R_s = R_r = \frac{0.01\delta}{\mu_0 S_{ag}} \quad (3.7)$$

The parameter R_l, the reluctance due to magnet-to-stator-flux leakage in the equation can be neglected according to Ye and Yao (2018) and is thereby set at 1. Filling in equations (3.4) and (3.7) into (3.3) will give the following equation:

$$B_g = \frac{4B_r \frac{h_m}{\mu_0 \mu_r S_m}}{\left[\frac{2\delta}{\mu_0 S_{ag}} \cdot \frac{0.01\delta}{\mu_0 S_{ag}} + \left(\frac{0.01\delta}{\mu_0 S_{ag}} + 2\frac{h_m}{\mu_0 \mu_r S_m}\right) \cdot \left(\frac{2\delta}{\mu_0 S_{ag}} + \frac{0.01\delta}{\mu_0 S_{ag}}\right)\right]} \quad (3.8)$$

Further elaboration of this equation gives:

$$B_g = \frac{\frac{4B_r h_m}{\mu_r S_m}}{\left[\frac{0.0401\delta^2}{\mu_0 S_{ag}^2} + \frac{4.02\delta}{\mu_0 \mu_r S_m S_{ag}}\right]} \quad (3.9)$$

The surface area of the air gap, S_{ag} and the magnet area perpendicular to the magnetizing direction, S_m can be calculated from the known variables (Figure 23). The fringing flux needs to be considered to calculate the surface area of the air gap (Mohan, 2012). The fringing flux is the magnetic flux in a magnetic core that spreads out into the surrounding medium (Figure 23). The surface area of the air gap, S_{ag}, is calculated using the following equation for an inrunner actuator:

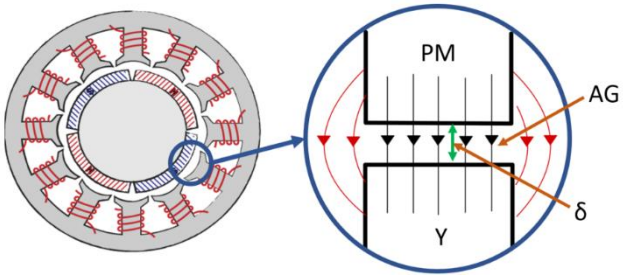

Figure 23: The black arrows indicate the magnetizing direction, and the red arrows the fringing flux surrounding the air gap. AG, Air gap; δ, air gap length; PM, permanent magnet; Y, Yoke.

$$S_{ag} = (\pi * R_{ro} + \delta) * (L_{st} + \delta) \quad (3.10)$$

The magnet area perpendicular to the magnetizing direction, S_m, is calculated with the following equation for an inrunner actuator:

$$S_m = \pi * R_{ro} * L_{st} \quad (3.11)$$

For an outrunner actuator, instead of the outer diameter of the rotor, the inner radius of the stator needs to be used. This is because both equations (3.10) and (3.11) are related to the air gap. The outer diameter of the rotor in an outrunner does not border the air gap, but the inner diameter does, see Figure 21.

Filling in the equations (3.10) and (3.11) in the equation of the air gap flux density (3.9) gives:

$$B_g = \frac{\frac{4B_r h_m}{\mu_r \pi R_{ro} L_{st}}}{\left[\frac{0.0401\delta^2}{\mu_0((\pi R_{ro} + \delta)(L_{st} + \delta))^2} + \frac{4.02\delta}{\mu_0 \mu_r \pi R_{ro} L_{st}((\pi R_{ro} + \delta)(L_{st} + \delta))}\right]} \quad (3.12)$$

Filling in (3.12) into (3.2) gives the following equation for the torque:

$$|\tau| = \frac{8N\mathrm{L_{st}R_{ro}}i\frac{B_r h_m}{\mu_r \pi R_{ro} L_{st}}}{\left[\frac{0.0401\delta^2}{\mu_0((\pi R_{ro} + \delta)(L_{st} + \delta))^2} + \frac{4.02\delta}{\mu_0 \mu_r \pi R_{ro} L_{st}((\pi R_{ro} + \delta)(L_{st} + \delta))}\right]} \quad (3.13)$$

Validation of the torque equation

The equation described above is validated with variables for the small electromotors derived from the articles' by Kim, Lee, and Kim (2014) and Pang et al. (2020). The input variables not reported in these articles are taken from the internet resources and are given in Table 1. Air permeability is a general value (Cullity & Graham, 2011). A magnet's relative permeability depends on the material of the magnet (Pyrhonen, Jokinen, & Hrabovcova, 2013). In the actuator of Pang et al. (2020), the magnets are made from sintered NdFeB, grade N48H with radial magnetization (Teslar Technology Co., Ltd., Taichung, Taiwan) ("Sintered Neodynium-Iron-Boron Magnets," 2021). Kim et al. (2014) did not report the type of magnet used; however, it is assumed that permanent magnets are made of NdFeB because it is the most common magnet used in BLDCs. The residual flux density, also called the remanence, is the magnetization left behind in a ferromagnetic material after an external magnetic field is removed. This value is also dependent on the magnet's material and is 1.39T for Neodymium magnets ("Sintered Neodynium-Iron-Boron Magnets," 2021). Table 1 provided the results obtained from the given equation along with the variables.

Table 1: Parameters for the torque equation from the articles by Kim et al. (2014) and Pang et al. (2020) and the torque results.

Parameter	Symbol	Unit	Values for validation with Kim et al. (2014)	Values for validation with Pang et al. (2020)	Origin of the values
Number of windings	N	-	21	60	Actuator article
Axial stack length	L_{st}	m	0.030	0.005	Actuator article
The outer diameter of the rotor	R_{ro}	m	0.0096	0.0037	Actuator article
Current	i	A	3.87	1	Actuator article
Residual flux density	B_r	T	1.39	1.39	Datasheet of the magnet
Magnet thickness	h_m	m	0.0026	0.001	Actuator article
Relative permeability of the magnet	μ_r	-	1.05	1.05	(Pyrhonen et al., 2013)
Air gap length	δ	m	0.0004	0.0004	Actuator article
Air permeability	μ_0	N/m	1.257×10^{-6}	1.257×10^{-6}	(Cullity & Graham, 2011)
Torque calculated by the article's authors	$\tau_{article}$	µNm	21,200	2927	Actuator article
Calculated torque by the equation	$\tau_{calculated}$	µNm	22,066	2495.9	-
Difference	$\Delta\tau$	µNm	+4.09%	-14.73%	-

As shown in Table 1, the calculations result in an average difference of -5.32% between the torque reported by the authors and the calculated torque. The difference in analytical calculations and the calculated torque the article reports could explain due to the differences in values derived from other sources than the original articles.

3.2 Scaling down of an electric motor

The actuator given by Pang et al. (2020) needs to be reduced in size, which has potential consequences for the torque output of the actuator. In the next section, the torque production in the actuator is described, followed by the consequences of scaling down the actuator. Two main factors cause a reduction in torque in

a more miniature actuator, including the reduced size and the consequences of the reduced size for the input current (Eq. 3.2).

The reduced size causes the torque in an actuator to decrease because the torque generated in the electric motor is proportional to the volume of the motor (Mekid, 2010). In an equation, this can be described as (Hanselman, 2003):

$$\tau = kD^2L_{st} \quad (3.14)$$

- τ torque [Nm]
- k a constant
- D overall outer diameter of the actuator [m]

Eq. 3.14 is a simplified version of Eq. 3.2. The diameter R_{ro} here is substituted by D, the constant k is a combination of the number of poles and the other variables. As one can see from Eq. 3.14, the diameter significantly influences the motor's torque.

Besides the volume of the actuator, the current has a direct influence on the actuator. Scaling down the actuator requires the diameter of the wires to be scaled-down as well to retain the number of windings per stator's yoke. Large actuators contain wires with a large diameter allowing a larger current, resulting in higher torque. A more miniature actuator inherently has fewer windings than a large actuator due to the reduced space. In small electric motors, the wire is smaller in diameter, which causes higher resistance leading to the generation of more heat at a lower current compared to a motor with wires of large diameter. Decreasing the thickness of the yokes increases the space in the slots. However, the tooth's flux saturation limits the reduction in yokes thickness (Sensinger, Clark, & Schorsch, 2011). In addition, the thickness of the yokes needs to be large enough to withstand the mechanical force applied upon them by the magnetic field.

3.3 Difference between an inrunner and outrunner

All the small actuators in the literature study and available on the commercial level are found to be inrunner actuators. However, for the current application, an outrunner-type motor is the preferred option. Therefore, a comparison between the two types of actuators is made.

The difference between an inrunner and an outrunner motor is the position of the stator and the rotor (Figure 21). In an inrunner, the rotor is in the centre of the actuator, surrounded by the stator. The inrunner has a compact set-up because the rotor is very thin, a thin rotor leaves more space for the stator and increases the number of windings per yoke of the stator (Reichert et al., 2009).

Table 2: Overview of the comparison between an inrunner and outrunner actuator.

Parameters	**Inrunner**	**Outrunner**
Moment arm	Smaller	Larger
Torque	Lower	Higher
RPM per volt	Higher	Lower
Efficiency	Higher	Lower
Heat dissipation	Better	Worse
Poles/ coils ratio	More slots than poles	More poles than slots

There are several consequences of the different configurations of inrunner and outrunner electric motors (Table 2). First, the moment arm (M) of an inrunner is usually smaller than an outrunner as indicated in Figure 21, resulting in a lower torque as compared to the latter. Also, the effects of scaling the inrunner and the outrunner are found to be different. The relation between the change in torque output and the scaling down depends on different dimensional parameters in an outrunner and an inrunner (Reichert et al., 2009). For an inrunner, the reduction in torque depends on the surface area of the stator, the total machine radius, and the air gap.

$$\frac{\tau}{c_F * \pi * R^3} = x_A * \sqrt{1 - x_{SAMA}} \quad (3.15)$$

- c_f force constant
- R_{ao} the outer radius of the actuator [m]
- x_{SAMA} the ratio of the stator area to the motor area

The scaling down of an outrunner is only dependent on the changes in surface area of the air gap radius. Therefore, the above equation is modified as follows:

$$\frac{\tau}{c_F * \pi * R^3} = \sqrt{x_{SAMA}^3} \quad (3.16)$$

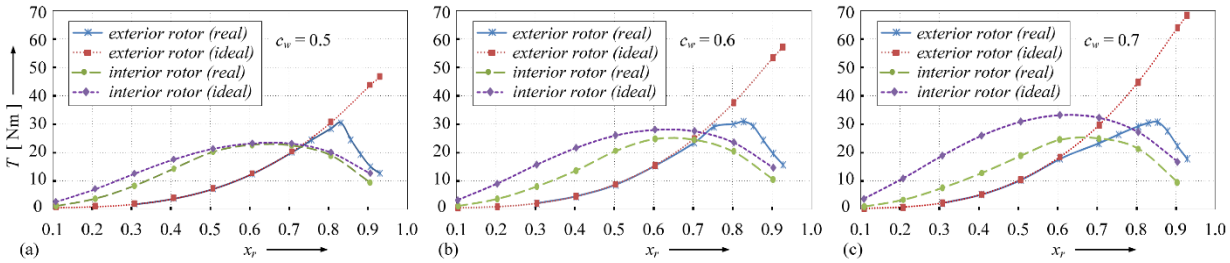

Figure 24: Results of the torque simulation with ideal and realistic constraints for different stator winding space factor values. a) 0.5, b) 0.6, and c) 0.6 (Image courtesy (Reichert, Nussbaumer, & Kolar, 2009)) c_w, winding space factor; T, Torque; x_r, the ratio of the air gap radius to the outer actuator radius.

Figure 24 shows that using an inrunner is beneficial for a small ratio of air gap radius to the actuator radius. Theoretically, the outrunner can produce the highest torque when the most significant possible air gap is considered. However, the maximum achievable ratio of the air gap to the outer radius of the actuator, x_r, depends on the radial thickness of the magnets attached. The maximum torque can be found for an outrunner when the stator area is as large as possible, leaving enough space for the rotor to produce the required magnetic field. In an inrunner, the maximum torque is generated when the ratio between the stator area to the rotor area is 2:1. The outrunner can theoretically produce higher torque but is reduced to the low air gap field in case of magnetic saturation.

Secondly, an inrunner usually contains fewer poles than slots (Sensinger et al., 2011). In an outrunner, the number of poles is usually higher than the number of slots. This is because there is more space for slots in an inrunner compared to an outrunner. This increased space for the slots results in a higher number of windings around the yokes, therefore, higher torque output is achieved. The higher number of poles than coils in the outrunner results in higher torque.

Third, an outrunner has a lower RPM per one volt applied (Ryan, 2018). The large diameter of the outrunner's rotor creates a larger circumference for the actuator to travel in one rotation. A lower RPM per volt results in a higher torque as these motor constants are inversely proportional to each other. The simulations by Sensinger et al. (2011) indicated a decrease of 76-90% in velocity ratio values due to higher rotor inertia in outrunner actuators. In addition, their simulations comparing the outrunner with the inrunner showed that the outrunner had a 13-40% decrease in rated power proportional to their lower slot volume.

Fourth, in the case of an inrunner, the shafts rotate in this actuator, while in the case of outrunner, the outer ring of the outrunner rotates. This difference in configuration has several advantages and disadvantages depending on their application. For example, in the VIP, the outrunner can be enclosed within the impeller and directly connects to the rotating part of the motor, while the inner parts stay stationary.

Finally, the inrunner has a higher potential to provide better efficiency (Ryan, 2018). The coils of the actuator produce the most heat in an actuator. This heat needs to dissipate through the various actuator components to the surrounding air. In an inrunner, the coils are just under the outer housing and can dissipate the heat through the surface area of the stator housing. In the case of the outrunner, the coils are in the middle, and the heat travels through more components. Therefore, the inrunner can get rid of the generated heat more

efficiently, allowing the motor to run at a lower temperature and provide better efficiency. To conclude, the outrunner has the potential to deliver a higher torque. However, the lower efficiency needs to be considered and thereby the higher temperature increase in the actuator.

3.4 PMSM

The inrunner and outrunner are explained above based on a BLDC. However, the actuator from Pang et al. (2020) is a PMSM, therefore, the difference is explained in the next section. The PMSM design is similar to a BLDC motor, as the PMSM consists of the same primary components. However, the BLDC and PMSM differ in the layout of the windings, stator flux linkage and the shape of the back electromotive force (EMF) (figure 25). A difference in the layout of the windings and the input current causes the differences in back EMF. In a BLDC motor, the windings are concentrated, and the current input is given as a direct current (DC). Windings are concentrated around an individual pole; thereby, the windings per phase are isolated from each other as depicted in Figure 26. With distributed windings, the windings of each phase overlap with other windings. Therefore, the BLDC is driven by a current rectangular pulse, resulting in a trapezoidal back EMF. On the other hand, the layout of the winding in a PMSM is distributed, and the driving current is alternating current (AC); this results in a sinusoidal current and a sinusoidal back EMF (Figure 25) (Hanselman, 2003). The wire travels from one slot across three teeth in a three-phase motor to the next slot in a distributed manner. The winding thereby encloses the teeth and forms the pole for that coil.

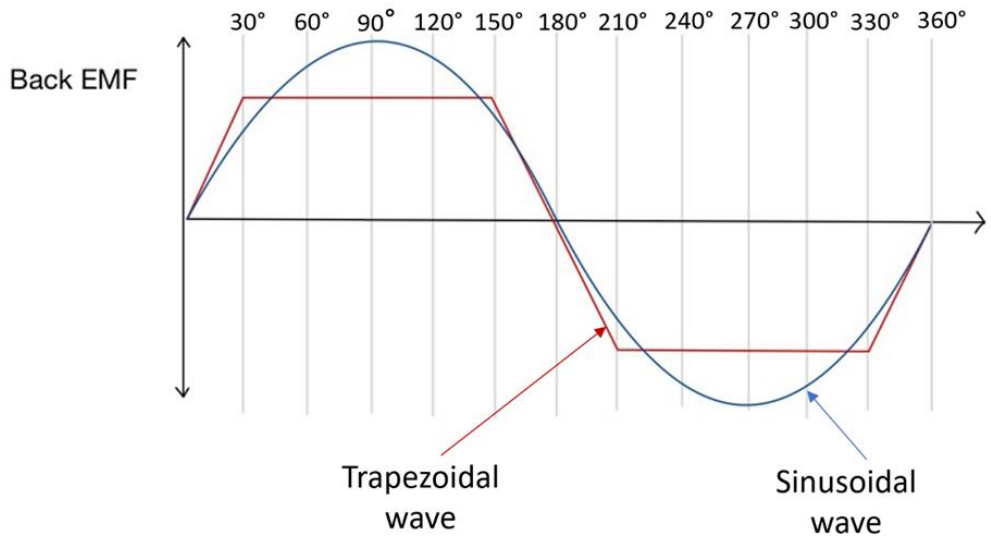

Figure 25: The back EMF over a full 360 degrees cycle for the BLDC (in red) and the PMSM (in blue) for one phase.

More accurate feedback of the rotor's position is required (Derammelaere, Haemers, De Viaene, Verbelen, & Stockman, 2016). The exact rotor position feedback is needed to identify the right time to alternate the direction of the current input. Therefore, PMSMs require position feedback throughout the whole electrical period and at the six communications points. Continuous computation is also required to obtain the sinusoidal waveform, measured by one Hall effect sensor and a PMSM motor controller. The sensor continuously monitors the rotor position, and the information is passed onto the PMSM motor controller. Due to the constant monitoring, the torque ripple is diminished in the PMSM, making the PMSM more efficient than the BLDC motors. However, the control of the PMSM motor is more complicated.

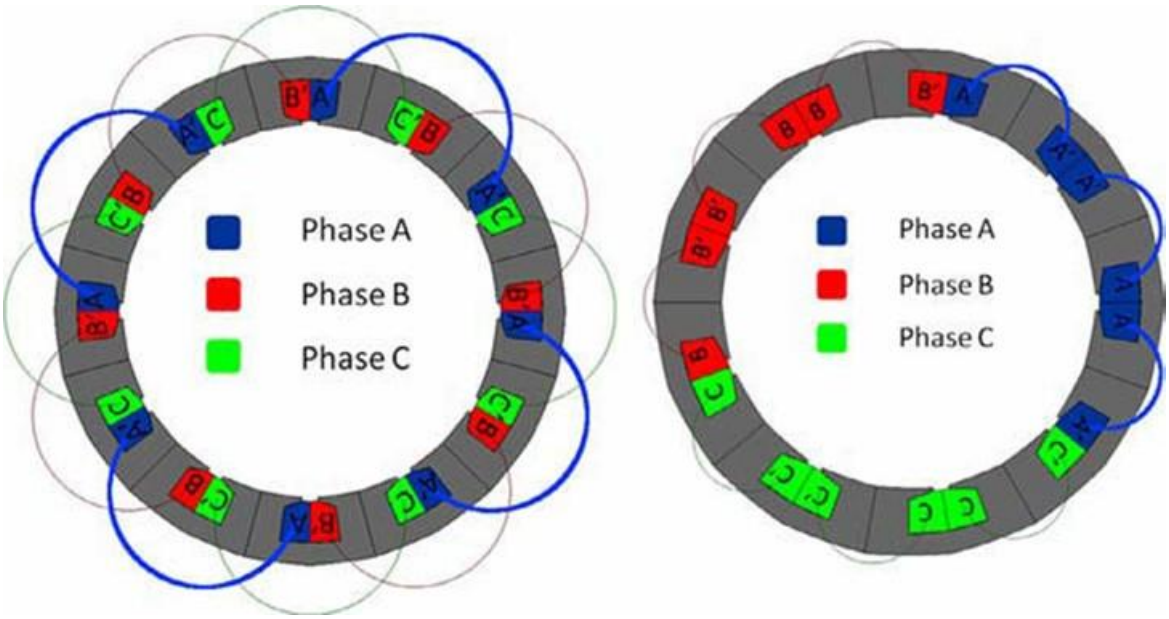

Figure 26: Distributed windings on the right and concentrated windings on the left. Both are three-phase motors. Image courtesy (Tang, Masmoudi, Paulides, Kazmin, & Lomonova, 2011).

3.5 Other electric motor parameters

Besides the differences between an inrunner or an outrunner and a PMSM or BLDC, the number of phases and number of poles and yokes need to be determined when designing an actuator.

Most of the BLDC motors are powered by a three-phase power supply. The advantage of a three-phase motor is that steady power is delivered because the power never drops to zero, as with a one-phase motor (Figure 27). The number of phases influences the number of yokes because the number of yokes is a multiple of the number of phases (Hanselman, 2003). As can be seen in Figure 28, there are three phases A, B, and C and the windings in each phase connected to each other. The current flows in series through each phase and thereby moves the magnetic field around in the air gap. During every step, one phase is negatively charged, one positive, and the last one is turned off.

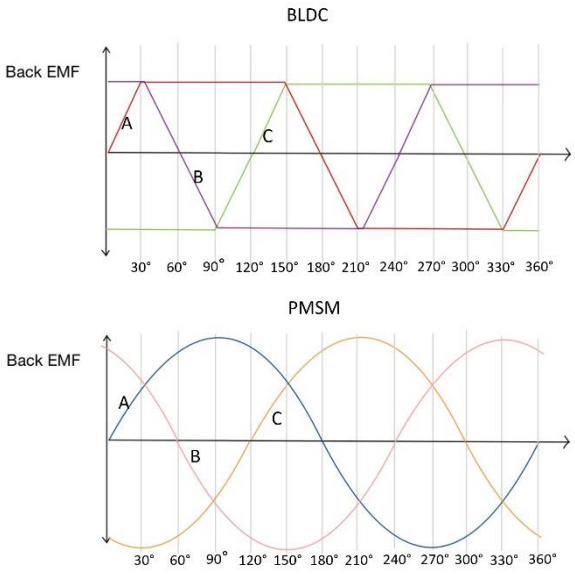

Figure 27: Back EMF for a three-phase BLDC and PMSM actuator. The different colored lines indicate the different phases which are 120 degrees apart.

Number of poles and yokes

The number of poles and yokes differ among various electric motor designs. The number of poles is always even; otherwise, the number of north and south poles on the rotor are not evenly distributed. Besides the number of yokes being a multiple of the number of phases. There is no defined ratio between the number of poles and yokes; although, some relationship exists between the number of yokes and poles.

The maximum electromagnetic force is experienced when the yoke aligns with the magnetic field (Mekid, 2010). Therefore, spreading out the yokes over many poles increases the overall torque of the actuator. However, a higher number of poles per yoke does have the disadvantage of a less smooth actuator rotation

due to induction of the cogging torque (Hanselman, 2003). The cogging torque is the interaction between the permanent magnets acting on the stator yoke and is independent of any current. Each time a pole passes by a stator slot, the permanent magnet produces a cogging torque, which is disadvantageous in BLDC motors. Because the cogging torque, causes vibration and noise, thereby reducing the accuracy of the control and the performance of the actuator (Chen, Shu, & Chen, 2012). An option to reduce the cogging torque is by decreasing the size of the slot opening, the distance between the two yokes (Figure 22). However, the length of the slot opening should be two to three times the covered diameter of the wire placed in the slots (Figure 21). There are two disadvantages of a narrow slot; the slot leakage inductance component of the winding is increased, and the wrapping of the copper coils around the stator becomes harder. To conclude, there should be a balance between the number of yokes and poles and having a smooth rotational motion.

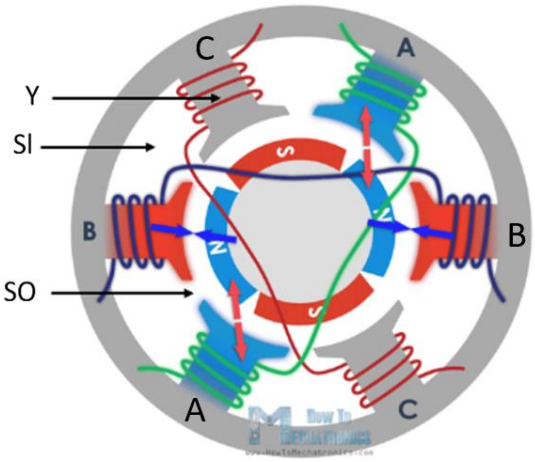

Figure 28: BLDC motor with six coils and four poles. Three-phase system powers the BDLC. The blue arrows indicate the attracting forces and the red arrows the repelling forces. Image courtesy (Nedelkovski, 2020) SO, Slot opening

3.6 Efficiency (and Losses)

In the torque calculation (Eq. 3.2), the losses in the actuator were neglected. In an electric motor, the supplied electrical power is converted to mechanical power. Several losses accompany this conversion, including; copper losses, core losses, mechanical losses, power interruption losses, and stray losses (Andrada, Torrent, Perat, & Blanqué, 2004; Boukais & Zeroug, 2004) (Figure 29). In commercial inrunner actuators with a diameter between 4 and 6 mm, these losses decrease the performance resulting in efficiency between 39% and 69% (FaulHaber, 2020; "Maxon EC motors ", 2020). Unfortunately, in this size range, no information could be found about the efficiency of outrunner actuators.

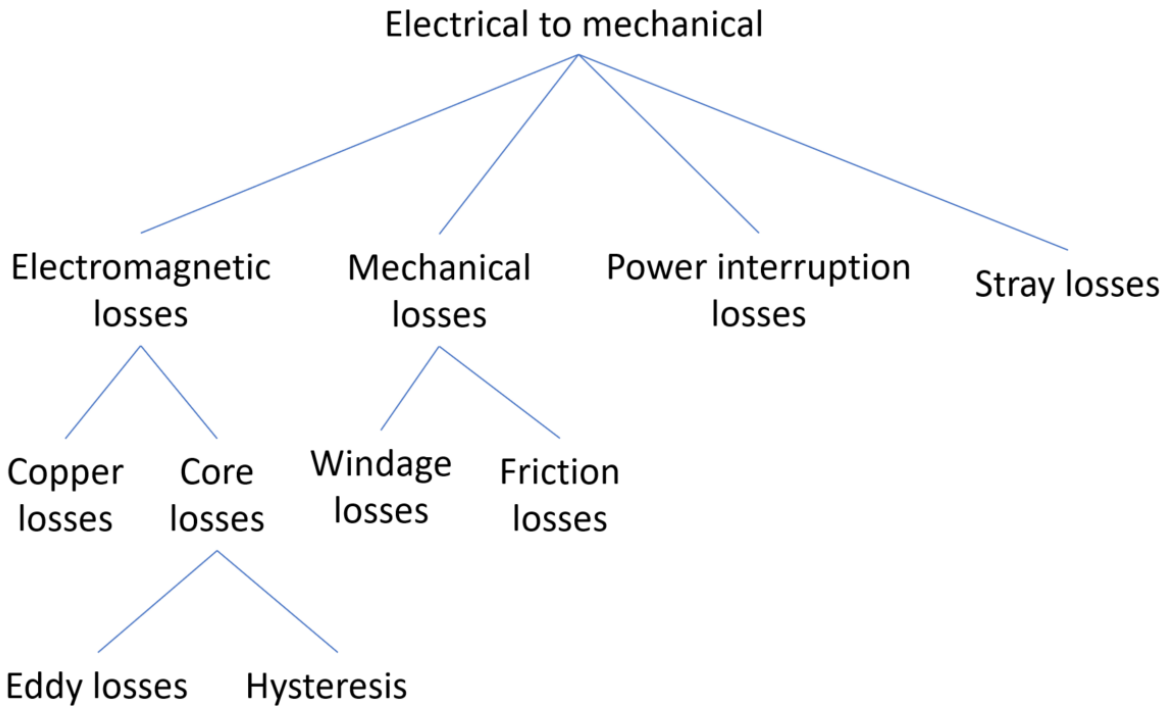

Figure 29: Overview of the power losses in an electromagnetic actuator.

The copper losses and core losses are the electromagnetic losses, which account for 80% of the total losses in an actuator (Kuria & Hwang, 2011). The copper losses are the losses due to the resistance in the windings. This resistance causes an electrical power conversion to heat. Copper losses can be calculated by

$$P_{lw} = {i_{in}}^2 * R_{wire} \quad (3.17)$$

- P_{lw} electric power losses due to wire resistivity [Watts]
- i_{in} input current [A]
- R_{wire} resistance in the wire [Ω]

The resistance in the cable can be calculated with the following equation:

$$R_{wire} = \frac{\rho_{wire} * l_{wire}}{A_{wire}} \quad (3.18)$$

- R_{wire} the resistance of a wire in Ω
- ρ_{wire} the resistivity in Ωm
- l_{wire} the length of the wire in m
- A_{wire} the cross-sectional area of the wire in m^2

3.6.1 Temperature calculation for the VIP

The temperature rise in an inrunner caused by the power losses in the wire can be calculated with the following equation:

$$\Delta T_{inrunner} = {i_w}^2 * R_{mw} * (R_{thwin} + R_{thcase}) \quad (3.19)$$

- $\Delta T_{inrunner}$ change in temperature for an inrunner in K
- i_w current through the motor windings in A
- R_{mw} resistance in motor winding in Ω
- R_{thwin} thermal resistance from windings to the case in K/W
- R_{thcase} thermal resistance case to ambient in K/W

It is assumed in Eq 3.19 that the heat from the coils is directly transferred to the stator core. The heat dissipation is found to be poor for an outrunner actuator, and the resulting temperature is higher. This is due to the heat generated from the windings that need to travel through more components before the heat exists in the motor. These additions result in the following equation.

$$\Delta T_{outrunner} = {i_w}^2 * R_{mw} * (R_{th1} + R_{th2} + R_{th3} + R_{th4} + R_{thout}) \quad (3.20)$$

- $\Delta T_{outrunner}$ change in temperature for an outrunner in K
- R_{th1} thermal resistance through the stator core in K/W
- R_{th2} thermal resistance through the air gap in K/W
- R_{th3} thermal resistance through the magnet in K/W
- R_{th4} thermal resistance through the case in K/W
- R_{thout} thermal resistance out into the ambient in K/W

As discussed above, the redesigned configuration of the VIP by Rodefeld et al. 2019, an internal secondary flow path was created to allow the blood to pass between the actuator and the impeller. In the case of VIP thus, as reported by the Rodefeld et al. (2019), the ambient media cooling the actuator is the blood flowing along the electromotor through the secondary pathway. It is assumed the same cooling mechanism can be applied in the modified VIP design for minimally-invasive implantation. The heat transfer from the wire windings to the surrounding blood flowing around the actuator's rotor can be calculated with the following equation (Figure 30).

$$\Delta T_{VIPacuator} = {i_w}^2 * R_{mw} * (R_{th1} + R_{th2} + R_{th3} + R_{th4} + R_{thout}) \quad (3.21)$$

- $\Delta T_{acuator}$ change in temperature for the actuator in K
- R_{thout} thermal resistance out into the blood in K/W

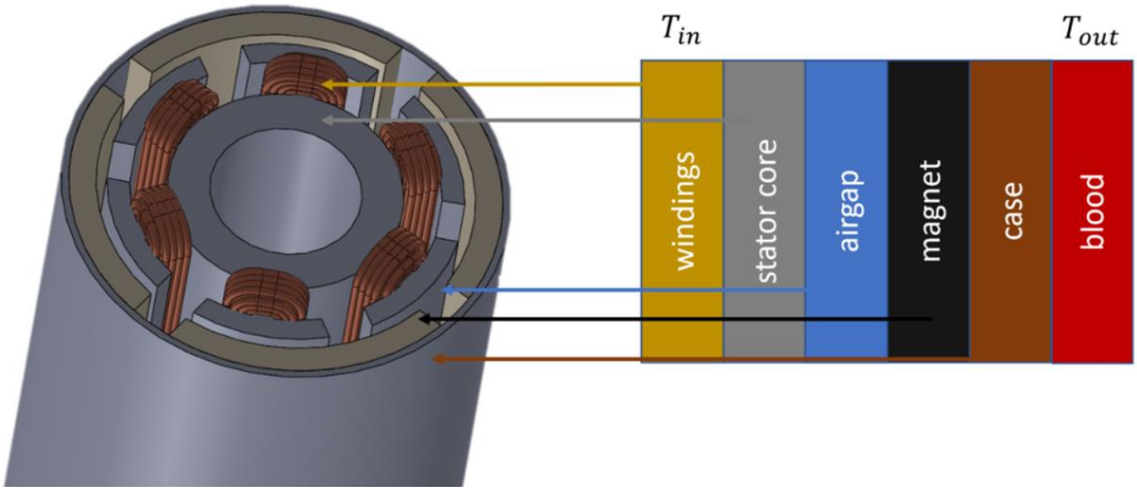

Figure 30: A sketch of an outrunner electric motor with the different components through which the temperature exists.

The thermal resistance in the previous equations (Eq 3.19-3.21) can be calculated with the following equation (Cengel, 2003):

$$R_{th} = \frac{L}{kA} \quad (3.22)$$

- R_{th} thermal resistance in K/W
- L_{plane} plane thickness in m
- k thermal conductivity of the material in W/mK
- A_{plane} plane area in m^2

Thermal conductivity for the external environment is calculated using the heat transfer coefficient, which gives the following equation (Cengel, 2003):

$$R_{th} = \frac{1}{h_{heat}A} \quad (3.23)$$

- R_{th} thermal resistance in K/W
- h_{heat} heat transfer coefficient of the material in W/m^2K

The blood's heat transfer coefficient depends on the velocity of the blood flowing through the vessels (Consiglieri, dos Santos, & Haemmerich, 2003). The blood velocity can be calculated from the volumetric flow with the following equation:

$$v = \frac{Q_{Lmin}}{A_{vessel}} (3.24)$$

- v velocity in m/s
- Q_{Lmin} volumetric flow in m^3/s
- A_{vessel} surface area through which the flow flows in m^2

3.6.2 Mechanical losses

The mechanical losses are composed of friction losses and windage losses (Andrada et al., 2004). Windage losses are the resistive force caused by the interaction between the ambient media and the rotating rotor. The friction losses occur at the shaft around which the rotor moves. The mechanical losses can be calculated with the following equation:

$$P_{mechloss} = P_{wind} + P_{fr} \approx 2R_{ro}^3 L_{str} \omega_{(RPM)}{}^3 \times 10^{-6} + \frac{3}{2} n_r m_{rot} \omega_{(RPM)} 10^{-3} (3.25)$$

- $P_{mechloss}$ mechanical power losses [Watts]
- P_{wind} power loss due to the windage losses [Watts]
- P_{fr} friction losses [Watts]

- n_r number of bearings
- m_{rot} weight of the rotor [kg]

3.6.3 Other power losses in the electric motor

Core losses of a soft ferromagnet material result from eddy current losses and hysteresis (Nag, Santra, Chatterjee, Chatterjee, & Ganguli, 2016). These losses occur in the stator teeth, stator yoke, and stator core (Stumberger, Hamler, & Hribernik, 2000). Eddy currents are circulating currents caused by the changing magnetic field, which do not contribute to the power (Hanselman, 2003). Eddy losses are different for BLDC and PMSM motors because they are caused by the magnetic flux, sinusoidal for PMSM and have a trapezoidal shape in BLDC motors (Andrada et al., 2004).

Hysteresis losses are due to the reversal of magnetization of the stator armature core (Nag et al., 2016). The stator core undergoes one complete cycle of magnetic reversal after passing under one pair of poles. The hysteresis only depends on the peak value of the flux density; therefore, the equation is the same for both the BLDC and the PMSM.

Stray losses are the losses that arise from the non-uniform distribution of a current in copper (Andrada et al., 2004). The stray losses also encompass the additional core losses produced by the distortion of magnetic flux by the load current. The stray losses are difficult to determine accurately; therefore, it is assumed that the stray losses are equal to about 1% of the output power (Gieras, 2002). Unfortunately, the above losses cannot be calculated without knowledge of the exact flux in the actuator, which is not present in the current thesis.

3.6.4 Hydraulic efficiency (and Losses)

The above losses are the losses in the electric motor. The actuator's output is mechanical power which is transferred to the hydraulic power of the VIP. The hydraulic power is responsible for propelling the blood forward. In the conversion of mechanical power to hydraulic power, power losses occur due to the resistance from the blood, slippage on the VIP's surface, and the pressure head. The resistance from the blood imposed on the VIP rotation is due to the viscosity of the blood and the friction forces between the impeller surface and the blood cells. The Von Kármán principle of the viscous pump is based on the no-slip condition, which requires the fluid at the disk's surface to rotate at the same velocity as the disk (Rodefeld et al., 2010). The viscosity of the blood diffuses this rotation away from the disk and induces rotation in the surrounding fluid. Despite the no-slip condition, there will always be power losses due to not all fluid particles being in contact with the VIP and needing to be propelled through other particles. In the TCPC, the VIP must work against a pressure head; although being relatively low, this pressure head still causes some power losses.

All the above losses cause the hydraulic power output to be lower than the electrical power input to the VIP. The efficiency of the actuator can be calculated with the given value of mechanical power. The mechanical power is usually determined by measuring the values with mockup experiments; this is not possible in the given case study. However, available efficiency equations and values from other devices such as the VIP could be used to estimate the efficiency range of the VIP.

The hydraulic efficiency, which is the total conversion of the electrical power the hydraulic power, can be given as (Halliday, Resnick, & Walker, 2013):

$$\eta_h = \frac{P_h}{P_{el}} * 100\% = \frac{Q * \Delta p * \frac{133.32}{60{,}000}}{i_{in} * V} * 100\% \quad (3.26)$$

- η_h hydraulic efficiency
- P_h hydraulic power [Watts]
- P_{el} electrical power [Watts]
- Q_{Lmin} flow in L/min
- Δp measured pressure rise across the pump in mmHg
- $\frac{133.32}{60{,}000}$ scaling factor for conversion to SI units
- i_{in} current input of the motor [A]

- V_{in} voltage input of the motor [V]

The hydraulic torque can be calculated from the hydraulic power (Halliday et al., 2013):

$$P_h = \tau\omega_{(\mathrm{SI})} \rightarrow \tau = \frac{P_h}{\omega_{(\mathrm{SI})}} (3.27)$$

- P_h hydraulic power [Watts]
- τ torque in [Nm]
- $\omega_{(\mathrm{SI})}$ angular velocity [rad/sec]

The mechanical power (Smith et al., 2019), which is the power the actuator delivers, can be calculated with the following equation:

$$P_m(t) = i_m(t) * \omega * K_\tau * \frac{2 * \pi}{60} (3.28)$$

- $P_m(t)$ = mechanical power [Watts]
- i_m = electrical current drawn by the motor [A]
- ω = the rotational velocity of the motor [RPM]
- K_τ= torque constant [Nm/A]
- $\frac{2*\pi}{60}$ is the scaling factor for conversion to SI-units

The motor's torque constant needs to be known for the above equation, which is usually determined by measuring the torque output at a certain current input.

4. Requirements for the actuator

In this chapter, the requirements for the actuator are provided. The requirements are either defined quantitatively based upon the theory in chapters 2 and 3 or defined qualitatively through calculations. First, the dimensional requirements for the actuator are provided along with the calculated hydraulic power, torque, and efficiency, and then the chapter is concluded with the list of requirements.

4.1 Outer dimensions of the actuator

The outer dimensions for the actuator are based on the VIP and the dimensional restrictions of the patient-specific TCPC geometry. The VIP is intended for chronic use in full-grown patients with Fontan circulation. The intention is to modify the design of the VIP allowing its minimally invasive implantation through a sufficiently large vein, for example, the jugular vein in the neck. Access through the right jugular vein allows a straight path to the TCPC intersection. Hence, the device does not need to be flexible, allowing the actuator to be rigid and offering some flexibility in its length. In full-grown patients, the right internal jugular vein is sufficiently large and can accommodate a large-calibre vascular access sheath with a diameter of up to 6 mm (Coburn & Merschen, 2010). Excluding the thickness of the delivery sheath, VIP, and considering the biconical shape of the fully deployed VIP, the outer dimensions of the outrunner electromotor were set to a diameter of 5.4 mm.

In the majority full-grown Fontan patients, the vertical and horizontal dimensions of the TCPC intersection fall within 20 mm, which determines the maximal size of the fully expanded VIP. Given the biconical shape of the VIP, the length of the actuator fitted inside the impeller is set to 11 mm.

4.2 Hydraulic torque and hydraulic power

Figure 19 shows a sketch of the actuator in the VIP inside the TCPC. The following calculations are performed to calculate the required hydraulic power and torque the VIP needs to produce. First, the hydraulic power of the pump is calculated with Eq. 3.26. The hydraulic power is then used to calculate the torque with Eq. 3.27.

The values used to calculate the power and torque were taken from the publications by the research group of Rodefeld.

- $p_{TCPC} = 0\ to\ 2000\ Pa$, based on Kennington et al. (2011), stating that a pressure rise of 15 mmHg is desired.
- $\omega_{(\mathrm{SI})} = 523.6\ rad/sec$, based on Kerlo et al. (2013), who performed most of their experiments at an operating velocity of 5000 rounds per minute (RPM). For the calculations, rad/sec is needed but for the rest of the paper RPM will be used to define rotational velocity because it is generically used.
- $Q = 7.33\ \times 10^{-5}\ m^3/s$, based on the volumetric flow rate of 4.4 L/min used by Kerlo et al. (2013).
- SG = 1.0506 was taken from the research by Trudnowski and Rico (1974) because the blood's relative density was not included in the publications by Rodefeld.

Using the equations 3.26 and 3.27, the power (P_h) and the torque (τ) values were calculated to be 0.147 Watts and 280 µNm.

4.3 Efficiency

As mentioned before, the accurate estimation of the mechanical power generated by an actuator is obtained through measurements which is not possible in the given case. Also, not all power losses can be calculated at this stage. These two reasons precludes precise calculation of the motor's efficiency. Consequently, the efficiency is an educated estimation based on the available data for the different cardiac assist devices, such as the IntraVAD by Wang et al. (2017), the Aortix intra-aortic pump by Vora et al. (2019), and the cavopulmonary pump by Granegger et al. (2019).

4.3.1 IntraVAD

The IntraVAD accelerates the blood flow in one direction, parallel to the VIP's axis, in contrast to the VIP which accelerates the blood into the direction perpendicular to its axis. Unfortunately, Wang et al. (2017) did not report the efficiency of the IntraVAD in the research article. Still, the efficiency can be calculated using

the measured motor torque and the calculated hydrodynamic torque, (Wang et al., 2017), although, less accurately due to lacking data on rotation velocity.

The hydrodynamic torque and the maximum motor torque are 1.23 and 7.69 mNm respectively provided in the article by Wang et al. (2017). These values result in an efficiency of 16%. In a later study done by the same group, the efficiency was assumed to be 10% in the case of a less efficient system (Wang et al., 2020). The whole system's efficiency is found to be low, primarily due to the power losses from converting the mechanical power to hydraulic power. Not all the blood encounters the surface of the vanes, and therefore, the hydraulic power must travel through the blood to increase the flow.

4.3.2 Aortix intra-aortic pump

The efficiency of the Aortix intra-aortic pump was not provided in the study of Kapur et al. (2020). However, they did provide the parameters with which the mechanical to hydraulic efficiency could be calculated using the related equations given in the previous chapter (Eq. 3.26 and Eq. 3.28).

The variables for the calculation of the efficiency are taken from the article by Vora et al. (2019) and the datasheet of the Maxon motor ("Maxon EC motors ", 2020):

- Q_{Lmin} = 5 L/min
- Δp = 15 mmHg
- $\omega_{(RPM)}$ = 30,000 RPM
- I_{in} = 0.109 A, assumed is that the motor runs at the nominal current, which is the max continuous current.
- K_{τ} = 0.00298 Nm/A

These variables provided the result in a hydraulic power of 0.166 Watt and a mechanical power of 1.02 Watt, resulting in an efficiency of 16.33%. Thus, the hydraulic power of the Aortix is close to the hydraulic power of the VIP, as calculated above.

4.3.3 Cavopulmonary pump

The third pump used to make an estimation is the cavopulmonary pump by Granegger et al. (2019). In the main operating conditions (rotational speed 2500 RPM), the flow rate of this device was 4L/min, and the pressure difference is 11.3 mmHg, which results in a hydraulic power of 0.1004 Watt. The article reports the hydraulic efficiency of the cavopulmonary pump to be 40%, which was calculated by using a computation fluid dynamic simulation.

4.3.4 Tesla pump

Moody (2016) evaluated the efficiency of the Telsa pump, which was also applied as a Fontan circulatory assist device by Cysyk et al. (2019). The pump's efficiency was only measured until an impeller speed of a little under 1200 RPM. Moody (2016) measured the in vitro pump efficiency at various outlet resistances. At the vascular resistance of 715.4 dynes/seconds/m^{-5}, which corresponds to a typical but low systemic vascular resistance in the adult, at the rotational speed of 1187 RPM the Tesla pump's efficiency was 5.57%. Figure 31 shows the extrapolated trend of the relationship between the Tesla pump's rotational speed and its efficiency up to 5000 RPM to estimate the efficiency of the VIP. At 5000 RPM and the same outlet resistance, multidisc Tesla pump is predicted to have an efficiency of 28%. Extrapolating the trendline does induce uncertainty because the data is not tested, and it's assumed that the data follows the same linear relationship when increasing the impeller speed.

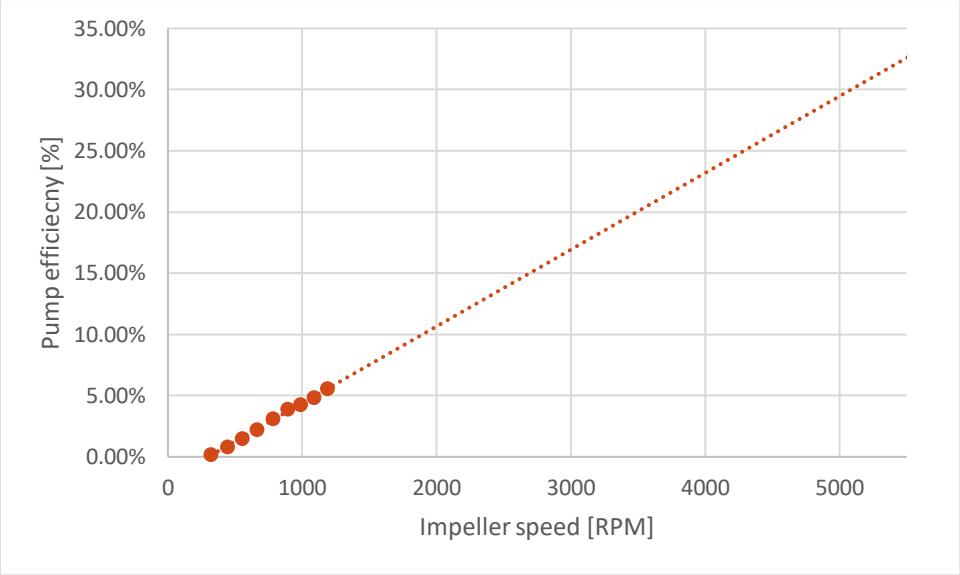

Figure 31: Data of Moody (2016) plotted with a trendline that is extrapolated to 5000 RPM.

The IntraVAD and the Aortix intra-aortic impeller pump are small axial pumps that propel forward part of the blood while being placed within the bloodstream. Both impellers have an efficiency of about 16%. The Tesla pump by Cysyk et al. (2019) and the cavopulmonary pump by Granegger et al. (2019) are larger centrifugal pumps replacing completely the TCPC intersection and both have a higher efficiency of respectively 40% and 28%. Because of the drawbacks of the latter pumps and avoiding the overestimation, the VIP's efficiency is assumed to be 16% in the given study. Thus, the mechanical power is 0.92 Watt instead of 0.15 Watt and the motor torque of 1767 µNm instead of 283 µNm.

4.4 List of requirements

Combing the main functional parameters calculated in this chapter with some additional important requirements concludes in the following list of requirements for the actuator:

1. The maximum outer dimensions of the actuator should be 5.4 mm in diameter and a length of 11 mm.
2. The actuator needs to be rotary and must provide a continuous movement of 360 degrees of rotation.
3. The actuator's rotating part should preferably be outside to easily connect to the VIP, such as in an outrunner configuration.
4. The required output of the actuator is a torque of 1767 µNm and a power of 0.92 watts.
5. The internal temperature of the actuator cannot exceed 155°C; otherwise, the isolation separating the windings will melt and thereby causing a short circuit. (Conrad, 2021).
6. The actuator should not increase the blood temperature above 40°C; otherwise, the risks of plasma protein denaturation can occur, which is the breakdown of blood cells (Vazquez & Larson, 2013).
7. The actuator needs to be sealed off to ensure no contact with the blood. Also, the air from the air gap should not leak into the bloodstream.
8. The actuator will be manufactured as a prototype with as many off-the-shelve components as possible. If no other options are available, then custom-made parts can be included.
9. The actuator should be controlled by a commercially available well-trusted motor driver that provides reliable control.
10. The actuator should have a lifetime of three years without the need for servicing (estimation is based on the lifetime of the heartmate III, (Abbot, 2020))
11. The actuator is preferably able to be powered by a battery of about 3 Volts.

5. Basic design

As mentioned in chapter 3, the actuator by Pang et al. (2020) is used as starting point. In the following chapter, the actuator is adapted to an outrunner configuration with the desired outer dimensions. Validation of the torque and temperature requirements are also calculated.

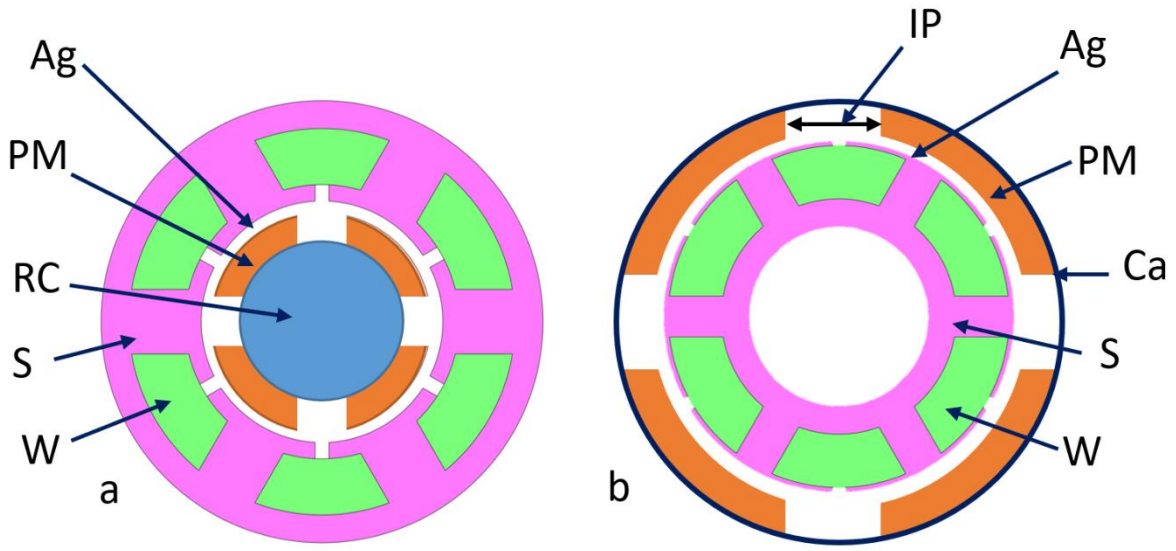

Figure 32: a) depicts a schematic representation of the actuator design by Pang et al. (2020) used as starting point for the design of the actuator. b) is the converted outrunner version based on the actuator by Pang, Shi, Xie, Huang, and Bui (2020). Ca, Case; IP, Interpole length; PM, permanent magnets; RC, Rotor core; W, windings

The scaled-down inrunner version of the actuator is made by reducing the dimensions of the actuator given in de study of Pang et al. (2020) by 2.78 (Figure 32a and Table 3). This scaling factor is calculated from the required outer diameter of the actuator and the outer diameter of the actuator provided by Pang et al. (2020). The axial length was increased from 5 mm to 11 mm. From this design, an outrunner version is designed by translating the sizes of the stator into an outrunner configuration (Figure 32b). After that, an air gap of 0.14 mm width is included, and a 0.1mm thick case around the actuator is added as a holder for the permanent magnets. Between the added case and the air gap, four curved permanent magnets were fitted with a thickness of 0.36 mm. The magnet thickness and the air gap length are based on the scaled-down design of the actuator given by Pang et al. (2020). The core back width is based on the remaining space in the center of the stator, keeping a shaft opening of 1.5 mm in diameter. The slot opening was arbitrarily chosen. The interpole length was also scaled-down with the same ratio as the rest of the actuator.

The copper windings in the actuator given in the study by Pang et al. (2020) have a diameter of 0.162 mm. The following equation is used to calculate the number of windings (N) for the scaled-down outrunner actuator:

$$A_{win} = \frac{\pi * {D_{wir}}^2}{4} * N \quad (5.1)$$

- A_{win} the surface area taken by windings
- D_{wir} diameter of the copper wires in m

Eq. 5.1 gives the surface area for the windings to be $7.6mm^2$ for the actuator provided in the research of Pang et al. (2020). The surface area for the concept actuator was estimated by first calculating the space for the stator as given by Pang et al. (2020) actuator and the concept actuator. From these two surface areas, the scaling factor was taken. After that, the scaling factor was used to estimate the surface area for the wire in the concept actuator. This resulted in 24 turns for the windings per yoke.

The resulted actuator's concept was then adjusted to arrive at a more realistic actuator design in terms of optimal performance and manufacturability. Thus, changes were made to the stator: the thickness of the

base and top of the T-shaped yoke was increased from 0.1 mm to 0.3 mm, deemed to be enough to withstand the interaction forces. The stator yoke is 11 mm in height, which is assumed to be a good basis to support the think yoke. Altogether, this resulted in a modeled outrunner electromotor with the outer dimensions of 5.4 mm in diameter and 11 mm in length (Figure 33).

Table 3: Parameters for the new proposed actuator design and the motors reported by Pang, Shi, Xie, Huang, and Bui (2020), and the scaled-down version of the actuator by Pang et al. (2020). The Yoke base width is the thickness of the base of the yoke. The core back width is the thickness of the circle the stator yokes are connected to. The slot opening is the distance between two tops of the yokes.

	All dimensions are in mm	**Symbols**	**Pang et al. (2020)**	**Inrunner Scaled-down version of the motor by Pang et al. (2020)**	**Outrunner Scaled-down version of the motor by Pang et al. (2020)**	**Concept version**
General	Inrunner or outrunner?	-	Inrunner	Inrunner	Outrunner	Outrunner
	Number of phases	-	3	3	3	3
	Type of connection	-	Star	Star	Star	Star
	Air gap length	δ	0.4	0.14	0.14	0.14
	Axial stack height	L_{st}	5	11	11	11
	The outer diameter of the actuator	D_{ao}	15	5.4	5.4	5.4
Stator	Outer radius in mm	S_{ro}	7.5	2.7	2.15	2.1
	Inner radius in mm	S_{ri}	4.1	2.95	2.2	1.5
	Number of slots	N_s	6	6	6	6
	Yoke base thickness	YBt	2.2	0.79	0.5	0.3
	Slot opening	SO	0.47	0.17	0.17	0.6
	Core back width	CB	0.95	0.34	0.34	0.45
Rotor	Outer radius in mm	R_{ro}	7.4	2.66	5.4	5.2
	Inner radius in mm	R_{ri}	2	0.72	5.3	4.48
	Number of poles	N_m	4	4	4	4
	Interpole iron width	IP	1.6	0.58	0.58	0.58
	Magnet thickness	h_m	1	0.36	0.36	0.36
Windings	Number of windings	N	60	22	22	24
	Diameter of the wire	D_{wir}	0.162	0.135	0.135	0.1

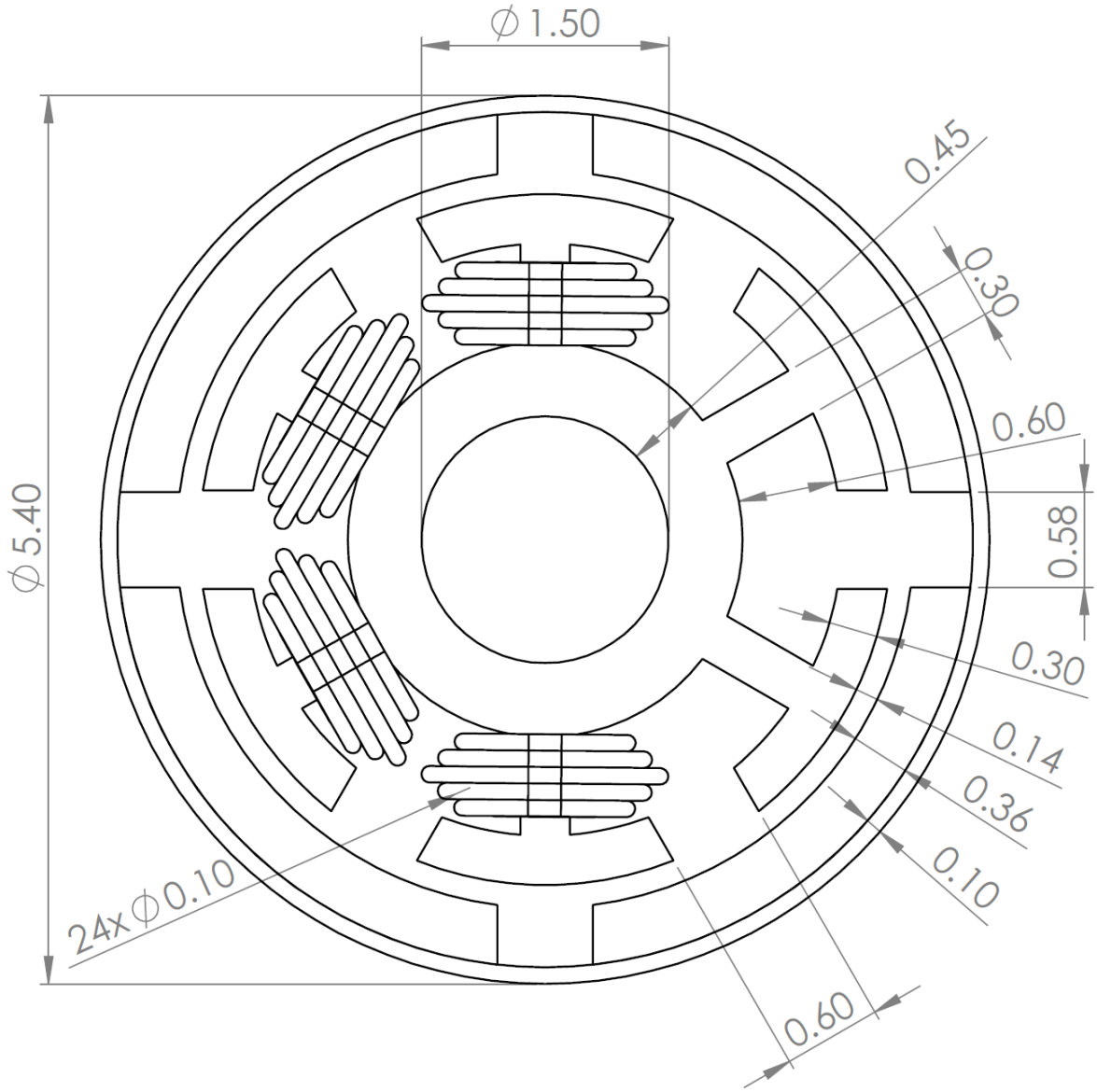

Figure 33: Top view of the concept design of the actuator. Only four of the six yokes are wrapped with the windings to allow for clear dimensions of the yokes.

5.1 Relevant calculations of the design

The theoretical torque and the actuator's internal temperature of the concept design are calculated to evaluate the feasibility. The losses are not included in this chapter to first compare the theoretical torque with the set requirements. These two parameters are calculated because they are the most important requirements to meet.

5.1.1 Torque calculation

The dimensions of the actuator's concept design given in Table 4 are taken from Figure 33. The current is scaled-down to 0.3A from the reported current used by Pang et al. (2020). The other parameters are the same as for the validation of the torque equation from chapter 3.1. Filling these into Eq. 3.13 results in 1715.4 µNm of torque, close to the estimated required torque of 1767 µNm for the actuator to drive the VIP.

Table 4: Input variables for the torque equation of the combined version of the actuator and the results.

	Symbols	Concept actuator
Current in A	i	0.3
Number of windings	N	24
Stack height in mm	L_{st}	11
Outer diameter of the rotor in mm	R_{od}	5.2
Inner diameter of the rotor in mm	R_{id}	4.48
Thickness of the magnet in mm	h_m	0.36
Air permeability in $\frac{N}{A^2}$	μ_0	1.257×10^{-6}
Air gap length in mm	δ	0.14
Residual flux density	B_r	1.3
Relative permeability of the magnet in $\frac{N}{A^2}$	μ_r	1.05
Torque in µNm	$\tau_{calculated}$	1628.7
Torque in µNm considering the correction factor	τ_{corr}	1715.4

5.1.2 Temperature calculation

As mentioned, the most dominant source of heat in the actuator is the resistance power in the wire around the stator yokes. As one of the requirements state, the temperature of the windings cannot exceed 155°C. To calculate the internal temperature with Eq. 3.21 the surrounding temperature needs to be known. Therefore, the temperature experiments by Granegger et al. (2019) are discussed next.

Granegger et al. (2019) investigated the temperature rise of the blood surrounding their cavopulmonary pump. The increase of the blood temperature was determined with computational fluid dynamic simulations using the power losses of the actuators as input. A worst-case scenario simulation with maximum velocity and maximum flow resulted in a blood temperature of the surrounding environment of 38.4°C. Thus, Granegger et al. (2019) concluded that the maximum computed temperature increase due to the motor was a heat of 1.4°C. The drawback of this approach was that Granegger et al. (2019) assumed steady boundary conditions. The approach to simulate heat transfer assumes a linear relationship between the heat flux and the temperature difference of the media, which they did not validate.

Rodefeld et al. (2019) concluded that the implied electric motor did not increase the temperature of the surrounding blood. Therefore, the actuator's external environment is a constant temperature of 37 °C, which is the temperature of the blood in the vena cava (Britt, 2012). When the VIP's environment remains constant, the actuator's internal temperature can be derived by calculating the change in temperature through the actuator, Eq. 3.23. Therefore based on Rodefeld et al. (2019) and Granegger et al. (2019) is concluded that the surrounding temperature of 37 °C can be taken for the temperature calculations.

Table 5 shows all the values required to calculate the thermal resistance for different components of the actuator. To select the right heat blood transfer from the literature, first the velocity of the blood needs to be known. The velocity can be calculated with Eq. 3.24. For the diameter of the TCPC, the diameter of the vena can be taken, which is about 20 mm (Prince, Novelline, Athanasoulis, & Simon, 1983). With the given radius, the surface area of the TCPC can be calculated, which results in $3.14 \times 10^{-4}\ m^2$. Kerlo et al. (2013) concluded

from their experiments that the volumetric flow in the TCPC is $7.33 \times 10^{-5} m^3/s$. Filling this into Eq. 3.24 gives a velocity of $0.23\ m/s$. According to the experiments by Consiglieri et al. (2003) this results in a blood heat transfer coefficient of 1611 W/m^2K.

Table 5: Thermal resistance of the different actuator components.

	Medium	L in mm	Material	k in W/mK	A in m^2	R_{th} in K/W
R_{th1}	Stator core	0.3	Somaloy	25 ("Somaloy, Powders for Electromagnetic Applications,")	0.1056×10^{-3}	0.1136
R_{th2}	Air gap	0.14	Air	0.027 (Cengel, 2003)	0.1451×10^{-3}	32.15
R_{th3}	Magnet	0.25	NdFeb	8.9551(ToolBox, 2003)	0.1056×10^{-3}	0.2644
R_{th4}	Actuator case	0.2	Steel	50 (Young & Ford, 1992)	0.1797×10^{-3}	0.0107
R_{thout}	Surrounding fluid	-	Blood	1611 (Consiglieri et al., 2003)	0.5401×10^{-3}	16.3487

The materials used for the stator and magnet are the same as in the actuator by Pang et al. (2020). The case will likely be made from stainless steel.

Using Eq. 3.18 the resistivity of the wire is calculated. For the coil wire length, $\mathrm{l_{wire}} = 0.4972\ \mathrm{m}$, is taken, which considers 24 turns around the stator yoke. The cross-section for a wire with a 0.1 mm diameter gives, an area equals to $A_{wire} = 7.85 \times 10^{-9}\ m^2$. The resistivity of a copper wire is $\rho_{wire} = 1.7 \times 10^{-8}\ \Omega m$, which results in a resistance of the wire of 1.08 Ω. For the temperature calculations, the worst-case scenario is taken in which all the coils are controlled simultaneously; therefore, the wire resistance is $6 \times 1.08 = 6.45\Omega$. An input current of 0.3A results in a change in temperature of 19.6 K. The surrounding of the VIP is the blood temperature of 37°C, resulting in an internal temperature for the actuator of 56.6°C. 56.6°C is well below the maximum windings temperature of 155°C.

6. Characterization of the parameters of the actuator

The concept design presented in the previous chapter can theoretically produce a torque close to the required value; however, the efficiency was not considered. Also, the input parameters should be further evaluated. Therefore, chapter six first characterizes the various parameters that can be altered, and the efficiency is considered. Manufacturing processes and the materials of the components to create a working prototype based on the proposed actuator's concept were not considered. Therefore, the following chapter describes optimization and manufacturing processes. This chapter also discusses the components most likely to fail first and options to prevent such failures. The chapter concludes with a final design concept of the actuator considering the discussed matters.

6.1 Temperature, torque, and efficiency optimization

6.1.1 Temperature

First of all, the temperature is considered because the optimization of parameters is limited to the temperature increase caused by the influence of the input current, the diameter of the wire, and the air gap. Other components of the actuator do not influence the temperature significantly and are therefore not further discussed.

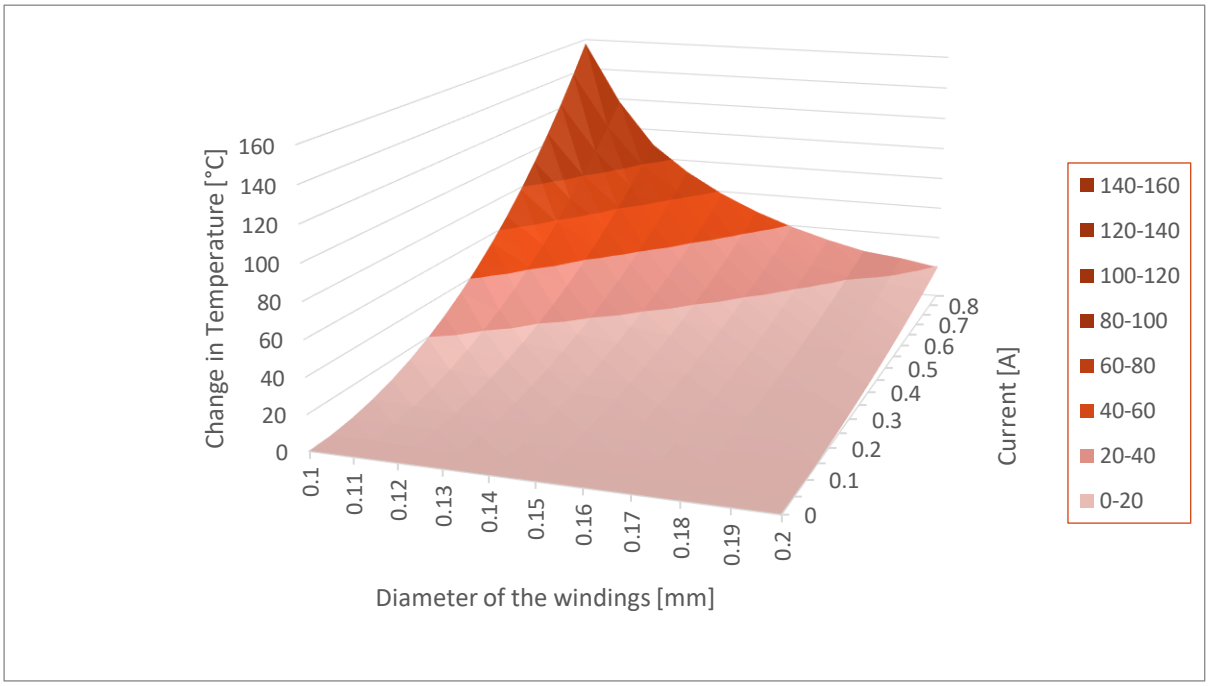

Figure 34: Change in temperature depending upon the diameter of the windings and the current. The color map depicts the temperature ranges, the darker the color, the higher the temperature.

Eq. 3.33 shows that the current input and the wire resistance have a direct influence on the temperature. Figure 34 depicts the relationship between the input current, the diameter of the windings, and the change in temperature, given that the other parameters are fixed (see Table 3). The blood has a temperature of 37°C, which leaves 118°C of maximum change in temperature when considering the maximum operating temperature of the wire of 155°C. Therefore, the absolute maximum current input can be 0.7A without changing the diameter of the windings. An input current of 0.7 A results in a temperature of 106.6°C and an internal temperature of 143.6°C.

Increasing the diameter of the wire would decrease the resistance of the wire (Eq. 3.18) and thereby reduce heat production. In addition, increasing the diameter of the wire would increase the space taken up by a wire in the stator slots and hence reduce the number of windings of the coils. If the diameter of the wire is doubled, the number of windings will be halved. This reduction of the number of windings decreases the length of the wire, further decreasing its resistance. The temperature developed is significantly reduced with

increasing wire diameter as expected because the most significant power loss is by the resistance of the wires, which creates heat.

Another parameter that influences the temperature is the air gap length. Reducing the air gap length would decrease the temperature generated in the actuator. The relationship between the air gap length and the temperature is linear; an enlargement of 10% of the air gap length causes a 43% increase in temperature. The consequences of changing the air gap length for the torque output are discussed in the next section.

6.1.2 Torque

In the next section, the various parameters influencing the torque output of the actuator are discussed.

6.1.2.1 Current

The current has a linear relationship with the torque, as a higher current will result in higher torque. However, the current is limited by the temperature increase which occurs in the windings due to its resistance. From Figure 34, it was concluded that a maximum current of 0.7A was the maximum current that could be used with a 0.1mm diameter windings. A current of 0.7A would result in a torque of 4002.5 µNm which is 2.3 times higher compared to a 0.3A current. However, increasing the current has two drawbacks. First, the generated temperature is closer to the maximum acceptable value which leaves less room for error and fluctuations. Secondly, the actuator's battery power needs to be larger to deliver a high ampere per hour rate.

6.1.2.2 Number of windings

The number of windings also has a linear relationship with the torque. The higher number of windings, the more torque an actuator can produce; however, the number of windings is limited by the space available in the stator. Therefore, the exact number of windings that can fit into the stator should be investigated when the stator is developed. A higher number of windings would be fitted into the stator if the yokes could be made thinner; however, first, the current dimensions of the stator should be tested before decreasing the thickness.

The wire diameter is related to the number of windings. Figure 35 shows the relationship between the wire diameter and the output torque. The number of windings is rounded during the calculations; therefore, the graph is a scatter plot.

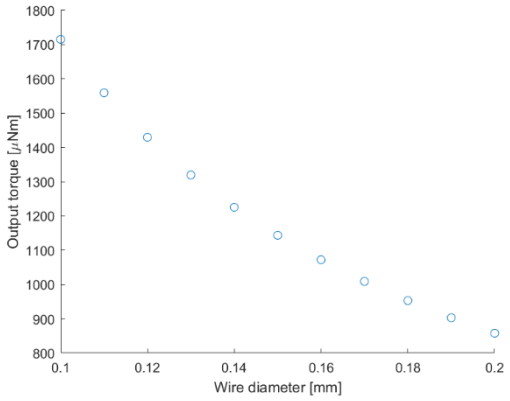

Figure 35: The influence of the wire diameter on the output torque.

6.1.2.3 Axial stack height

The relationship between the actuator's axial stack height (length of the actuator) and the produced torque is shown in Figure 36. An increase in the stator's length by 5 mm without altering its diameter and the input current causes a 45% increment of the torque output. Given that there is space available within the TCPC to accommodate the longer actuator, it is advisable to consider changing the concept design. Such an increase in torque output of the actuator with a longer stator is due to the larger air gap surface and larger actuator volume, as shown by Eq. 3.13. An increased length of the windings wire results in an increased power loss in the windings, as shown in Figure 36.

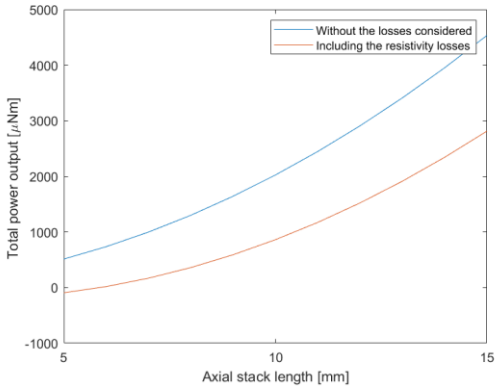

Figure 36: The influence of an increased actuator length on the output torque. For the values taken from table 3.

6.1.2.4 Air gap length

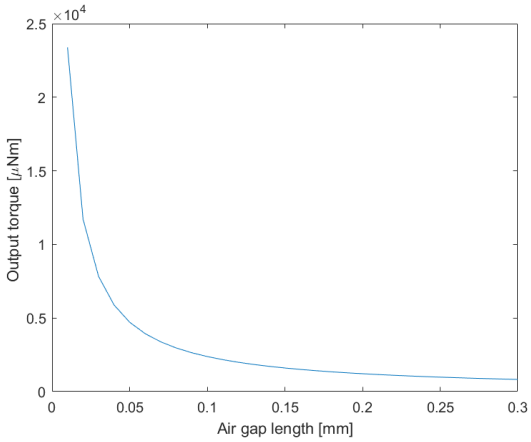

Figure 37: Influence of the air gap length on the output torque. Thereby, taking the input variables as in Table 3 and not considering the difference in size of other components because of the changed air gap length.

Figure 37 depicts the influence of the air gap length on the torque output. Decreasing the air gap length has a significant influence on the torque output. However, a very small air gap length can result in several drawbacks. The alignment of the stator and rotor need to be very accurate. Therefore, the tolerance of the parts needs to be very low, and the surfaces need to be very smooth. Also, minimizing the air gap length induces problems of armature reaction (Chau, Cui, Jiang, & Wang, 2006). The armature reaction is the magnetic field produced by the winding (Hanselman, 2003). The armature reaction strengthens the field in the air gap at the leading edge of each rotor pole arc, thereby causing magnetic saturation. However, on the trailing edge of the same rotor pole, the armature field opposes the air gap field and causes the air gap flux density to weaken. Because of these drawbacks and the already existing manufacturing challenges, the air gap length is chosen to be 0.14m, based on the actuator reported in Pang et al. (2020).

6.1.2.5 Magnet thickness

The magnet thickness has a very small influence on the torque if the magnet is thicker than 0.05 mm (Figure 38). Doubling the magnet thickness without reducing the inner diameter of the rotor would increase the torque by only 0.2%. Therefore, a reduction of the magnet thickness could be considered, thereby creating more space for the stator, resulting in a higher number of windings and higher torque output. However, the possibility for a reduction in thickness of the curved magnet can be limited to the manufacturing possibilities of magnets in the given shape and is not considered here further. In the future, the effect of magnet thickness on the magnetic field in the air gap needs to be investigated.

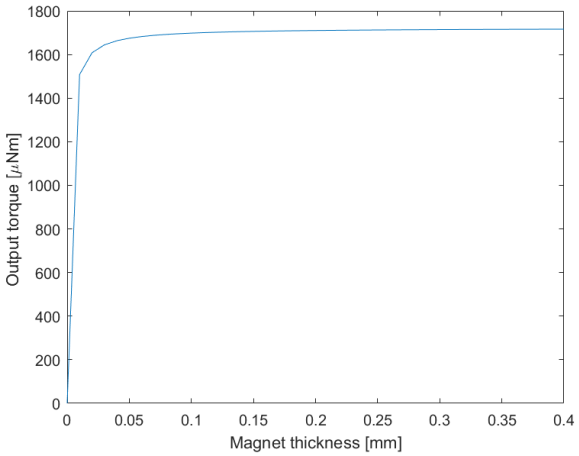

Figure 38: Influence of the magnet thickness on the torque output. Thereby, the input variables as in Table 3 and not considering the difference in the size of other components because of the changed magnet thickness.

6.1.2.6 Number of poles

The proposed concept design consists of four poles based on modifying of the inrunner electromotor reported by Pang et al. (2020). Increasing the number of poles would increase the torque, as can be seen from Eq. 3.13. As discussed earlier, the rotor of an outrunner electromotor generally has larger number of permanent magnets. The relationship between the number of poles and torque is linear; doubling the number of poles results in twice as much torque. However, the number of poles is limited by the space in the rotor and the induction of the cogging torque. Therefore, increasing the number of poles leaves less room for each pole resulting in increasingly narrower magnets, which can also pose manufacturing limitations. This can be partly compensated by decreasing the interpole length to zero. Finding this optimum value is a complex function between the rotor's geometry and magnet material's properties, according to Hanselman (2003). Due to the unknown effect of reducing the magnet size on the complexity and price of its

manufacturing, the original amount of four poles is kept for the presented actuator concept derived from Pang et al., 2020.

6.1.3 Efficiency

The losses due to the resistivity of the wire (Eq. 3.17) are the most dominant, accounting for nearly 80% of the total power losses. In Eq. 3.17, the current has a quadratic relationship with the power losses; hence, a decrease in the current causes a significant reduction in power losses resulting in higher efficiency (Figure 39). However, a decrease in current influences the torque, which will be discussed in the following section.

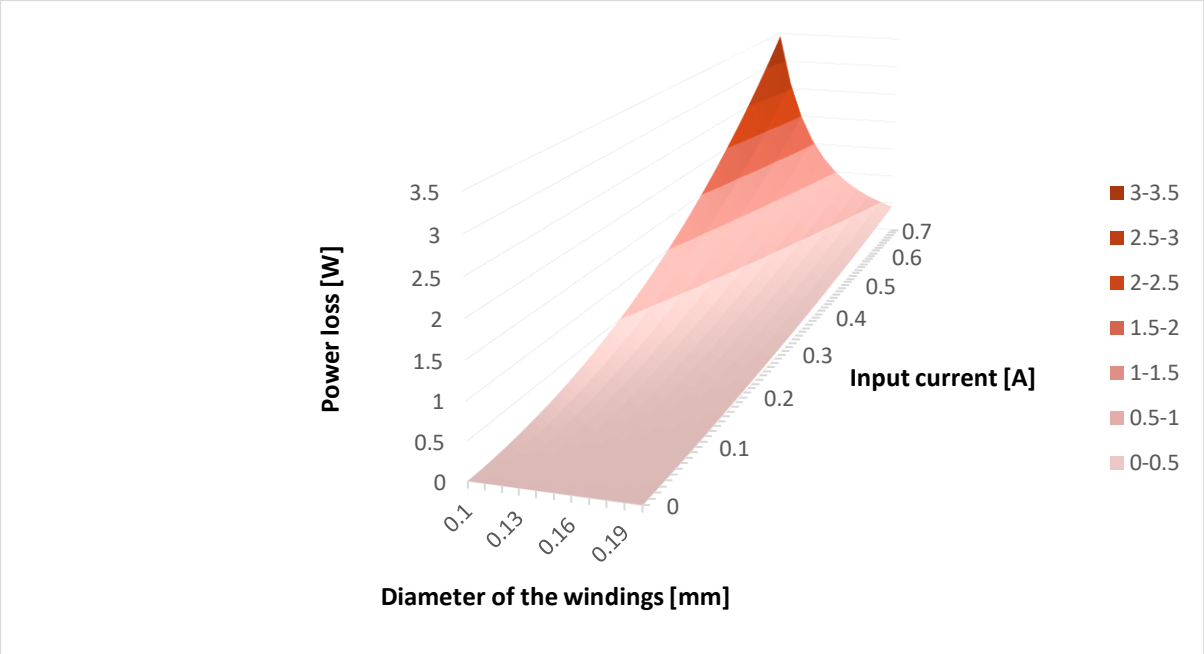

Figure 39: Power losses due to the resistivity in the windings based on the current and diameter of the windings. The color map depicts the power loss ranges, the darker the color, the higher the power losses.

Influencing the diameter of the wire is another approach to reduce power losses. A larger diameter of the wire lowers the wire's resistance and thereby lowers the power losses (Figure 39). In Figure 39, it is assumed that the resistance in the actuator is a summation of the resistances in the six coils. In addition, an increment in the wire diameter causes a reduction in the length of the wire and an increment in the cross-sectional area; both influence the wire resistance (Eq. 3.18). As discussed above, a larger wire diameter reduces the number of windings that can fit into the stator and the torque output. Therefore, the decreased power loss needs to be more significant than the losses in torque.

6.1.4 Torque, temperature, and efficiency combined

With all other actuator parameters fixed, the influence of the wire diameter on the torque (Figure 35), the influence of the current on the torque, and the influence of the current and diameter of the windings on the power losses (Figure 39) are shown in Figure 40. The power output is calculated with the torque Eq. 3.27 and Eq. 3.28. The rotational speed was set at 5000 RPM. The total power is calculated by subtracting the power losses in the wires (Eq. 3.20) and the mechanical losses (Eq. 3.25) from the power output. The highest total power output was for a wire with a diameter of 0.19 mm, which corresponds to 13 turns of copper windings and a current of 0.79A. The power output is 0.632 W, which results in a torque output of 2446.8 µNm. This is well above the required 1768 µNm.

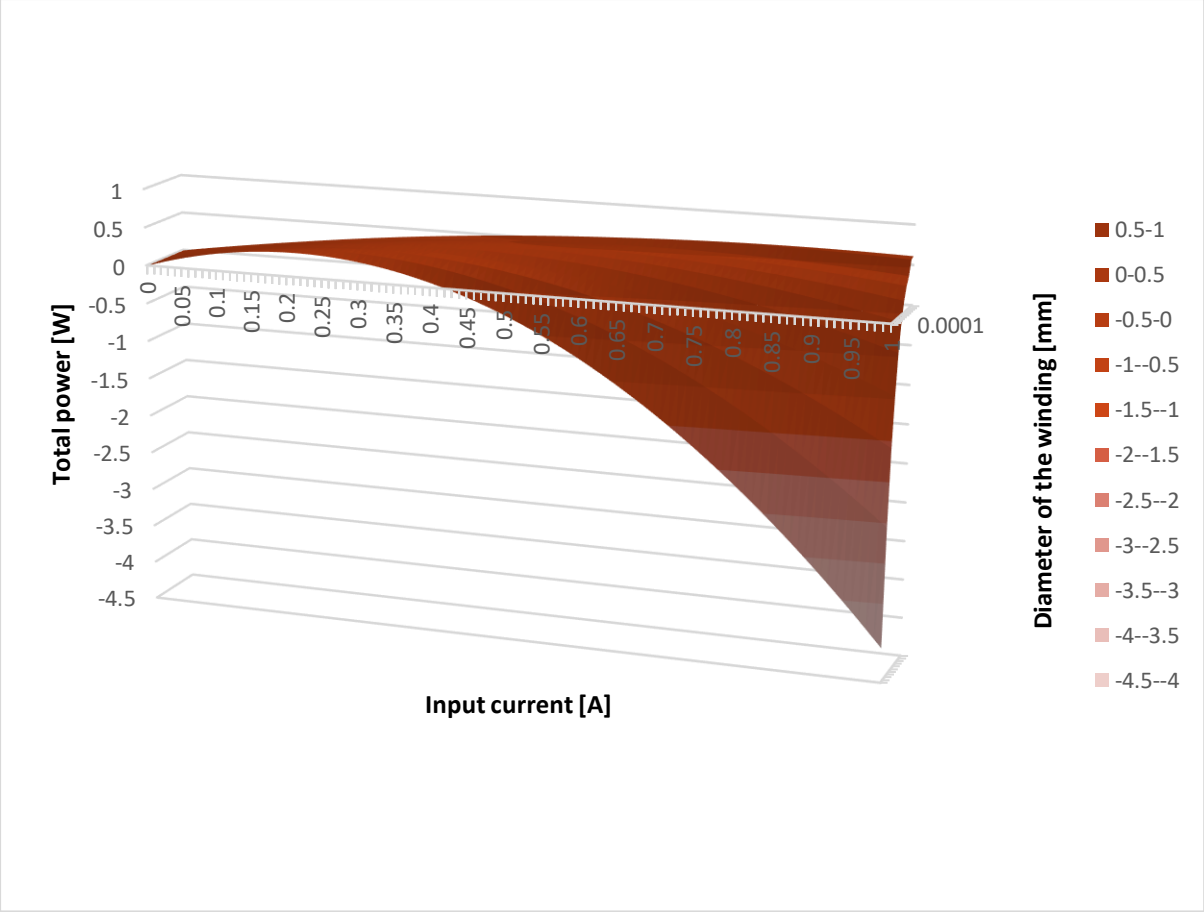

Figure 40: The actuator's total output power depended upon the current and the diameter of the windings. The total power is calculated by subtracting the mechanical power losses, friction power losses, and resistivity power losses from the power output The color map depicts the power loss ranges, the darker the color, the higher the power losses.

As discussed in the previous chapter, a current of 0.7A is the highest current that should be taken due to excessive heat generation in the motor having windings with the 0.1 mm diameter wire. However, when taking a larger diameter of the wire, the resistivity and the temperature are lower. Recalculating the temperature with the current values gives a change in temperature of 20.5 K, which results in an internal temperature of 57.5 °C. Therefore, these results show that the highest torque output can be achieved with a wire diameter of 0.19 mm along with a number of windings of 13 and current input of 0.79A.

6.2 Manufacturing and availability of the materials

In the next section, the manufacturing of the various components is described, along with the changes suggested for the proposed design to make them manufacturable. The materials for different components are also discussed based on the manufacturing method and availability of off-the-shelf components.

6.2.1 Case

The outer casing around the actuator has several functions, with the primary function being the holder for magnets. The magnets are directly attached to the case. The outer casing also becomes functional to seal the actuator of the ambient media. The casing in the currently proposed concept is a 0.1 mm thick tube made of stainless steel with an outer diameter of 5.4 mm. A commercially available capillary tube of stainless-steel ASIA (304) has a wall thickness of 0.2 mm (Metalen, 2021). This slightly thicker capillary tube has an inner diameter of 5 mm, which will need a slight reduction in the dimensions of the other components to be fitted inside.

6.2.2 Manufacturing of the stator

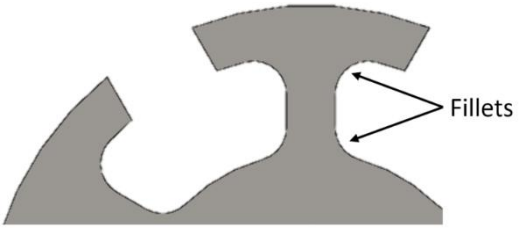

Figure 41: One and half stator yokes are depicted showing the fillets in the corners. 2 of the six fillets in the picture are indicated by arrows.

Manufacturing the stator is a challenging task due to the T-shaped yokes. Milling, metal 3D printing, and wire electrical discharge machining (WEDM) are options for machining small-sized metal components. Milling is not an option for the stator because of the shape of the T-shaped yokes. Electrical discharge machining is a manufacturing method that can be used with electrically conductive materials in which precisely controlled sparks occur between an electrode and the workpiece in the presence of dielectric fluid (Jameson, 2001). An electrode is used as a cutting tool, which is in WEDM a continuous wire. The sparking in WEDM takes place from the electrode wire-side surface to the workpiece. Metal 3D printing is a manufacturing process in which a high-powered laser selectively binds particles together on a powdered bed while the machine distributed even layers of the metallic powder (Materialise, 2021). Both methods are different from each other with the biggest difference being that in WEDM, the part is cut out of as a solid metal piece and in metal 3D printing, the parts are built up out of metallic powder. Therefore, machining the stator out of WEDM results in a stronger piece. Another advantage of using WEDM is that the surfaces of the stator are smooth. Smooth surfaces are essential for creating a small-sized air gap. If the surfaces are not straight, the air gap distance cannot be kept the same around the whole stator. The surfaces resulting from metal 3D printing are rough and need to be post-process to make them smooth. Post-processing complicates the manufacturing process, especially for the small-sized stator. Therefore, WEDM is chosen as the preferred manufacturing method for the stator.

The TU Delft electronic and mechanical support division (DEMO) has a WEDM machine that can either be equipped with a 0.25mm or a 0.10mm wire (Roessen & Bakker, 2021). A wire of 0.25 mm results in a cutting slot of 0.32 mm, which means that the minimum radius will be 0.16 mm in corners. A larger wire has the advantage of giving fewer problems during manufacturing because it is stronger and less likely to break. The 0.16 mm radius fillets are included in the design and do not reduce the amount of winding space when the 16 windings of a 0.15 mm diameter copper wire are chosen (Figure 41). Therefore, using the 0.25 mm cutting wire for manufacturing is advised in this study. A rough estimation of the price of manufacturing for stator is around 800 Euros; this is based on a 40 Euro hour rate and an estimated manufacturing time of 20 hours.

6.2.2.1 Stator Material

The main condition for materials to be machined with WEDM is that they need to be electrically conductive. Pang et al. (2020) described a stator out of Somaloy 700 with the use of WEDM. Somaloy is a soft magnetic component. It was concluded from their experiments that actuators made from Somaloy have a 9.1% higher performance as compared to silicon steel actuators. However, Somaloy is a sintered material. Sintering is the process of forming materials by heating the grains of material to a temperature just below the melting point under pressure (German, 1996). This causes the contact points of the grains to grow together to form the material. The downside of sintered materials is that they are weaker than the ASIA (304) grade stainless steel (Hoganas, 2018; Lingadurai, Nagasivamuni, Muthu Kamatchi, & Palavesam, 2012). However, because of the higher performance of Somaloy, it is still advised in this study as the preferred material for manufacturing the stator.

6.2.3 Windings

Copper has excellent electrical conductivity and is generally used to make the actuator's windings (Hanselman, 2003); therefore, copper is chosen as the material for the windings in the current actuator design and its analysis. In the preliminary concept of the actuator, the windings had a diameter of 0.162 mm taken directly over from the actuator prototyped reported by (Pang et al., 2020). Similar to the other components, the wire diameter was also scaled down to 0.1 mm. After the optimizations for the power losses, as discussed in the previous chapter, the optimal diameter of the wire is 0.15 mm, which is readily available commercially (Conrad, 2021).

6.2.3 Permanent magnets

PMSM and BLDC actuators of all sizes and especially the small ones use neodymium-iron-boron (NdFeB) rotor's material for the permanent magnets (D. Han, Nagai, & Tadahiko, 2020; Pang & Lai, 2017; Wang et al., 2017). NdFeB has a high magnetic density to the higher performance of the actuator (J. H. Kim, Jung, & Sung, 2006). NdFeB is widely available for producing magnets with custom size, form and magnetization direction and is chosen as the material for the current actuator concept.

The interpole length in the initial design concept was scaled-down from 1.6 mm to 0.58 mm as reported by Pang et al. (2020). Their research concluded the simulations that an interpole distance of 1.6 mm was the optimum for the inrunner electromotor resulting in a high torque density and a low motor volume. However, including an interpole length between the permanent magnets complicated the design of the rotor for the current actuator concept. Because the experiments by Pang et al. (2020) showed that the highest average torque was with the zero interpole length and for the analysis of the current concept, the interpole length is set to zero. However, the generation of torque ripple at such a short interpole distance should be investigated after the prototype is built.

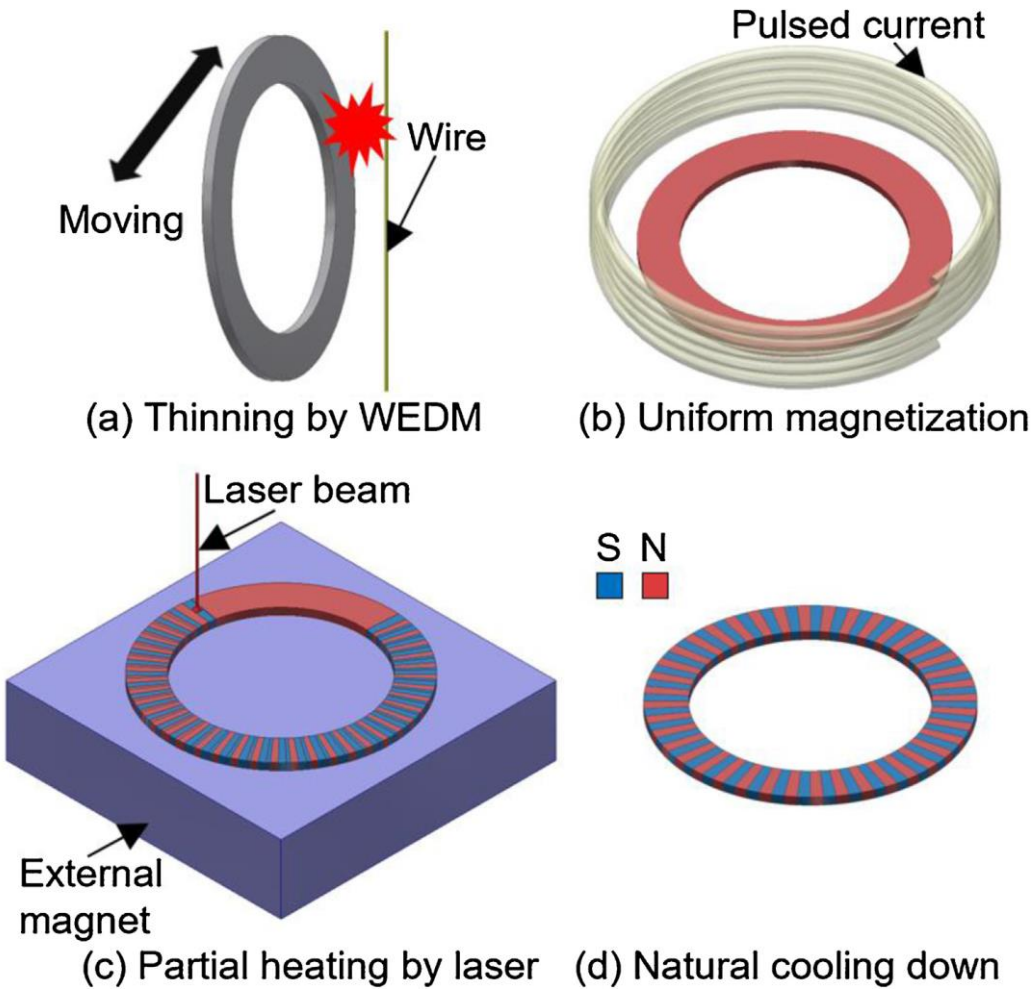

Figure 42: Manufacturing process of the multipole ring by D. Han et al. (2020). A) A thin ring of the material the magnet is going to be made of, cut by WEMD. B) The material is magnetized using a pulsed magnetizer. C) A laser beam selectively heats the upper surface of the magnet, creating different poles. D) the magnet is cooled down naturally.

Unfortunately, there are no magnets found in the required size or close to the required size. Therefore, the magnets need to be custom-made for the current given design. An example of a 1 mm thick ring magnet with an outer diameter of 10.5 mm and 120 poles were reported in the study by Han et al. (2020) (Figure 42). The multi-pole magnet ring were manufactured by cutting a bulk magnet to the designed size. After the thin ring was produced using the WEDM, it was unidirectionally magnetized using a pulsed magnetizer (Figure

42b). Then the magnet was fixed onto the center of a NdFeB magnetic block, which provides an external magnetic field (Figure 42c). A laser beam then selectively heated the upper surface of the magnet, created the reverse magnetic directions and different poles. They called this process single-sided laser-assisted heating, as only the upper surface was heated. A layer of anti-corrosive material can be added to make the magnet more resistant to corrosion.

The described process could potentially be used to create the ring magnet for the current actuator concept with modification of the magnetization direction. The addition of multiple rings with different poles could potentially increase the actuator's torque output. However, a significant difference is that the magnet of the current concept is vertically orientated instead of horizontal configuration (Figure 43), and hence potentially complicating the laser beam process. The magnet for the proposed concept is thinner, which might not be feasible with the above-described technique. Therefore, for a simple process of prototype manufacturing, it is advisable to produce a rotor with only four curved permanent magnets and a small interpole length. Preferably, an external company should manufacture the magnets for the rotor.

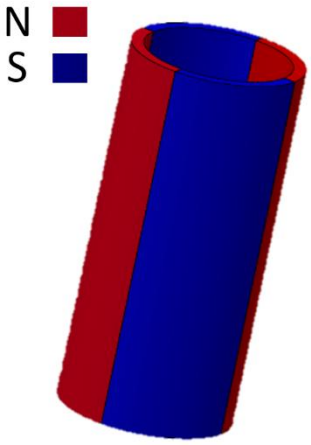

Figure 43: Vertically oriented permanent magnet with four poles. The red indicates the north poles and the blue the south poles.

6.2.4 Central shaft

In the current concept design and analysis, the central shaft holding the actuator in place was neglected. There are two ways to manufacture the shaft: incorporating the shaft into the stator design or producing a straight tube which is then pressed into the stator.

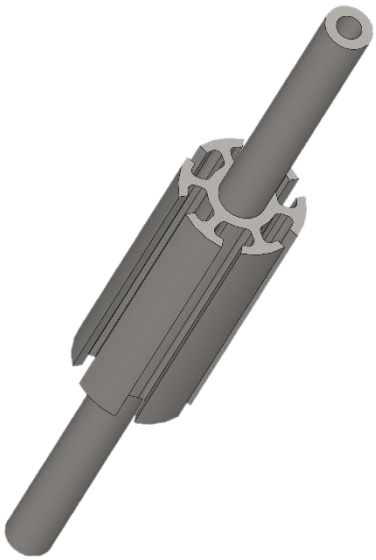

Figure 44: The shaft inside the center of the stator with a hole through the middle.

Incorporating the shaft into the stator design complicates the manufacturing because either pre-processing or post-processing is required and is not advisable. A loose shaft simplifies the manufacturing process significantly, but it needs to be strongly attached to the stator with no slippage. Welding or gluing can prevent slippage or breakdown. Furthermore, for the optimal and safe functioning of the actuator, it should be sealed off from the ambient media, which in the current case is blood, while allowing the free continuous movement of the rotor around the stator and the central shaft. Given the need for access of the electrical wires from the battery and control unit to the actuator, the central shaft should be hollow at least at one end (Figure 44). The commercially available capillary tube of 1.5 mm diameter with a thickness of 0.35 mm is used for the shaft (Metalen, 2021). In addition, a hole on the side of the shaft needs to be drilled to let the wires go through the holes. The interior of an outrunner electromotor fixed to the middle of a central shaft can be achieved using the miniature ball bearings.

6.2.5 Bearings

Components in contact with each other have an increased risk of wear and tear. In the current concept of an actuator, the only rubbing parts are the balls and their cage inside the bearings sealing off the electromotor (Figure 45). These bearings are not included in the analysis of the current prototype nor the mechanical coupling between the actuator's rotor and the VIP is addressed here. Both mechanical frictions of the motor bearings and the mass of the VIP rotating together with the rotor will affect on the actuator's torque output and should be further investigated. To get insight into the geometrical configuration of an outrunner actuator sealed off by the ball bearings, a commercially available model is included in the 3D rendering of the current concept (Figure 46). The addition of two 2.5 mm high bearings to the actuator's rotor will increase the total actuator's length to 16 mm. Thinner bearings could be used in case of encountering problems of fitting the actuator into the VIP.

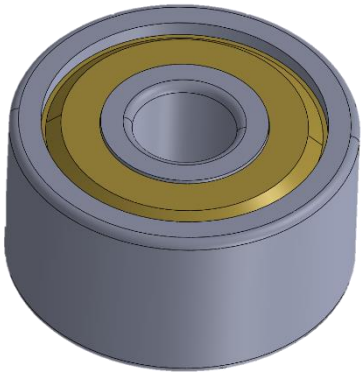

Figure 45: A 2.5 mm high bearing with an outer diameter of 5 mm and an inner hole of 1.5 mm. 5 0.6mm small balls are inside the bearing allowing the rotation. The bearing is sealed, and no air nor water enters.

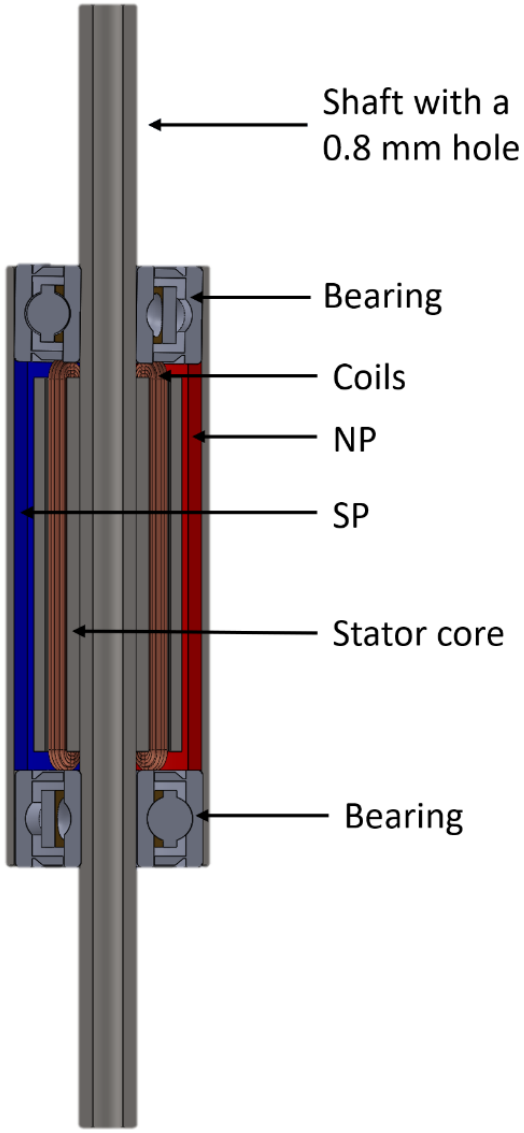

Figure 46: Cross-sectional view of the actuator showing the components with two bearings added to seal the top and bottom of the actuator.

6.3 Components first to fail

One of the requirements is that the VIP should run for at least three years without being serviced. In the following section, different components and mechanisms that can potentially fail are discussed. First, the forces acting on the stator are discussed, followed by the mechanical failure potentials, and finally, the electrical failure is discussed.

6.3.1 Stator

The strength of the stator is currently still uncertain. A force simulation was conducted using SolidWorks (Dassault Systèmes, Vélizy-Villacoublay, France) to investigate the locations of the weak points (Figure 48). The simulation should be used to identify the weak points but not as an accurate measure of the forces and stresses applied on the stator. A static 3D force simulation was chosen in the given study. In this simulation, the material of the stator was set at stainless-steel AISA 304 for the sake of simplicity.

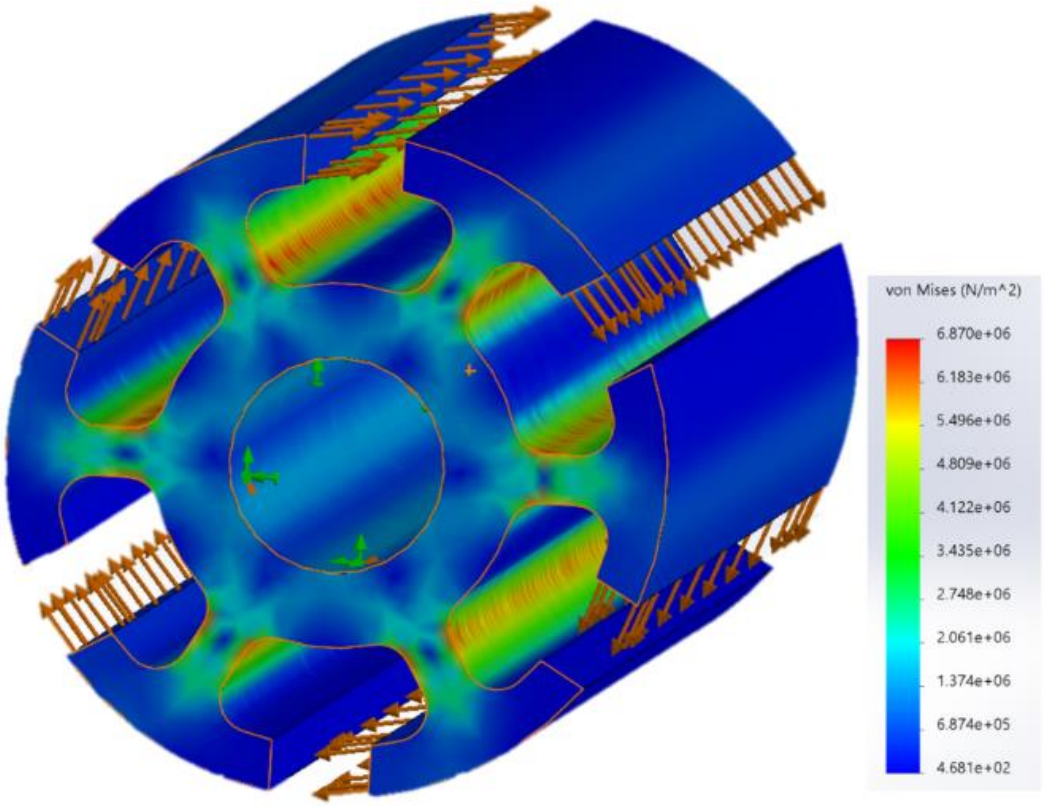

Figure 47: Stress distribution on the stator. The green arrows in the middle indicate that the actuator is fixed in the inner circle of the stator. The orange arrows indicate the torque applied to the stator yokes. The red zones show the highest concentrations of stress. The scale shows the values of the colored areas in N/m^2.

The boundary condition for the study is a fixed inner circle of the stator, mimicking its fixation to the central shaft that keeps the actuator in place. The meshing was set to the finest setting available in SolidWorks; this did not significantly increase simulation time. A torque force of 2446.8 µNm obtained in the previous chapter (ch.6.1.4) was applied to the yokes. The point of engagement of the force was assumed to be at the top of the T-shaped yokes because this part is most likely to experience the Lorentz force pushing the rotor around the stator. The center of the actuator was set as the axis of the torque. To obtain the magnitude of torque per yoke, assuming that the torque is equally distributed over the six yokes, resulting in 407.8 µNm per yoke. The results of the simulation can be seen in Figure 48. The stress shows the force experienced by the object, whereas the strain shows the change of the object's shape when stress is applied. The highest stress concentration is indicated by the red in Figure 48. The highest stress and strains are where the T-shaped yokes are connected to the middle ring. These stresses can be reduced by increasing the radius of the fillets smoothing the connection between the stator core and yokes. Increasing the fillet radius would increase the strength of the yokes but should not interfere with the amount of copper wire turns fitting in

the stator. An optimum between the two should be found. With 15 turns and a diameter of 0.15 mm, the maximum fillet radius of the fillets can be 0.2 mm instead, which is a little larger than the 0.16 mm radius fillet needed for the manufacturing.

Another more drastic approach to increase the strength of the stator can increase the thickness of the base of the stator yoke. By increasing this thickness, the space for the windings is reduced. Increasing the thickness of the base of the yoke to 0.5 mm, reduces the space of the windings by reducing the number of windings by 5, thereby reducing the torque by about 20%. An alternative to this approach is to increase the thickness of the base of the yoke closest to the stator and then gradually reduce the thickness of the base of the yoke towards the top of the yoke. For the current prototype, these last two options are not considered, and the current thickness of 0.3mm will be tested first.

6.3.2 Other causes of failure

Besides the above mechanical components that can fail, the motor can also fail due to overheating and other electronic problems. One of the most common causes of actuator failure is low resistance caused by the degradation of the insulation of the wire windings due to overheating, corrosion, and physical damage (Acorn, 2018). The degradation of the insulation can cause current leakages and short circuits, which leads to actuator failure. Preventing this is difficult because an inspection of signs of wear is not possible when the actuator is implanted inside the patient. Therefore, the potential for degradation should be minimized. As already mentioned, the actuator needs to be sealed off from the blood surrounding the actuator. Adding corrosion-resistant insulation to the wires and the other component of the actuator is the only other protection against corrosion.

Another cause of failure in the motor is an overload due to an excessive current flowing through the windings (Acorn, 2018). If the current overload exceeds the limits of the copper wire, the wire will melt. A low voltage supply can cause a current overload because the actuator will maintain the torque output by drawing more current. Short circuited conduction or excessive voltage supply also causes electrical overload. A solution is to install adequate over-current protection, which detects overcurrent and interrupts of the power supply. For the actuator, however, the intended voltage of the battery that will supply the electrical current is already limited to 3 V, and thereby, the risk of current overload happening is low.

Over-heating of the actuator is another cause of failure. As calculated in 5.1.2, the current internal temperature of the continuously working actuator is estimated to be 71.8 °C, which is less than half the insulated wire can handle. Therefore, this risk for the current actuator is not significant.

6.4 Final actuator design

All the dimensions and other parameters for the final design of the actuator are given in table 6 and Figure 49. Table 7 lists the components for manufacturing the actuator, the materials the components to be made of, the manufacturing technique, and the advised place where the components could be manufactured.

Table 6: The final dimensions (in mm) and parameters of the actuator design

	All dimensions are in mm	**symbols**	**Final design**
General			Outrunner
	Number of phases	-	3
	Input current	-	0.79 A
	Voltage input	-	2.36 V
	Air gap length	δ	0.14
	Axial stack length	L_{st}	16.2
	The outer diameter of the actuator	D_{ao}	5.4
Stator	Outer radius	S_{ro}	2
	Inner radius	S_{ri}	0.65
	Number of slots	N_s	6
	Slot opening	SO	0.6
	Yoke base thickness	YBt	0.3
	Core back length	CB	0.45
	Shaft diameter	D_{sh}	1.3
	Axial stack length	L_{st}	10
Rotor	Outer diameter	R_{ro}	2.5
	Inner diameter	R_{ri}	2.14
	Number of poles	N_m	4
	Interpole width	IP	0
	Magnet thickness	h_m	0.36
Windings	Number of windings	N	13
	Diameter of the wire	D_{wir}	0.19
	Type of connection	-	Star
	Type of distribution	-	Concentrated
Bearings	Stack height	B_{st}	2.59
	Outer radius	B_{ro}	2.5
	Inner diameter	B_{ri}	0.75
Shaft	Stack height	S_{st}	30
	Outer diameter	Sh_{ro}	1.5
	Inner diameter	Sh_{ri}	0.8

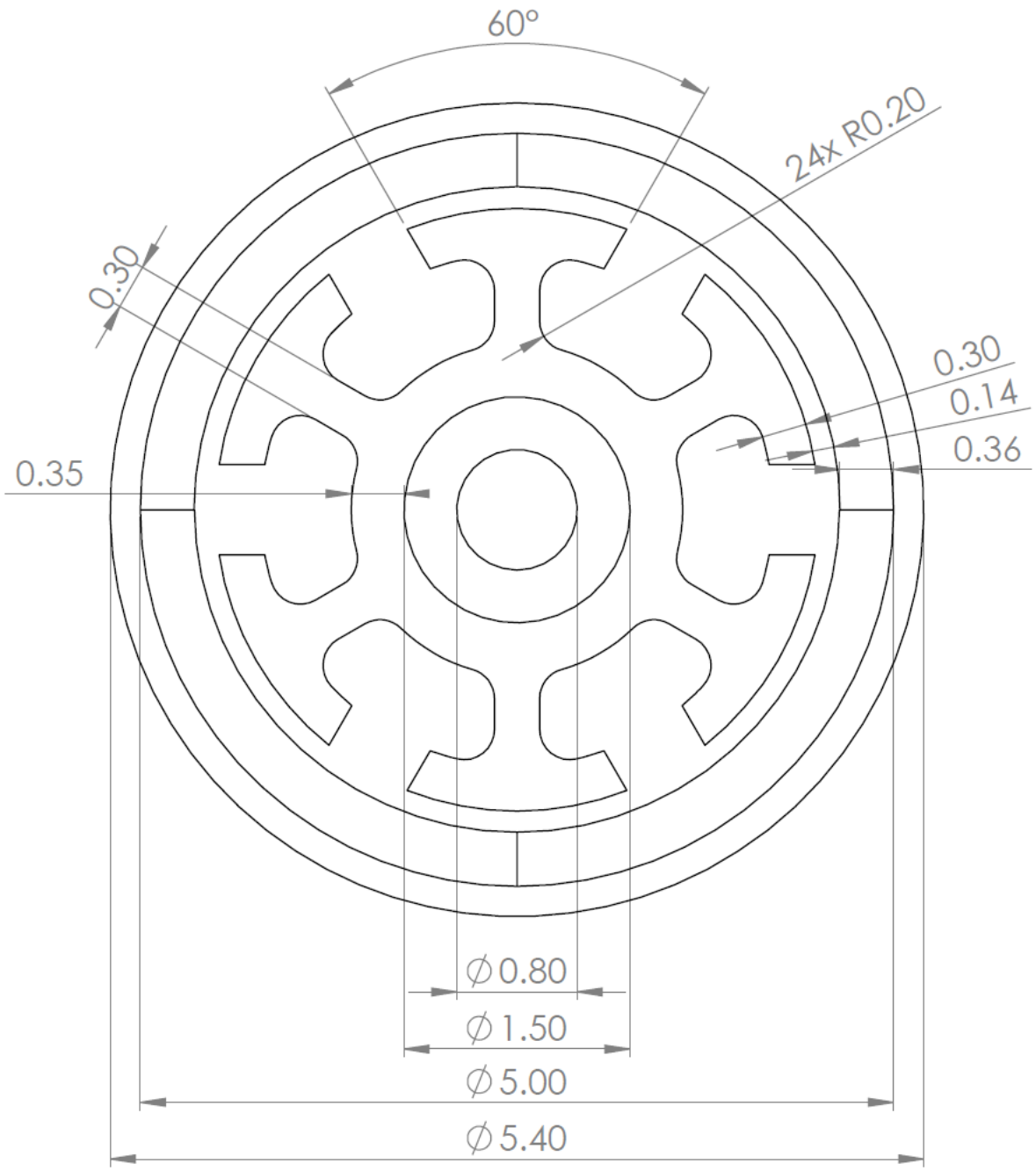

Figure 48: Top view of the inside of the actuator with all the dimensions.

Table 7: List of components, the material the component is made of, the manufacturing technique, and the place the components could be manufactured.

Components	Material	Manufacturing technique	Place of manufacturing
Shaft	Stainless steel AISI 304	Store-bought	Salomon's metalen
Magnets	NdFeB	Custom made	Commercial website
Stator core	Somaloy or stainless steel	WEDM	TU Delft
Coils	Copper	Store-bought	Conrad
Case	Stainless steel AISI 304	Store-bought	Salomon's metalen
Bearing	AST bearing 691XHZZ	Store-bought	(AST bearings)

6.4.1 Assembly

After manufacturing the stator, a 1.5mm diameter capillary tube intended to be the central shaft holding the stator in place should be pressed, welded or glued to the stator. Then, the copper wire is wrapped around the stator yokes creating the coils. Wrapping the wires is a very delicate process and intense care should be taken to avoid the yokes bending. After that, permanent magnets will be attached to the case, which can be done by the glue added to the inner side of the case. Then the stator should be placed in the middle of the rotor and the two bearings are slide onto and firmly attached to the central shaft by their inner ring. The outer rings of the ball bearings are then firmly attached to either end of the rotor's case of the actuator. Figure 50 depicts the exploded view of the components of the actuator.

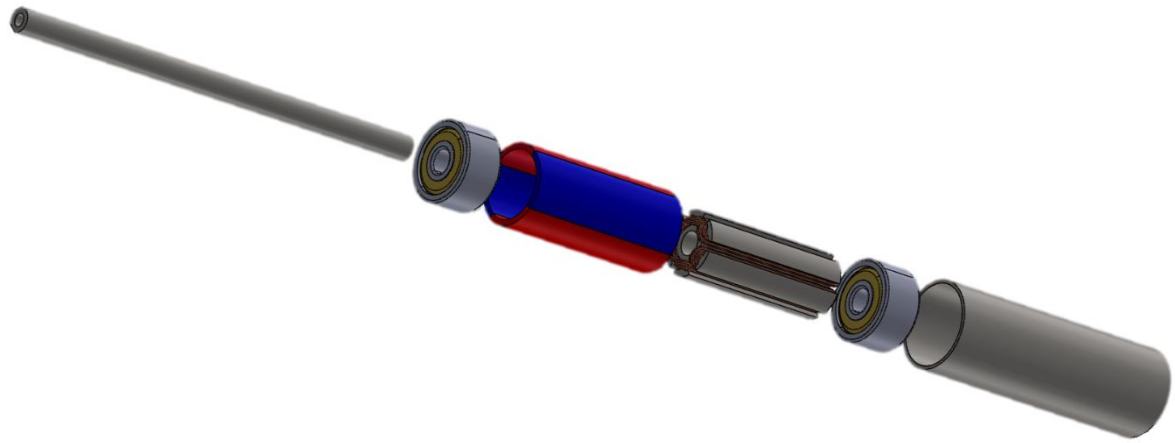

Figure 49: Exploded view of the actuator with two added bearings. In the center of the shaft a hole is made to allow the electrical wires pass through.

7. Tests

After the prototype is built, several experiments need to be conducted to validate the design, such as torque tests and circulatory mock loop experiments for the evaluation of hydraulic power, temperature, and a lifetime of the actuator. This chapter outlines the possible setups for these tests based on the published literature.

7.1 Torque test

The primary purpose of the torque test is to find the value of the continuous torque output of the actuator. Besides testing the torque value, the torque test also serves to evaluate the functioning of the actuator. As a safety precaution to ensure the actuator does not overheat, the temperature is continuously measured.

7.1.1 Input and output variables

For the torque test, the current is the primary input variable. Voltage is also taken as an input variable; however, the voltage is directly related to the current. The current input will range from 0 to 0.5A. The RPM is dependent upon the voltage input of the actuator and is set at 5000 RPM. The output parameter is the measured torque and the temperature.

7.1.2 Test setup

The test setup presented in this study is from Cham and Samad (2014). Figure 51 depicts a schematic diagram of the setup studied in the literature. The power supply is a bench power supply that allows for varying the input current and voltage quickly over a wide range. The bench power supplies a direct current voltage. Initially, it is proposed to control the prototype in a BLDC configuration achieving a less complicated control. A motor dynamometer is connected to measure the torque and rotational speed of the actuator simultaneously. In addition, an embedded thermocouple with a diameter of 0.075mm sensor is placed inside the shaft of the actuator to measure the temperature (RSPro, 2021c). The accuracy of this sensor is 1.5°C which is accurate enough for the current measurements. The current sensor is added as an additional check of the current powered from the bench power supply. In the current prototype, there is no motor driver included. The size of the motor driver does not matter for the tests. Therefore, a development circuit board (DM183021 (Farnell, 2021)) is used as the motor driver. The Arduino board is used to extract the information from the dynamo. The PC is connected to the development circuit board and controlled with the software packet of the circuit board. The actuator is set to a constant velocity of 5000 RPM by the motor driver. Arduino is programmed such that the torque output and rotational velocity from the dynamo are registered to the PC.

7.1.3 List of materials

- Current sensor
- DM183021 development circuit board (Farnell, Leeds, United Kingdom)
- Arduino board
- PC
- Motor dynamometer
- Bench power supply
- Embedded thermocouple (RSPro, Haarlem, The Netherlands)

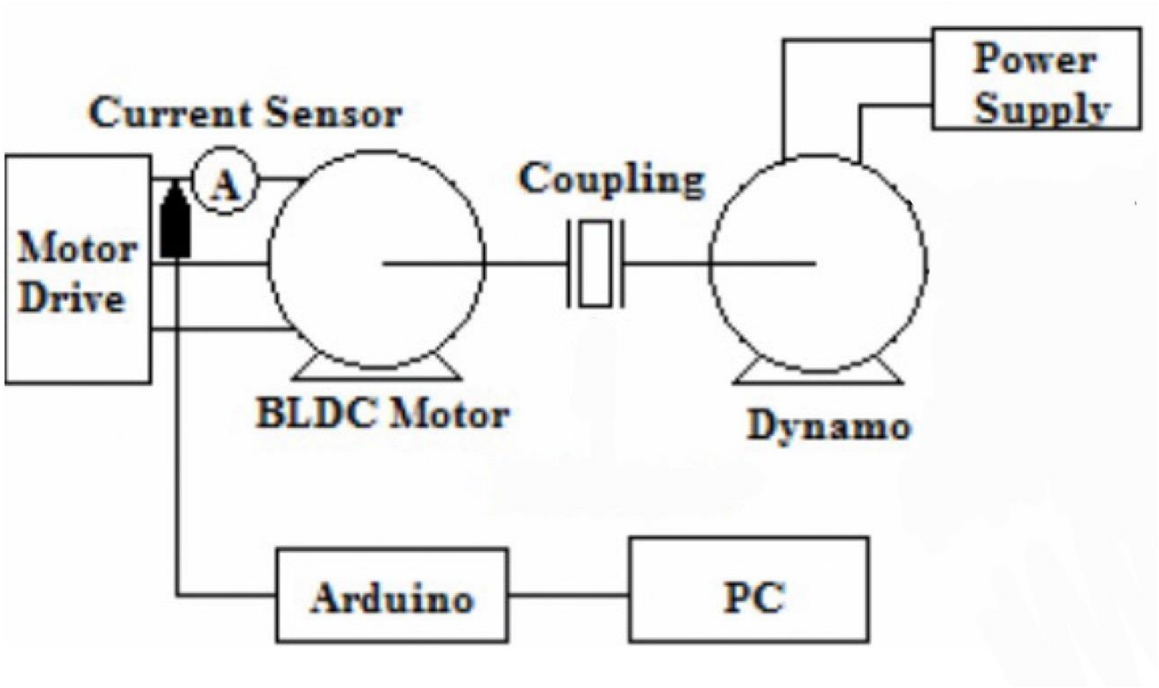

Figure 50: Schematic diagram of the setup by Cham and Samad (2014) adjusted for the torque test.

7.1.4 Test protocol

Before the experimental protocol, a test run is performed to evaluate the actuator's performance, whereby the motor driver is set to rotate at 1000 RPM at a current input of 0.2A. If the actuator rotates appropriately, the following experiment is performed.

1. The setup should be built as above-described and depicted in Figure 51.
2. During the whole experiment, the temperature should be monitored. If the temperature increases above 100°C, the test should directly be aborted.
3. Increase the current in 5 steps of 0.01A in time increments of 5 minutes from 0 to 0.5A. When the current is increased, the voltage decreases and should be kept such that the rotational velocity remains at 5000 RPM.
4. Save the torque output information and the rotational velocity information for each current increment.
5. Repeat step 3 and 4, three times to get a reliable measurement.

7.1.5 Data processing

The current, voltage, and torque outputs per step are saved through the Arduino onto the PC. The relationship between the current and the torque output should be displayed in a graph, including the voltage information. From this information, the optimal current and voltage can be found to power the actuator. Depending on the maximum continuous torque output, the actuator requires further optimization, or the VIP test should be performed. The torque test is successful if the actuator runs appropriately and has a torque output of at least 50% of the required torque. For the temperature, only the maximum temperature is of interest.

7.2 Hydraulic test

The hydraulic experiments are performed once the satisfying results of the torque tests have been achieved with the actuator. The hydraulic test is copied as accurately as possible from the hemodynamic studies performed by the group of Rodefeld; therefore, the results of this test are comparable with the findings of the Rodefeld group. This is important to evaluate the functioning of the actuator within the VIP inside the TCPC. Rodefeld used a circulatory mock loop to perform the hemodynamic studies with their 3D printed VIP prototype driven by an electromotor outside the VIP. For the current test, the actuator will be placed inside a 3D printed VIP.

The hydraulic tests measure three parameters: blood temperature surrounding the VIP, hydraulic power of the VIP, and the actuator's lifetime, which is called the fatigue test. The blood temperature surrounding the VIP is measured as the blood should not exceed 40 degrees. According to Rodefeld et al. (2019) and Granegger et al. (2019), the temperature increase of the surrounding blood does not exceed 0.1 degrees. Still, due to the potentially lethal consequences, the test should repeat with the current actuator design.

The second component of the VIP test evaluation is hydraulic power. The hydraulic power is calculated by measuring the flow rate increment and pressure rise which the VIP produces.

The final component is the fatigue test, testing the time until service is required. The requirement of the actuator state that the actuator should last at least three years without the service requirement. The fatigue test is usually not run for three years, but the conditions are modified to accelerate the potential failure of the actuator's components. After that, the prototype is taken apart and checked for damage to any components. The fatigue test should only be conducted if at least two actuator prototypes are available because this test is prone to damage the actuator.

7.2.1 Input and output variables

The current and voltage that produces the required or closest to the required mechanical power in the previous test are taken to measure temperature and hydraulic power. The rotational velocity is set at 5000 RPM to replicate the setting in the experiments by Kerlo (2013). For the fatigue test, the input will be altered to push the actuator. The variable inputs for the fatigue test are the viscosity of the fluid and the RPM.

The test has three intended purposes and, thereby, three variable outcomes. The first is the temperature of the fluid around the actuator at different locations. Second, the hydraulic power is measured by measuring the flow rate and the pressure rise across the VIP. Third, the fatigue of the actuator is assessed using visual inspection and the hydraulic power and temperature output.

7.2.2 Test set-up

The test setup proposed here is based on the in-vitro experiments conducted by the research group of Rodefeld (Kerlo, 2013) (Figure 52). The setup consists of a mock circulation loop simulating the single ventricle physiology with a 4-way idealized TCPC intersection, mimicking adult's Fontan circulation anatomy and hemodynamic conditions. The prototype of the VIP driven by the enclosed actuator will be placed inside the TCPC for evaluation.

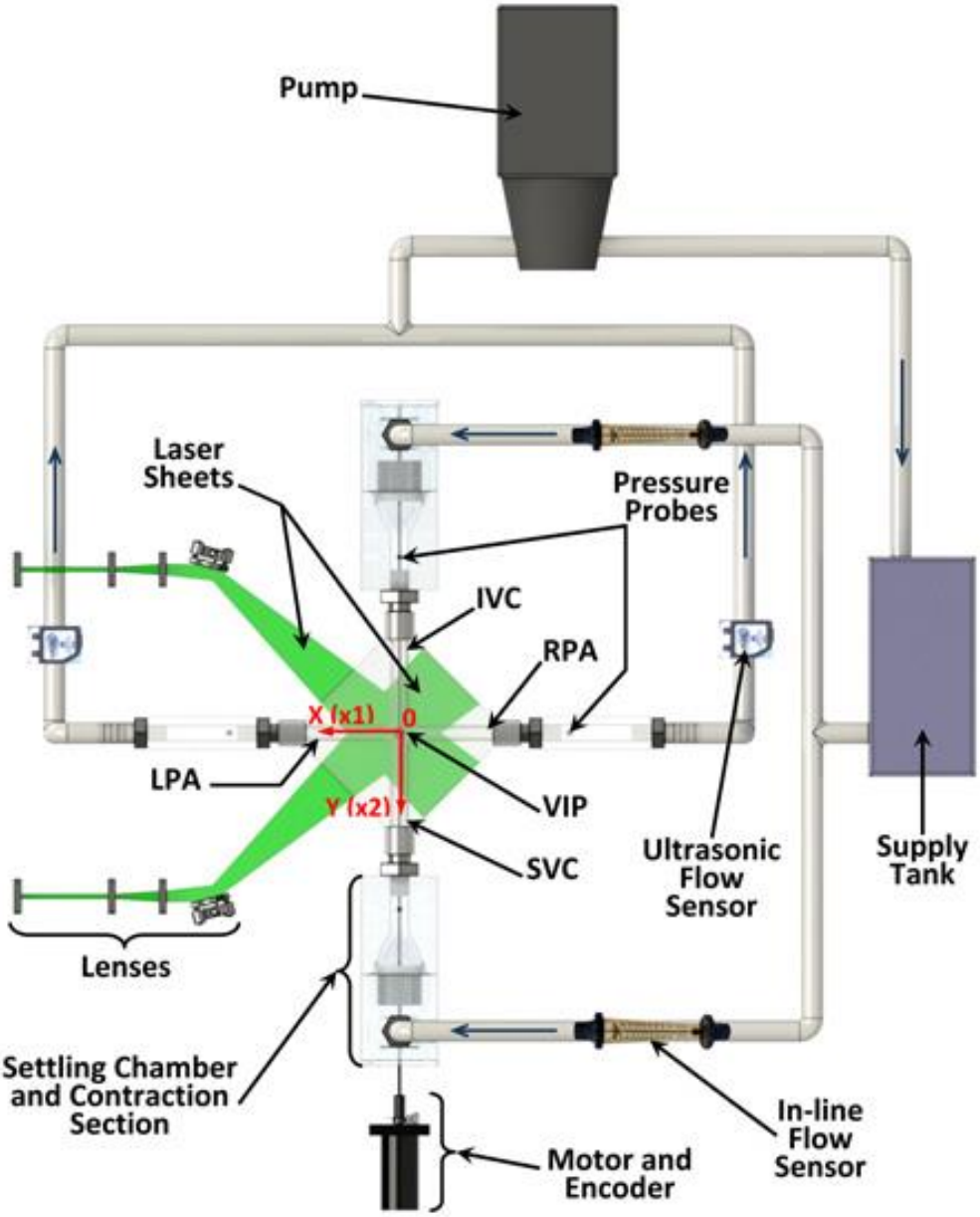

Figure 51: Schematic diagram of the experimental setup. The lenses and laser sheet are not included in the current setup. Image courtesy (Kerlo, 2013)

7.2.2.1 TCPC model

The idealized TCPC model used by Kerlo et al, 2013 in their hydraulic tests consists of two inlets and two outlets that meet perpendicularly (Figure 53). The inlets mimic the inferior vena cava and the superior vena cava with the diameters of the tube set at 20 mm. The outlets representing the left and right pulmonary arteries have a diameter of 18 mm. Because the intersection of the vena cava and pulmonary arteries has no sharp edges, a curvature to the intersections is added. Kerlo (2013) made the idealized TCPC from silicone to create a transparent TCPC to obverse the flow. The silicone TCPC model is created by an in-house procedure depicted in Figure 53. First, a solid negative half mold of the idealized TCPC is printed. Then, from this 3D-printed mold, a 2-part marine silicone rubber mold is created. Then, a cast water-soluble optical wax in the 2-part silicon is created. The surface of the negative mold is sanded to provide a smooth finish. Fourth, the waxed mold is encased into the transparent silicon rubber (Sylgard 184 (Farnell, 2017)). Fifth, the wax is removed using warm water to create the transparent TCPC model. The accuracy of the TCPC model in Kerlo et al. (2013) was defined by the resolution of the 3D printer, which for most 3D printers is 0.2 mm.

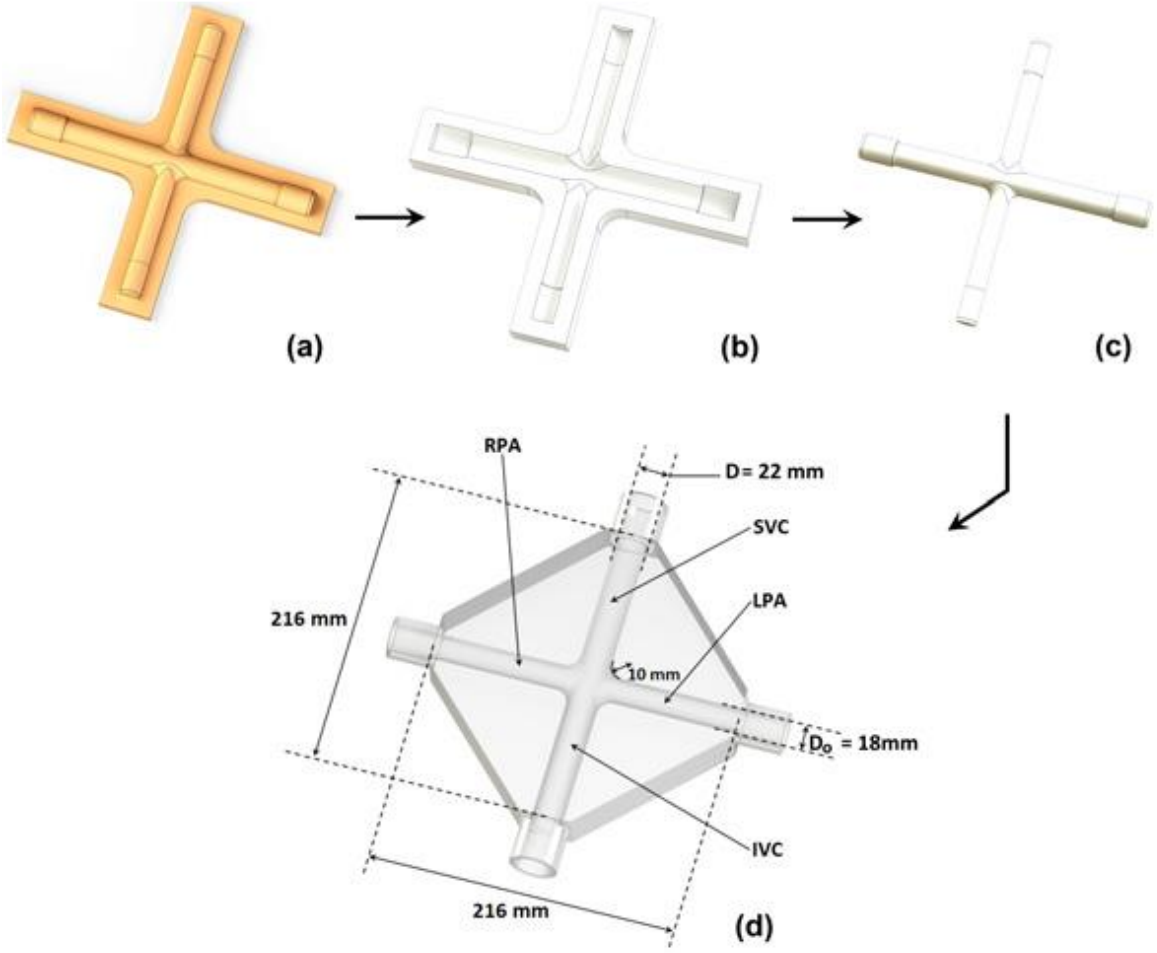

Figure 52: The idealized TCPC model with the dimensions and an illustration of the manufacturing process of the transparent silicon TCPC mode. A) 3D printed half mold; b) marine silicone half mold; c) wax negative mold; d) transparent silicon test section after wax is removed from the inside. Image courtesy (Kerlo, 2013)

7.2.2.2 Mockup loop with the actuator inside the VIP

As mentioned, the hydraulic test is copied from the hemodynamic studies performed by the group of Rodefeld. Figure 52 depicts the mockup loop that is within which the TCPC is placed. The full test setup is described by Kerlo (2013). In the setup by Kerlo (2013), the rotation of 3D printed VIP within the TCPC intersection was driven by a shaft connected to an external BLDC. The actuator prototype will be enclosed by a solid VIP in the current setup, as depicted in Figure 54. The VIP will have the same outer shape as the VIP

from Kerlo (2013); however, a 5.4 mm hole is made in the middle into which the actuator is placed. The open space is filled with 3D-printed cone shape caps. The wires of the actuator will run through the hollow shaft.

The actuator is externally connected to the DM183021 development circuit board and the bench power supply from the torque test. The development circuit board is controlled through a PC and sets the rotational speed to 5000 RPM.

The fluid inside the mock circulation loop resembles the viscosity of blood and is made from a mixture of water, glycerin, and sodium iodine. The density of the fluid is $\rho = 1.283\, kg/m^3$ instead of the $\rho = 1.060\, kg/m^3$ for blood. Kerlo (2013) decided to use this mixture because the refractive indices and the viscosity were more critical to meet than the density of the fluid. The refractive indices matched the refractive indices of the TCPC model, which is essential to prevent distortion in the optical experiments they conducted. In the current test, the same fluid is used, allowing for comparable results. The blood flow in the mock-up loop has a continuous flow comparable to the blood flow entering the TCPC.

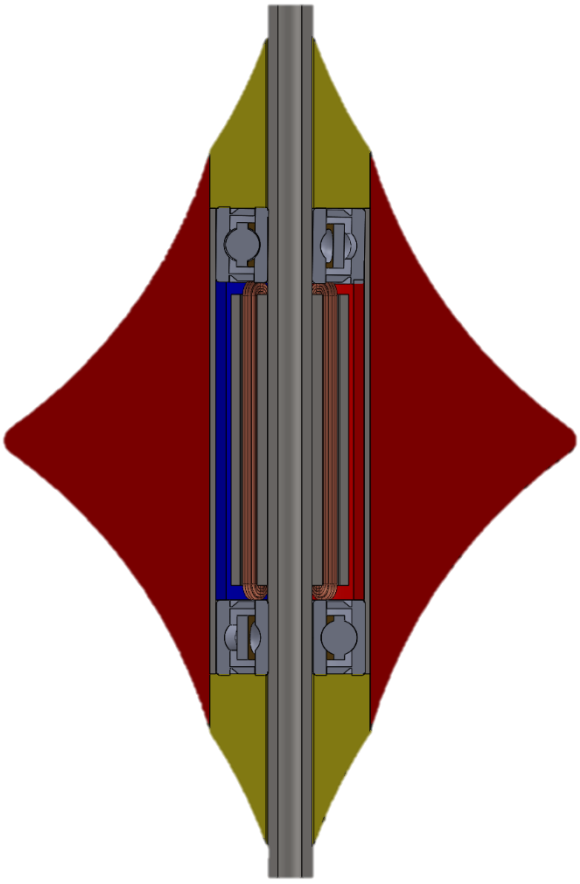

Figure 53: Cross-sectional view of the actuator inside the solid impeller. The red is the impeller, and the yellow are the caps.

7.2.2.3 Sensors in the mock circulation loop

Four pressure ports at each branch of the test section were designed in the study of Kerlo (2013) (Figure 52). The pressure ports are designed to house a high fidelity Millar 5F pressure catheter (Millar, Instruments, TX), with an accuracy of 1 mmHg. The flow entering the inlet and exiting from the outlet is simultaneously measured using the flow meters. The flow rate is measured non-invasively with two clamp-on tubing ultrasonic flow sensors (PXL12, Transonic System Inc.) connected to a flow meter module (TS410, Transonic Systems Inc.). In addition, temperature sensors are placed at the inlets and outlets of the TCPC. The placement should not intervene with the blood flow or influence the pressure measurements. Platinum resistance thermometers are chosen as temperature sensors because they have accuracy down to 0.1°C (RSPro, 2021b), which is the temperature difference found by Rodefeld et al. (2019).

7.2.3 List of materials

- Mock circulation loop
    - Supply tank
    - Two settling chambers
    - Ultrasonic flow sensors (PXL12, Transonic System Inc.)
    - Flowmeter module (TS410, Transonic Systems Inc.)
    - CA series centrifugal pump (Micropump, 2021)
    - Millar 5F pressure catheter (Millar, Instruments, TX)
    - pump controller (PXI 6221 DAQ, Nationalinstruments)
    - A mixture of water, glycerin, and sodium iodine
    - Tubbing clamps
    - Thermocouple (RSPro, Haarlem, The Netherlands)
- TCPC mock model
- Actuator prototype
- VIP prototype

- DM183021 development circuit board
- Bench power supply

7.2.4 Test protocol

The temperature and hydraulic power in the mock circulation loop are measured during the same experiment. For the fatigue test, a separate test protocol is described below.

1. The input variables for the test are the optimum current and voltage from the previous test set by the power supply.
2. Then the actuator should run until a steady-state in the temperature increase is reached. If no increase in temperature is observed, the test is aborted after 2 hours of the actuator running.
3. During the 2 hours with 1 min intervals the flow rate and pressure rise within the mock-up loop are registered.
4. Steps 2 should be repeated three times.
5. If at any moment the fluid increases more than 10 ℃, the experiment should be aborted immediately.

After the experiment, the bearings are removed to expose the stator and the permanent magnets. The actuator is visually inspected for damage in the parts, with special attention to the stator. If no visual damage is found, the actuator should be reassembled, and the fatigue test is performed.

For the fatigue test, the fluid's viscosity is increased by increasing the percentage of glycerin and reducing the percentage of water by 10% in the mixture. Then the same test protocol as described above is again performed. The test should run for at least five hours. Then the actuator should be taken apart and inspected for visual damage. If no visual damage is found, the test will be rerun with a set RPM of 10,000. The voltage might need to be increased to reach the RPM. The actuator will run for 5 hours, and the actuator is taken apart again.

7.2.5 Data processing and conclusion drawn from the experiments

7.2.5.1 Temperature

For the temperature, different results from the various locations should be considered. The room temperature influences the fluid temperature in the mock circulation loop. Therefore, the temperature should be constant during the test. The maximum temperature increase is registered and depicted in a graph showing the temperatures over the test's time. The maximum rise of the fluid temperature in the mock circulation should not be more than 1°C. Otherwise, the actuator can potentially cause damage to the blood cells.

7.2.5.2 Hydraulic power

The experiment measures the pressure difference and flow rate. From this calculation in combination with Eq. 3.26, the hydraulic power is calculated. The resulting hydraulic power should be outlined against the time to evaluate the difference of hydraulic power over a period. The hydraulic power value is used to estimate if the actuator can power the VIP. If the average hydraulic power over the test duration is 75% of the required hydraulic power, the actuator should be further optimized or change to a PMSM configuration. If the hydraulic

7.2.5.3 Fatigue test

The data processing for the fatigue test is the same as for the above-described experiments. The hydraulic power and temperature are outlined against the running time. The hypothesis is that the fatigue test shows no visual damage, and the actuator maintains a steady torque output. If both are true, the actuator is robust enough to withstand a relatively extended running time. The fatigue test should then be prolonged to run for multiple days or even months.

8. Discussion

This master thesis aims to design an actuator to power the VIP for patients with Fontan circulation. An electromotor was used as a basis to design the actuator with the outer dimensions enabling motor incorporation within a VIP for minimally invasive implantation. The current design meets most of the requirements, and others require additional research.

The presented motor concept consists of a shaft surrounded by a stator with six yokes around each are 13 windings wrapped. Surrounding the stator are the magnets, which are held together by an outer casing. Two bearings are added on the top and the bottom to seal the actuator and allow the rotor to rotate around the stator. The stator meets the required outer dimensions and provides the required continuous movement of 360 degrees of rotation (Table 8). The third requirement states that the torque and power output should be 1767 µNm and 0.92 watts based on the assumed efficiency of 16% for the VIP generating 4.4 L/min of average flow. The torque calculation showed a requirement for torque output of 1715.4 µNm, based on the first basic schematic design. Power losses were not included in these calculations. After optimizing for the power losses and recalculating the actuator's output, the mechanical torque output of the actuator is 2446.8 µNm, and the mechanical power output is 0.632 Watt. These values are above the required torque.

Table 8: The requirements with the required values and what they are in the concept actuator. Green indicates that the actuator completely meets the requirement, orange indicates that the actuator partially meets the requirements, and red indicates that the requirement is not met in the current actuators or requires further testing.

Requirement	Required	Concept
Dimensions	Ø5.4mm by 11 mm	Ø5.4mm by 11 mm
Rotation	360° continuous movement	360° continuous movement
Configuration	Outrunner	Outrunner
Output	1767 µNm, 0.92 W	2446.8 µNm, 0.632 W
Internal temperature	Max 155°C	57.5°C
Sealed off	Completely	Completely
off-the-shelve components	All components	50% of the components, not the stator and the magnets
Surrounding blood temperature	Max 40°C	Concluded from maximum increment found by Granegger et al. (2019) of 1.3°C.
Lifetime	3 years	Requires further testing
Power supply	Implantable battery	Requires further investigation

The torque calculations have been validated using two actuators as reported in the literature. Unfortunately, not all the necessary information was available from the researched articles. However, these missing values were found in some other sources. The validation calculations show that the values are close to the values reported in the articles. Therefore, with some certainty, it can be concluded that the torque equation can give reliable results also for the presented actuator concept. Note that the actuators used for the validation are both in-runners, which could bias the results. However, after careful consideration, it was assumed that the equations could be used for both in-runners and outrunners.

The power loss calculations have some limitations that can cause a difference when assessing the torque output. First, the power losses through the wire are calculated assuming a straight wire. It was assumed that the power losses in the coil are the same throughout the whole wire length; however, a difference due to heat transfer between the wires probably exists. Secondly, the total power loss is calculated by only considering the resistivity power loss and mechanical power losses, thereby neglecting the other power losses. Nearly 80% power loss was caused by resistivity; however, further testing is required to prove this assumption. Third, besides the potential differences in the power losses calculation, the hydraulic efficiency of the device is estimated based on other devices. This efficiency should be further tested with the test protocols described in chapter 7.

The temperature build-up in the actuator is calculated as the required maximum temperature. The temperature equation is not validated because the same out-runner actuators were not found. The only reference found was an in-runner actuator of the same size. These actuators have a temperature rise of $12.25°C$ when taking a current of 0.45A. In the current study, an internal temperature rise in the actuator of 44°C was calculated when considering 0.45A. However, due to the different setup, no conclusion can be drawn from this reference actuator, only that the temperature is indeed lower for an in-runner. Another limitation of the temperature calculations is that the shaft in the center is not included due to its unknown influence.

The sixth requirement states that the actuator needs to be sealed off to ensure no contact with the blood or air from the motor gap leaking into the bloodstream. The actuator will not function properly and potentially in the motor gap if blood would enter the motor. Therefore, a bearing on the top and the bottom of the motor should be added to seal the current design. However, this addition increases the actuator axial length above the required length. An option to reduce the length is to include a thinner bearing or modifying the impeller design to ensure the correct fitting of the actuator.

The seventh requirement states that the actuator should be made of as many off-the-shelf components as possible. In the current design, wire, shaft, and outer casing are off-the-shelf components. The stator and permanent magnets are required to be custom-made. If the actuator is made in series production, the custom-made manufacturing process changes and reduces costs. WEDM can cut materials up to 255 mm in thickness (Roessen & Bakker, 2021). For series production, the stator can be made out of a 255 mm thick material. After machining, the material is cut into 11 mm thick stators. This would result in 20 stators. The machining time of thicker material is longer, but dividing this over multiple pieces would reduce the costs.

A specialized company should make the magnets used in the proposed system because of the difficulty and steps required to produce a magnet. Series production makes the magnet more interesting for an outside company to manufacture them. However, if no company is interested in making a single unit, the described process in chapter 6.2.3 could be used to manufacture a prototype.

The requirement of the actuator having a lifecycle containing three years without the service or maintenance requirements was based on the lifetime of the Heartmate III assist device (Abbot, 2020). Furthermore, the design is simplified as much as possible to ensure a robust and durable configuration. The actuator should also be easily controllable, which can be accomplished by choosing a commercially available and well-trusted motor driver. The motor drive should provide reliable control and preferably be small enough to be implanted inside the human body. In the current design, the motor driver was not addressed. However, the motor driver is mentioned in the test as a development circuit board. After the tests, the requirements for the motor driver should be outlined, and a reliable off-the-shelf driver can be chosen.

The next requirement states that the actuator should be powered with a small 3V battery, implementable near the impeller underneath the skin. An implantable battery significantly reduces the risk of infections due to drivelines entering the skin. An example of implantable batteries is the batteries used for pacemakers. A major concern with using a small battery is that the required current is high along with the actuator, which requires a continuous power supply. Unfortunately, there are currently no batteries that are small enough with this amount of ampere-hour rates. Further research is required to find the possibilities to reduce the

size of a battery while keeping a high ampere-hour. An alternative is a battery on the outside of the body. In addition, an external battery has the advantage of changing the battery when it runs down without the need for surgical intervention. Note that, as mentioned, a disadvantage of an external battery is the increased risk of infection.

The current actuator design is set up as a BLDC motor because it is easier to control and requires fewer sensors. In addition, the BLDC motor represents a less complicated system that is more reliable to implant into the human body. The advantage of using a PMSM configuration is a reduction of the torque ripple, which increases the efficiency of an actuator. An increased efficiency results in higher torque output. If the torque test does not result in enough torque output, a PMSM configuration should be tested again. Therefore, the current supply needs to change to an alternating current and the layout of the winding to a distributed layout instead of a concentrated layout as in the current concept design.

In case the design optimization does not result in enough higher torque output, renowned motor manufacturing companies could be contacted to gain more insights into the possible optimization for the outrunner electromotor. After optimizing the prototype, if the actuator still does not work as required, an alternative option would be to choose a commercially available in-runner actuator and change the design of the impeller to accommodate the in-runner.

Unfortunately, none of the components could be manufactured during the writing of this thesis. F First, the current COVID-19 situation restricted access to the workshop of the University of Maastricht. Therefore, the whole project was focused on modelling and analytical evaluation. Secondly, no funding was available to cover manufacturing costs.

From this thesis project, several lessons were learned:

1. Before starting a research project, the researcher should make a well-structured plan to give a proper direction. If the structure is less profound, it is harder to determine what should be investigated first and what should be left for the future. A good presentation structure is also essential to get the desired information and restrict participants from incorporating less relevant subjects.
2. Solid basic knowledge is necessary to be able to discuss the potential changes in the proposed system.
3. When bringing up an idea, it is important to restrict the discussion to the main focusing area.
4. Simulation programs can be used as an additional check but validated analytical calculations are more reliable.
5. Last but not least, it is essential to ask for help from experts to complete a research project.

Conclusion

In this thesis, the gap in treatment for patients with a Fontan circulation was described. A potential concept to bridge the gap is the catheter-based VIP developed by the group of Rodefeld. In their research, the VIP is not powered by an internal actuator. This thesis aimed to design an actuator that can power the VIP. The requirements of the actuator are defined. The designed actuator is an outrunner electromagnetic motor that is easily attached to the VIP. It can produce a torque of 2446 µNm while the temperature does not exceed the critical limit value. The next step will be to prototype and test the designed actuator. After that, conclusions can be drawn about the feasibility of powering the VIP with the proposed actuator design.

Abbreviations

- Ao Aorta
- AoV Aortic Valve
- AG Air gap
- BLDC Brushless direct current
- C Coil
- CB Core back length
- EMF Electromotive force
- F Lorentz Force
- LA Left Atrium
- LPA Left Pulmonary Artery
- LV Left Ventricle
- IP Interpole Length
- IVC Inferior Vena Cava
- M Moment Arm
- MPA Main Pulmonary Artery
- MV Mitral Valve
- NdFeB Neodymium Iron Boron
- NP North pole permanent magnet
- ODA Outer Diameter of the Actuator
- ODR Outer Diameter of the rotor
- ODS Outer Diameter of the Stator;
- PDA Patent Ductus Arteriosus
- PM Permanent Magnet
- PMSM Permanent magnet synchronous motor
- PMt Permanent Magnet Thickness
- PV Pulmonary Valve
- R Rotor
- RA Right Atrium
- RMS Root mean square
- RPA Right pulmonary artery
- RPM Rounds per minute
- RV Right Ventricle
- S Stator
- SH Shaft Hole
- YBl Yoke base length
- YBt Yoke base thickness
- YTt Yoke top thickness
- Sl Slot
- SO Slot opening
- SP South pole permanent magnet
- SVC Superior Vena Cava
- SVHD Single Ventricle Heart Defects
- TCPC Total cavopulmonary connection
- TV Tricuspid Valve
- WEDM Wire Electrical Discharge Machining
- Y Yoke
- YB Base of the yoke
- YBl Yoke Base Length
- YBt Yoke Base Thickness
- YC Connection of the yoke to the rest of the stator
- YT Yoke Top
- YTt Yoke top thickness

Symbols

- A_{vessel} the surface area of a vessel [mm^2]
- A_{win} the surface area was taken by windings without considering the fill factor [mm^2]
- A_{plate} plane area [mm^2]
- A_{wire} the cross sectional area of a wire [m^2]
- $\hat{B}$ the peak value of the flux density [T]
- B_g air gap flux density [T]
- B_{max} maximum flux density [T]
- B_r residual flux density [T]
- B_{ro} the outer radius of the bearing [mm]
- B_{ri} the inner radius of the bearing [mm]
- B_{st} stack height of the bearing [mm]
- c_f force constant
- η_{el-m} motor efficiency
- $\eta_{impeller}$ impeller efficiency
- η_h hydraulic efficiency
- δ air gap length [mm]
- D_{wir} diameter of the copper wires [mm]
- D_{ao} the outer radius of the actuator [mm]
- D_{sh} diameter of the shaft [mm]
- f fundamental supply of frequency
- F force [N]
- F_L Lorentz force [N]
- i_{in} current input of the motor [A]
- i_m the electrical current drawn by the motor [A]
- i_w current through motor windings [A]
- H static pressure head [mmHg]
- h_{heat} heat transfer coefficient of the material [W/m^2K]
- h_m magnet thickness [mm]
- k_e constant determined by curve fitting from the manufacturer's data
- k_h hysteresis constant
- K_e back EMF constant [Vs/rad]
- k thermal conductivity of the material [W/mK]
- K_τ torque constant [Nm/A]
- $K_{v\,(RPM)}$ velocity constant [RPM/V]
- $K_{v\,(SI)}$ velocity constant in the SI units [Rad/Vs]
- L_{st} axial stack height of the actuator [mm]
- L_{str} axial stack height of the rotor [mm]
- L_{plate} plate thickness [mm]
- l_{wire} length of the wire [mm]
- μ_0 air permeability [N/A^2]
- μ_r relative permeability of the magnet [N/A^2]
- m_{rot} weight of the rotor [kg]
- N number of windings
- N_m number of poles
- N_s number of slots
- n_r the number of bearings
- Δp measured pressure rise across the pump [mmHg]
- p_{TCPC} pressure in the TCPC [Pa]
- $P_{CL(BLDC)}$ power losses due to eddy currents in BLDC [Watts]
- $P_{CL(PMSM)}$ power losses due to eddy currents in PMSM [Watts]
- P_{el} electric power [Watts]

- P_{fr} friction losses [Watts]
- P_{lw} electric power losses due to wire resistivity [Watts]
- P_{int} power loss due to power interruption [Watts]
- P_h hydraulic power [Watts]
- P_{hys} hysteresis power losses [Watts]
- P_m mechanical power [Watts]
- P_{wind} power loss due to the windage losses [Watts]
- Q_{heat} heat flux [Watt]
- Q_{Lmin} volumetric flow [L/min]
- $Q_{(SI)}$ volumetric flow in SI-units [m^3/sec]
- R_{ao} the outer radius of the actuator [m]
- R_g the reluctance of the air gap [H^{-1}]
- R_l reluctance due to magnet to stator flux leakage [H^{-1}]
- R_m the reluctance of the magnet pole [H^{-1}]
- R_{ON} resistance of the power switch in the ON state [Ω]
- R_{OVIP} the outer radius of the VIP [m]
- R_r the reluctance of the rotor core [H^{-1}]
- R_{ri} the inner radius of the rotor [mm]
- R_{ro} the outer radius of the rotor [mm]
- R_s the reluctance of the stator core [H^{-1}]
- R_{win} resistance in the motor winding [Ω]
- R_{wire} resistance of a wire [Ω]
- R_{th} thermal resistance [K/W]
- R_{th1} thermal resistance from windings to stator core [K/W]
- R_{th2} thermal resistance stator core to air gap [K/W]
- R_{th3} thermal resistance air gap to the magnet [K/W]
- R_{th4} thermal resistance magnet to case [K/W]
- R_{th5} thermal resistance through the physiological fluid in K/W
- R_{th6} thermal resistance through the impeller shell in K/W
- R_{thtot} a sum of the thermal resistance [K/W]
- ρ_{wire} the resistivity of a material [Ωm]
- σ_h hydrodynamic torque [Nm]
- σ_m maximum motor torque [Nm]
- S_{ag} the surface area of the air gap [m^2]
- SG specific gravitation
- Sh_{ri} inner radius of the shaft [mm]
- Sh_{ro} outer radius of the shaft [mm]
- Sh_{st} stack height of the shaft [mm]
- S_m magnet area perpendicular to magnetizing direction [m^2]
- S_{ri} inner radius of the stator [mm]
- S_{ro} outer radius of the stator [mm]
- T temperature [K]
- T_{in} temperature of the windings [K]
- T_{out} temperature of the ambient [K]
- $T_{surface}$ temperature rise of the surface [K]
- T_{fluid} temperature rise of the fluid [K]
- t time [s]
- τ torque [Nm]
- τ_{ave} average torque [Nm]
- τ_{im} impeller torque [Nm]
- τ_{max} maximum torque [Nm]
- τ_{min} minimum torque [Nm]
- τ_{ripple} torque ripple [Nm]

- $\omega_{(\mathrm{SI})}$ angular velocity in SI-units [rad/sec]
- $\omega_{(RPM)}$ rotational velocity [RPM]
- V_{in} voltage input of the motor [V]
- v velocity [m/s]
- x_{SAMA} ratio of the stator area to the motor area

Reference list

Abbot. (2020). *HeartMate3 Left ventricular assist system, instruction to use*: Abbott.

About Congenital Heart Defects. (2020). Retrieved from https://www.heart.org/en/health-topics/congenital-heart-defects/about-congenital-heart-defects

Andrada, P., Torrent, M., Perat, J. I., & Blanqué, B. (2004). Power losses in outside-spin brushess DC motor. *Renewable Energy and Power Quality Journal*(2), 320-321-320-325.

bearings, A. (2021). 691XHZZ Miniature & Instrument Series, Stainless Steel Ball Bearing. Retrieved from https://www.astbearings.com/catalog/min_inst_met/691XHZZ

Boukais, B., & Zeroug, H. (2004). *Efficency Determination of a Brushless DC Motor Under Field Weakening Operation*. Paper presented at the Progress in Electromagnetic Research Symposium.

Britt, L. D. B., Phillip S.; Peitzman, Andrew B.; Jurkovich, Gregory. (2012). *Acute Care Surgery*. : Lippincott Williams & Wilkins.

Broda, C. R., Downing, T. E., & John, A. S. (2020). Diagnosis and management of the adult patient with a failing Fontan circulation. *Heart Fail Rev, 25*(4), 633-646. doi:10.1007/s10741-020-09932-0

Brushed vs. Brushless Motors. (2020). Retrieved from https://motors.vex.com/brushed-brushless

Calvert, J. W., & Lefer, D. J. (2012). Overview of Cardiac Muscle Physiology. In *Muscle* (pp. 57-66).

Cengel, Y. A. (2003). *HEAT TRANSFER A practical approach*: New York, NY, USA: McGraw-Hill.

Cham, C.-L., & Samad, Z. B. (2014). Brushless DC Motor Electromagnetic Torque Estimation with Single-Phase Current Sensing. *Journal of Electrical Engineering and Technology, 9*(3), 866-872. doi:10.5370/jeet.2014.9.3.866

Chen, Q., Shu, H., & Chen, L. (2012). Simulation analysis of cogging torque of permanent magnet synchronous motor for electric vehicle. *Journal of mechanical science and technology, 26*(12), 4065-4071.

Chopski, S. G., Moskowitz, W. B., Stevens, R. M., & Throckmorton, A. L. (2017). Mechanical Circulatory Support Devices for Pediatric Patients With Congenital Heart Disease. *Artif Organs, 41*(1), E1-E14. doi:10.1111/aor.12760

Circulatory Support without Surgery for Heart Failure Patients. (2020). Retrieved from https://www.maxongroup.com/maxon/view/application/Circulatory-Support-without-Surgery-for-Heart-Failure-Patients

Conrad. (2021). Block Koperdraad gelakt Buitendiameter (incl. isolatielak)=0.10mm. Retrieved from https://www.conrad.nl/p/block-koperdraad-gelakt-buitendiameter-incl-isolatielak010-mm-2702-m-020-kg-605278

Consiglieri, L., dos Santos, I., & Haemmerich, D. (2003). Theoretical analysis of the heat convection coefficient in large vessels and the significance for thermal ablative therapies. *Physics in Medicine & Biology, 48*(24), 4125.

Cullity, B. D., & Graham, C. D. (2011). *Introduction to magnetic materials*: John Wiley & Sons.

Cysyk, J., Clark, J. B., Newswanger, R., Jhun, C.-S., Izer, J., Finicle, H., . . . Rosenberg, G. (2019). Chronic in vivo test of a right heart replacement blood pump for failed Fontan circulation. *ASAIO Journal, 65*(6), 593-600.

DeGan, J., Kennington, J., Anupindi, K., Shetty, D., Chen, J., Rodefeld, M., & Frankel, S. (2011). *Modeling of Patient-Specific Fontan Physiology From MRI Images for CFD Testing of a Cavopulmonary Assist Device*. Paper presented at the Summer Bioengineering Conference.

Delorme, Y., Anupindi, K., Kerlo, A.-E. M., Shetty, D., Rodefeld, M., Chen, J., & Frankel, S. (2013). Large eddy simulation of powered Fontan hemodynamics. *J Biomech, 46*(2), 408-422. doi:10.1016/j.jbiomech.2012.10.045

Delorme, Y. T., Anupindi, K., Kerlo, A., Shetty, D., Rodefeld, M., Chen, J., & Frankel, S. (2013). Large eddy simulation of powered Fontan hemodynamics. *Journal of biomechanics, 46*(2), 408-422.

Derammelaere, S., Haemers, M., De Viaene, J., Verbelen, F., & Stockman, K. (2016). *A quantitative comparison between BLDC, PMSM, brushed DC and stepping motor technologies*. Paper presented at the 2016 19th International Conference on Electrical Machines and Systems (ICEMS).

Deutsch, S., Tarbell, J. M., Manning, K. B., Rosenberg, G., & Fontaine, A. A. (2006). Experimental fluid mechanics of pulsatile artificial blood pumps. *The Annual Review of Fluid Mechanics, 38*, 65-86. doi:10.1146/annurev.fluid

Facts about Hypoplastic Left Heart Syndrome. (2019). Retrieved from https://www.cdc.gov/ncbddd/heartdefects/hlhs.html

Farnell. (2017). *Sylgard 184 Silicone Elastomer*.

Farnell. (2021). DM183201 Development board. Retrieved from https://nl.farnell.com/microchip/dm183021/picdem-bldc-motor-cntlr-dev-board/dp/1084612#
FaulHaber. (2020). Faulhaber B-micro. Retrieved from https://www.faulhaber.com/en/products/brushless-dc-motors/faulhaber-b-micro/
Fontan, F., & Baudet, E. (1971). Surgical repair of tricuspid atresia. *Thorax, 26*(3), 240-248.
German, R. M. (1996). *Sintering theory and practice*.
Gewillig, M. (2005). The Fontan circulation. *Heart, 91*(6), 839-846. doi:10.1136/hrt.2004.051789
Gieras, J. F. (2002). *Permanent magnet motor technology: design and applications*: CRC press.
Giridharan, G. A., Ising, M., Sobieski, M. A., Koenig, S. C., Chen, J., Frankel, S., & Rodefeld, M. D. (2014). Cavopulmonary assist for the failing Fontan circulation: impact of ventricular function on mechanical support strategy. *ASAIO J, 60*(6), 707-715. doi:10.1097/MAT.0000000000000135
Granegger, M., Thamsen, B., Hubmann, E. J., Choi, Y., Beck, D., Valsangiacomo Buechel, E., . . . Hubler, M. (2019). A long-term mechanical cavopulmonary support device for patients with Fontan circulation. *Med Eng Phys, 70*, 9-18. doi:10.1016/j.medengphy.2019.06.017
Griselli, M., Sinha, R., Jang, S., Perri, G., & Adachi, I. (2018). Mechanical Circulatory Support for Single Ventricle Failure. *Front Cardiovasc Med, 5*, 115. doi:10.3389/fcvm.2018.00115
Halliday, D., Resnick, R., & Walker, J. (2013). *Fundamentals of physics*: John Wiley & Sons.
Han, J., & Trumble, D. R. (2019). Cardiac Assist Devices: Early Concepts, Current Technologies, and Future Innovations. *Bioengineering (Basel), 6*(1). doi:10.3390/bioengineering6010018
Hanselman, D. C. (2003). *Brushless permanent magnet motor design*.
Harris, I., & George, L. (2017). Single Ventricle Defects and the Fontan. Retrieved from https://www.achaheart.org/your-heart/health-information/single-ventricle-defects-and-the-fontan/#:~:text=Single%20ventricle%20defects%20are%20rare,of%20every%20100%2C000%20live%20births.
Hoganas. (2018). Material data: Somaloy 700. In.
Hsu, D. T. (2015). The Fontan operation: the long-term outlook. *Curr Opin Pediatr, 27*(5), 569-575. doi:10.1097/MOP.0000000000000271
Imielski, B. R., Niebler, R. A., Kindel, S. J., & Woods, R. K. (2017). HeartWare Ventricular Assist Device Implantation in Patients With Fontan Physiology. *Artif Organs, 41*(1), 40-46. doi:10.1111/aor.12852
Inc., T. S. (2021). PXL clamp on flowsensor. Retrieved from https://www.transonic.com/product/pxl-clamp-on-flowsensor/
Inc., T. S. (2021). TS410 Tubing module. Retrieved from https://www.transonic.com/search/product/ts410-tubing-module/
instruments, N. (2021). PXI-6221 Retrieved from https://www.ni.com/nl-nl/support/model.pxi-6221.html
Intro to the heart. (2012). Retrieved from https://antranik.org/intro-to-the-heart/
Jameson, E. C. (2001). *Electrical discharge machining*: Society of Manufacturing Engineers.
Kapur, N. K., Esposito, M. L., & Wihiteheed, E. (2020). Aortix: a novel intra-aortic entrainment pump. *Future Cardiology, 17*(2), 283-291.
Kennington, J. R., Frankel, S. H., Chen, J., Koenig, S. C., Sobieski, M. A., Giridharan, G. A., & Rodefeld, M. D. (2011). Design Optimization and Performance Studies of an Adult Scale Viscous Impeller Pump for Powered Fontan in an Idealized Total Cavopulmonary Connection. *Cardiovascular Engineering and Technology, 2*(4), 237-243. doi:10.1007/s13239-011-0058-2
Kerlo, A.-E. M. (2013). *EXPERIMENTAL STUDY OF PATHOLOGICAL AND CARDIOVASCULAR DEVICE HEMODYNAMICS*. (PhD). Purdue University, West Lafayette, Indiana.
Kerlo, A.-E. M., Delorme, Y. T., Xu, D., Frankel, S. H., Giridharan, G. A., Rodefeld, M. D., & Chen, J. (2013). Experimental characterization of powered Fontan hemodynamics in an idealized total cavopulmonary connection model. *Experiments in Fluids, 54*(8). doi:10.1007/s00348-013-1581-8
Kim, T., Lee, S., & Kim, W. (2014). *Design and characteristic analysis of high speed slotless permanent magnet sychoronous motor for surgical hand-piece*. Paper presented at the 2014 IEEE International Conference on Industrial Technology (ICIT).
Kuria, J., & Hwang, P. (2011). Modeling Power Losses in Electric Vehicle BLDC Motor. *Journal of Energy Technologies and policy, 1*(4).
Lacour-Gayet, F. G., Lanning, C. J., Stoica, S., Wang, R., Rech, B. A., Goldberg, S., & Shandas, R. (2009). An artificial right ventricle for failing fontan: in vitro and computational study. *Ann Thorac Surg, 88*(1), 170-176. doi:10.1016/j.athoracsur.2009.03.091
Leval, M. R. d. (1998). The Fontan Circulation: What Have We Learned? What to Expect? *Pediatric Cardiology, 19*, 316-220.

Lingadurai, K., Nagasivamuni, B., Muthu Kamatchi, M., & Palavesam, J. (2012). Selection of Wire Electrical Discharge Machining Process Parameters on Stainless Steel AISI Grade-304 using Design of Experiments Approach. *Journal of The Institution of Engineers (India): Series C, 93*(2), 163-170. doi:10.1007/s40032-012-0020-6

Lyle, M., Said, S., & Egbe, A. (2017). Hope and Hazards for Patients After Fontan Procedure. Retrieved from https://www.medscape.com/viewarticle/886896

Mancini, D., & Colombo, P. C. (2015). Left Ventricular Assist Devices: A Rapidly Evolving Alternative to Transplant. *J Am Coll Cardiol, 65*(23), 2542-2555. doi:10.1016/j.jacc.2015.04.039

Materialise. (2021). Metal 3D printing. Retrieved from https://www.materialise.com/en/manufacturing/3d-printing-technology/metal-3d-printing#:~:text=Metal%203D%20Printing%20is%20a,even%20layers%20of%20metallic%20powder.

Maxon EC motors (2020). Retrieved from https://www.maxongroup.com/maxon/view/product/motor/ecmotor/ec/ec6/250101?etcc_cu=onsite&etcc_med=Header%20Suche&etcc_cmp=mit%20Ergebnis&etcc_ctv=Layer&query=2501

Mekid, S. (2010). *Effects of Miniaturisation on Electromagnetic Motors for Micro Mechatronic Systems*. Paper presented at the ASME International Mechanical Engineering Congress and Exposition.

Metalen, S. s. (2021). Material: Stainless steel Capillair. Retrieved from https://salomons-metalen.com/products/stainless-steel/capillair

Micropump. (2021). CA series centrifugal pump. Retrieved from https://www.micropump.com/product_detail.aspx?ProductID=71

Millar. (2021). Pressure catheters. Retrieved from https://millar.com/Research/Pressure-Catheters/

Mohan, N. (2012). *Electric machines and drives: a first course*: Wiley.

Moody, K. H. (2016). Efficiency Evaluation of a Magnetically Driven Multiple Disk Centrifugal Blood Pump.

Nag, T., Santra, S. B., Chatterjee, A., Chatterjee, D., & Ganguli, A. K. (2016). Modelling and minimization of losses for brushless DC (BLDC) motor suitable for electric vehicular applications. *World Journal of Modelling and Simulation, 12*(4), 259-267.

Nathan, M., Baird, C., Fynn-Thompson, F., Almond, C., Thiagarajan, R., Laussen, P., . . . Pigula, F. (2006). Successful implantation of a Berlin heart biventricular assist device in a failing single ventricle. *J Thorac Cardiovasc Surg, 131*(6), 1407-1408. doi:10.1016/j.jtcvs.2006.02.015

Nayak, S., & Booker, P. D. (2008). The Fontan circulation. *Continuing Education in Anaesthesia Critical Care & Pain, 8*(1), 26-30. doi:10.1093/bjaceaccp/mkm047

Newcomb, A. E., Negri, J. C., Brizard, C. P., & d'Udekem, Y. (2006). Successful left ventricular assist device bridge to transplantation after failure of a fontan revision. *J Heart Lung Transplant, 25*(3), 365-367. doi:10.1016/j.healun.2005.05.022

Norwood, W. I., Kirklin, J. K., & Sanders, S. P. (1980). Hypoplastic left heart syndrome: experience with palliative surgery. *The American journal of cardiology, 45*(1), 87-91.

Pang, D.-C., Shi, Z.-J., Xie, P.-X., Huang, H.-C., & Bui, G.-T. (2020). Investigation of an Inset Micro Permanent Magnet Synchronous Motor Using Soft Magnetic Composite Material. *Energies, 13*(17). doi:10.3390/en13174445

Panton, R. L. (2013). Von Karman pump. In *Incompressible flow* (pp. 257-261): John Wiley & Sons.

Prince, M., Novelline, R., Athanasoulis, C., & Simon, M. (1983). The diameter of the inferior vena cava and its implications for the use of vena caval filters. *Radiology, 149*(3), 687-689.

Pyrhonen, J., Jokinen, T., & Hrabovcova, V. (2013). Design of Mangetic Circuits. In *Design of rotating electrical machines*: John Wiley & Sons.

Reichert, T., Nussbaumer, T., & Kolar, J. W. (2009). Torque scaling laws for interior and exterior rotor permanent magnet machines. *IEEE*.

Rodefeld, M. D., Boyd, J. H., Myers, C. D., LaLone, B. J., Bezruczko, A. J., Potter, A. W., & Brown, J. W. (2003). Cavopulmonary assist: circulatory support for the univentricular fontan circulation. *The Annals of Thoracic Surgery, 76*(6), 1911-1916. doi:10.1016/s0003-4975(03)01014-2

Rodefeld, M. D., Coats, B., Fisher, T., Giridharan, G. A., Chen, J., Brown, J. W., & Frankel, S. H. (2010). Cavopulmonary assist for the univentricular Fontan circulation: von Karman viscous impeller pump. *J Thorac Cardiovasc Surg, 140*(3), 529-536. doi:10.1016/j.jtcvs.2010.04.037

Rodefeld, M. D., Frankel, S. H., & Giridharan, G. A. (2011). Cavopulmonary assist: (em)powering the univentricular fontan circulation. *Semin Thorac Cardiovasc Surg Pediatr Card Surg Annu, 14*(1), 45-54. doi:10.1053/j.pcsu.2011.01.015

Rodefeld, M. D., Marsden, A., Figliola, R., Jonas, T., Neary, M., & Giridharan, G. A. (2019). Cavopulmonary assist: Long-term reversal of the Fontan paradox. *J Thorac Cardiovasc Surg, 158*(6), 1627-1636. doi:10.1016/j.jtcvs.2019.06.112

Roessen, L., & Bakker, B. (2021). Faciliteiten. Retrieved from https://www.tudelft.nl/demo/faciliteiten

RSPro. (2021a). RS PRO Type PT 100 Thermocouple 100mm Length, 6mm Diameter. Retrieved from https://nl.rs-online.com/web/p/thermocouples/3730372/

RSPro. (2021b). Thermocouple selection guide. In R. PRO (Ed.).

RSPro. (2021c). Type K thermocouple 1m lenght, 0.075m diameter. In RSPro (Ed.).

Ryan. (2018). Brushless Inrunner vs Outrunner motor? Retrieved from https://www.radiocontrolinfo.com/brushless-inrunner-vs-outrunner-motor/#:~:text=The%20permanent%20magnets%20on%20the,they%20are%20fixed%20in%20position.&text=On%20the%20inrunner%20motor%2C%20you,for%20how%20it%20is%20built.

Sensinger, J. W., Clark, S. D., & Schorsch, J. F. (2011). *Exterior vs. interior rotors in robotic brushless motors*. Paper presented at the 2011 IEEE International Conference on Robotics and Automation.

Serway, R. A., & Jewett, J. W. (2018). *Physics for scientists and engineers*: Cengage learning.

Sintered Neodynium-Iron-Boron Magnets. (2021). In: Arnold Magnetic technologies.

Smith, P. A., Wang, Y., Bieritz, S. A., Sampaio, L. C., Cohn, W. E., Metcalfe, R. W., & Frazier, O. H. (2019). Design Method Using Statistical Models for Miniature Left Ventricular Assist Device Hydraulics. *Ann Biomed Eng, 47*(1), 126-137. doi:10.1007/s10439-018-02140-w

Somaloy, Powders for Electromagnetic Applications. Retrieved from https://www.hoganas.com/en/powder-technologies/soft-magnetic-composites/products/coated-powders-for-electromagnetic-applications

Stewart, G. C., & Givertz, M. M. (2012). Mechanical circulatory support for advanced heart failure: patients and technology in evolution. *Circulation, 125*(10), 1304-1315. doi:10.1161/CIRCULATIONAHA.111.060830

Stumberger, B., Hamler, A., & Hribernik, B. (2000). Analysis of iron loss in interior permanent magnet synchronous motor over a wide-speed range of constant output power operation. *IEEE Transactions on Magnetics, 36*(4), 1846-1849.

Throckmorton, A. L., Carr, J. P., Tahir, S. A., Tate, R., Downs, E. A., Bhavsar, S. S., . . . Moskowitz, W. B. (2011). Mechanical cavopulmonary assistance of a patient-specific Fontan physiology: numerical simulations, lumped parameter modeling, and suction experiments. *Artif Organs, 35*(11), 1036-1047. doi:10.1111/j.1525-1594.2011.01339.x

ToolBox, E. (2003). Thermal Conductivity of some selected Materials and Gases. Retrieved from https://www.engineeringtoolbox.com/thermal-conductivity-d_429.html

Trudnowski, R. J., & Rico, R. C. (1974). Specific gravity of blood and plasma at 4 and 37 C. *Clinical chemistry, 20*(5), 615-616.

Urencio, M., Greenleaf, C., Salazar, J. D., & Dodge-Khatami, A. (2016). Resource and cost considerations in treating hypoplastic left heart syndrome. *Pediatric Health Med Ther, 7*, 149-153. doi:10.2147/PHMT.S98327

Vazquez, R., & Larson, D. F. (2013). Plasma protein denaturation with graded heat exposure. *Perfusion, 28*(6), 557-559. doi:10.1177/0267659113498921

Vora, A. N., Schuyler Jones, W., DeVore, A. D., Ebner, A., Clifton, W., & Patel, M. R. (2019). First-in-human experience with Aortix intraaortic pump. *Catheter Cardiovasc Interv, 93*(3), 428-433. doi:10.1002/ccd.27857

Wang, Y., Karnik, S., Smith, P. A., Elgalad, A., Frazier, O. H., & Kurita, N. (2020). Numerical and Experimental Approach to Characterize a BLDC Motor with Different Radial-gap to Improve Hemocompatibility Performance.

Wang, Y., Logan, T. G., Smith, P. A., Hsu, P. L., Cohn, W. E., Xu, L., & McMahon, R. A. (2017). Systematic Design of a Magnetically Levitated Brushless DC Motor for a Reversible Rotary Intra-Aortic Blood Pump. *Artif Organs, 41*(10), 923-933. doi:10.1111/aor.12965

Ye, S., & Yao, X. (2018). Fast analytical calculation of the air-gap flux density in an outer-rotor permanent-magnet brushless motor. *MATEC Web of Conferences, 189*. doi:10.1051/matecconf/201818906008

Young, H. D., & Ford, A. L. (1992). *University Physics: Student's Solutions Manual to Accompany*: Addison-Wesley.